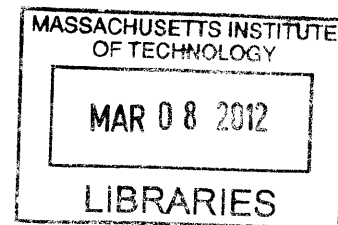# Phytoplankton in Flow

by

William McKinney Durham

B.S., Civil Engineering,
Clemson University (2004)

S.M., Civil and Environmental Engineering,
Massachusetts Institute of Technology (2006)

Submitted to the Department of Civil and Environmental Engineering
in Partial Fulfillment of the Requirements of the Degree of

Doctor of Philosophy in the field of Civil and Environmental Engineering
at the
MASSACHUSETTS INSTITUTE OF TECHNOLOGY

February 2012

Signature of Author..
Department of Civil and Environmental Engineering
December 22, 2011

Certified by...
Roman Stocker
Associate Professor of Civil and Environmental Engineering

Accepted by...
Heidi Nepf
Chair, Departmental Committee for Graduate Students

Phytoplankton in Flow

by

William M. Durham

Submitted to the Department of Civil and Environmental Engineering on December 22, 2011 in Partial Fulfillment of the Requirements for the Degree of Doctor of Philosophy in the field of Civil and Environmental Engineering

ABSTRACT

Phytoplankton are small, unicellular organisms, which form the base of the marine food web and are cumulatively responsible for almost half the global production of oxygen. While phytoplankton live in an environment characterized by ubiquitous fluid motion, the impacts of hydrodynamic conditions on phytoplankton ecology remain poorly understood. In this thesis, we propose two novel biophysical mechanisms that rely on the interaction between phytoplankton motility and fluid shear and demonstrate how these mechanisms can drive thin phytoplankton layers and microscale cell aggregations.

First, we consider 'thin phytoplankton layers', important hotspots of ecological activity that are found meters beneath the ocean surface and contain cell concentrations up to two orders of magnitude above ambient. While current interpretations of their formation favor abiotic processes, many phytoplankton species found in these layers are motile. We demonstrate that layers can form when the vertical migration of phytoplankton is disrupted by hydrodynamic shear. Using a combination of experiments, individual-based simulations, and continuum modeling, we show that this mechanism – which we call 'gyrotactic trapping' – is capable of triggering thin phytoplankton layers under hydrodynamic conditions typical of the environments that often harbor thin layers.

Second, we explore the potential for turbulent shear to produce patchiness in the spatial distribution of motile phytoplankton. Field measurements have revealed that motile phytoplankton form aggregations at the smallest scales of marine turbulence – the Kolmogorov scale (typically millimeters to centimeters) – whereas non-motile cells do not. We propose a new mechanism for the formation of this small-scale patchiness based on the interplay of gyrotactic motility and turbulent shear. Contrary to intuition, turbulence does not stir a plankton suspension to homogeneity, but instead drives patchiness. Using an analytical model of vortical flow we show that motility can give rise to a striking array of patchiness regimes. We then test this mechanism using both laboratory experiments and isotropic turbulent flows generated via Direct Numerical Simulation. We find that motile phytoplankton cells rapidly form aggregations, whereas non-motile cells remain randomly distributed.

In summary, this thesis demonstrates that microhydrodynamic conditions play a fundamental role in phytoplankton ecology and, as a consequence, can contribute to shape macroscale characteristics of the Ocean.

Thesis Supervisor: Roman Stocker
Title: Associate Professor of Civil and Environmental Engineering

ACKNOWLEDGEMENTS

TABLE OF CONTENTS

INTRODUCTION

Phytoplankton are microscopic, unicellular organisms that inhabit nearly all sunlit bodies of water on Earth. While small in size (order 1-500 μm), they cumulatively are responsible over nearly half of the production oxygen on Earth (Field *et al.* 1998). Phytoplankton reside at the bottom of the marine foodweb: almost all life in the Ocean relies on their primary production (Fenchel 1988). However, some phytoplankton can also harm marine life: during harmful algal bloom events, toxic species of phytoplankton can severely impact larger organisms including fish, invertebrates, and seabirds (Harrison *et al.* 1997). Some harmful algal blooms cause such devastation that years are required for the ecosystem to fully recover (Gjosaeter *et al.* 2000).

While abundant in many different environments, the distribution of phytoplankton is far from uniform. Gradients in concentration of phytoplankton span a wide range of length scales, ranging from regions of persistent upwelling at the equator that drives regions of enhanced concentration with length scales of thousands of kilometers (Marañón *et al.* 2001) to ephemeral microscale patchiness that occurs at the scale of centimeters (Mitchell *et al.* 2008, Malkiel *et al.* 1999). This 'patchiness' has many implications on the marine ecosystem, including mean abundance (Steele 1974), predator-prey dynamics (Tiselius 1992, Tiselius *et al.* 1993), and fish recruitment (Lasker 1975). Variance in the distribution of phytoplankton exceeds that of a random process (Mackas 1985) and many mechanisms that might sustain this variability have been proposed (Martin 2003, Appendix: Part Two). Patchiness likely contributes to the amazing diversity encountered in phytoplankton (Richerson *et al.* 1970, Bracco *et al.* 2000); over 3,000 distinct species of phytoplankton (Sournia *et al.* 1991) have been identified. While the competitive exclusion principle (Hardin 1960) suggests that a single phytoplankton species would dominate an entire body of water if it was uniformly mixed (by driving its competitors to extinction), heterogeneity in the spatial distribution of phytoplankton permits the existence of 'contemporaneous non-equilibriums' (Richerson *et al.* 1970) that promote the collective survival of multiple species.

One way to classify different phytoplankton species is by the presence or absence of motility. While some types of phytoplankton are incapable of swimming, and remain at the whim of ambient flows, other types of phytoplankton can actively propel themselves through the water column by propagating bending waves along their flexible flagella (Guasto *et al.* 2012). Toxic species are often motile: about 90% of the species that form harmful algal blooms can actively swim (Smayda 1997). The arrangement and kinematics of the flagella are diverse: Some green algae beat two nearly identical flagella in a breaststroke motion (Polin *et al.* 2009), whereas most dinoflagellates wave two dissimilar flagella in combination for propulsion and steering (Fenchel 2001). For some species, the mechanism of propulsion remains unknown, as in *Synechococcus*, which lacks flagella (Brahamsha 1999, McCarren and Brahamsha 2009). One of the primary functions of cell motility is perform diurnal vertical migrations. Often the upper mixed layer is depleted of limiting nutrients: motility allows cells to spend the daylight hours near the surface where light is more abundant while traversing to depths below the pyncocline at night, where

nutrients are more abundant and predation risks are lower (Ryan *et al.* 2010, Bollens *et al.* 2011).

To keep their motility directed vertically, many phytoplankton generate a stabilizing torque through a process known as gravitaxis. Gravitaxis can arise either actively through behaviorally directed steering (Lebert and Hader 1996) or passively through asymmetries in cell morphology (Kessler 1985, Roberts and Deacon 2002). However, fluid motion in marine environments is inevitable and gradients in fluid velocity give rise to additional torques that act on the cell. If a cell's swimming direction is guided by the combined effect of self-stabilization and shear, it is said to be undergoing gyrotaxis. Gyrotaxis was discovered in 1985, when John Kessler demonstrated that motile phytoplankton cells tend to collect along the centerline of a laminar Poiseuille pipe flow (Kessler 1985). Subsequently, gyrotaxis has been found to give rise to a peculiar form of bioconvection that has been the subject of numerous theoretical and experimental works (see Pedley and Kessler 1992 for a review).

Modeling gyrotactic cells as bottom-heavy prolate spheroids, the temporal evolution of its swimming direction, **p**, can be written as (Pedley and Kessler 1992):

$$\frac{d\mathbf{p}}{dt} = \frac{1}{2B}\left[\mathbf{k} - (\mathbf{k}\cdot\mathbf{p})\mathbf{p}\right] + \frac{1}{2}\boldsymbol{\omega}\times\mathbf{p} + \alpha\mathbf{p}\cdot\mathbf{E}\cdot\left[\mathbf{I} - \mathbf{pp}\right]. \tag{1}$$

where ω is the fluid vorticity, **E** is the rate of strain tensor, **I** is the identity matrix, t is time, B is the characteristic time a perturbed cell takes to return to its preferred orientation **k** if $\omega = 0$, and $\alpha = (\gamma^2 - 1)/(\gamma^2 + 1)$, where γ is the ratio of the cell's major to minor axes. The first term on the right hand side of Eqn. 1 parameterizes the tendency of the cell to remain pointed in its preferred direction **k** (usually in a direction parallel with gravity) and can be applied to regardless of the mechanism the cell uses for stabilization. The second term parameterizes the tendency of a cell to be overturned by vorticity, while the third term parameterizes the tendency for elongated cells to be aligned by fluid strain. The timescale, B, is known as the gyrotactic reorientation parameter and gives a measure of cell stability: a smaller B implies the cell is more resistant to perturbation by fluid shear. In the limit of ($B^{-1} = 0$), a cell has no preferred orientation and the classical Jeffery orbits (Jeffery 1922) are recovered. In simple shear, Jeffery's theory predicts that elongated particles rotate undergo periodic rotation, but tend to spend most of the time aligned in the direction of the flow. The orientation of non-motile cells, whose body morphology is often symmetric, can be analyzed in this limit (Karp-Boss and Jumars, 1998).

In marine systems, the depth of the euphotic zone places exerts a fundamental control on the proportion of the water column capable of supporting phytoplankton growth (Field *et al.* 1998). In the open ocean, concentrations of phytoplankton are often highest ~100 meters beneath the surface within structures known as the deep chlorophyll maximum, where gradients in light and nutrients overlap (Cullen, 1982). Light decreases exponentially from the surface, whereas nutrients are often more abundant in deeper waters (Ryan *et al.* 2010, Sullivan *et al.* 2010). The attenuation of light as it propagates through the water column is dictated largely by the light scattering characteristics of the

10

microbial life suspended within it. To estimate the fraction of incident light scattered in the forward direction (which propagates deeper into the water column) and in the backwards direction (which propagates back towards the surface), researchers have developed models to predict the scattering characteristics of the individual microbiological constituents of the water (Mobley and Stramski 1997, Stramski *et al.* 2001). However, frequent discrepancies between predictions and measurements highlight the need to better understand the complex underlying physics (Dall'Olmo *et al.* 2009).

In this thesis and appendix, we propose three biophysical mechanisms that rely on the interaction of phytoplankton morphology with fluid shear and demonstrate how they can drive thin phytoplankton layers, microscale cell aggregations, and induce changes in the Ocean light climate. Each of these mechanisms relies on the mathematical formulation given by Equation (1), although taken in different limits and under different flow conditions.

In chapter one, we show how a population of gyrotactic phytoplankton can become trapped within regions of enhanced shear to form 'thin layers,' a peculiar form of phytoplankton patchiness that occurs when a large number of photosynthetic cells aggregate within narrow horizontal bands of the water column. Thin phytoplankton layers are typically centimeters to meters in thickness and can contain cell concentrations up to two orders of magnitude above ambient. Our mechanism, which we call 'gyrotactic trapping' occurs when vertically migrating cells accumulate where vertical gradients in horizontal velocity exceeds a critical shear threshold, causing cells to tumble end over end. Using a combination of experiments, individual-based models, and continuum mathematical modeling, we show that gyrotactic trapping, is capable of triggering thin layers of phytoplankton in hydrodynamic conditions typical of where thin layers are routinely found.

This chapter has been published as:

Durham WM, Kessler, JO, and Stocker, R. (2009) Disruption of vertical motility by shear triggers formation of thin phytoplankton layers. *Science* 323: 1067-70.

In chapter two, we demonstrate that gyrotactic motility within two dimensional Taylor-Green vortex flow, often used as a simple analog for turbulent fluid motion, leads to tightly clustered aggregations of microorganisms. We show that two dimensionless numbers, characterizing the relative swimming speed and stability against overturning by shear, govern the coupling between motility and flow. Exploration of parameter space revealed a striking array of patchiness regimes, some of which were capable of producing significant levels of aggregation within only a few vortex overturning timescales.

This chapter has been published as:

Durham WM, Climent E, Stocker R. (2011) Gyrotaxis in a steady vortical flow. *Physical Review Letters* 106: 238102.

In chapter three, we build on the results of chapter two by showing that small-scale turbulent flows can drive the formation of tightly clustered aggregations of gyrotactic phytoplankton cells. We suggest that this mechanism may be responsible for the observation that motile phytoplankton are more heterogeneously distributed than non-motile cells at the millimeter to centimeter scales in Ocean. Using a cavity-driven vortical flow, we show the motile cells rapidly form highly clustered aggregations, whereas non-motile cells remain randomly distributed. To extend this to realistic turbulent flows, we implement a model of gyrotactic motility within an isotropic flow generated via Direct Numerical Simulation. We find that isotropic turbulence drives *de novo* aggregation in regions of downwelling and develop a simple metric that can be used to predict the level of aggregation.

This chapter will be submitted to a journal for publication in the coming weeks.

In Part One of the Appendix, we show that the tendency for cells with elongated morphologies to align in shear can affect the propagation of light through the upper ocean. The competition between fluid shear, which tends to align cells with the flow, and Brownian rotational diffusion, which tends to randomize the cell orientation, dictates the degree of alignment. To predict how light scattering by a microbial suspension is affected by shear, we developed a mathematical model that couples fluid dynamics and optics. We find that typical shear levels can increase optical backscatter of natural microbial assemblages by more than 20%. Our results imply that fluid flow, currently neglected in models of marine optics, may exert an important control on the marine light climate.

This chapter has been published as:

Marcos[*], Seymour J[*], Luhar M[*], Durham WM[*], Mitchell JG, Macke A, Stocker R[*]. (2011) Microbial alignment in flow changes ocean light climate. *Proceedings of the National Academy of Sciences USA* 108:3860-3864.

where [*] denotes shared first authorship.

In Part Two of the Appendix of this thesis contains a review of the literature on thin phytoplankton layers. In this contribution we review key findings from thin layer observations, describe proposed mechanisms of convergence and the methods used to decipher them in field observations, and discuss the ecological interactions of phytoplankton layers with higher trophic levels.

This paper has been published as:

Durham WM, Stocker R. (in press) Thin Phytoplankton Layers: Characteristics, Mechanisms, and Consequences. *Annual Review of Marine Science.*

References:

Bollens SM, Rollwagen-Bollens G, Quenette JA, Bochdansky AB. (2011) Cascading migrations and implications for vertical fluxes in pelagic ecosystems. *J. Plankton Res.* 33:349-255.

Bracco A, Provenzale A, Scheuring I. (2000). Mesoscale Vortices and the Paradox of the Plankton. *Proc. Roy. Soc. B.* 267: 1795-1800.

Brahamsha B. (1999) Non-flagellar swimming in marine *Synechococcus*. *J. Mol. Microbiol. Biotechnol.* 1:59-62

Cullen JJ. (1982) The deep chlorophyll maximum: comparing vertical profiles of chlorophyll *a*. *Can. J. Fish. Aquat. Sci.* 39:791-803.

Dall'Olmo G, Westberry TK, Behrenfeld MJ, Boss E, Slade WH (2009) Significant contribution of large particles to optical backscattering in the open ocean. *Biogeosci* 6:947–967.

Fenchel T. (1988) Marine Plankton Food Chains. *Annu. Rev. Ecol. Syst.* 19:19-38.

Fenchel T. (2001) How dinoflagellates swim. *Protist* 152:329-338

Field CB, Behrenfeld MJ, Randerson JT, Falkowski P. (1998) Primary Production of the Biosphere: Integrating Terrestrial and Oceanic Components. *Science* 281:237-240.

Guasto JS, Rusconi R, Stocker R. (2012) Fluid mechanics of planktonic microorganisms. *Annu. Rev. Fluid Mech.* 44.

Hardin G. (1960) The competitive exclusion principle. *Science.* 131:1292-1298.

Horner RA, Garrison DL, Plumley FG. (1997) Harmful algal blooms and red tide problems on the U.S. west coast. *Limnol. Oceano.* 42:1076-1088.

Jeffery GB. (1922) The motion of ellipsoidal particles immersed in a viscous fluid. *Proc. R. Soc. A.* 102:161 -179.

Karp-Boss L, Jumars P. (1998) Motion of diatom chains in steady shear flow. *Limnol. Oceanogr.* 43:1767–1773.

Mackas DL, Denman KL, Abbot MR. (1985) Plankton patchiness: biology in the physical vernacular. *Bull. Mar. Sci.* 37: 652-674.

Malkiel E, Alquaddoomi O, Katz J. (1999) Measurements of plankton distribution in the ocean using submersible holography *Meas. Sci. Technol.* 10: 1142–1152.

Martin AP. (2003) Phytoplankton patchiness: the role of lateral stirring and mixing. *Prog. Oceano.* 57: 125-174.

McCarren J, Brahamsha B. (2009) Swimming motility mutants of marine *Synechococcus* affected in production and locations of the s-layer protein swmA. *J. Bacteriol.* 191: 1111-1114.

Mitchell JG, Yamazaki H, Seuront L, Wolk F, Li H. (2008) Phytoplankton patch patterns: seascape anatomy in a turbulent ocean. *J. Mar. Syst.* 69:247-53.

Mobley CD, Stramski D (1997) Effects of microbial particles on oceanic optics: Methodology for radiative transfer modeling and example simulations. *Limnol Oceanogr* 42:550-560

Lasker R. (1975) Field criteria for survival of anchovy larvae: relation between inshore chlorophyll maximum layers and successful first feeding. *Fish. Bull.* 73:453-62.

Lebert M, Häder D-P. (1996) How *Euglena* tells up from down. *Nature.* 379:590.

Pedley TJ and Kessler JO. (1992) Hydrodynamic phenomena in suspensions of swimming microorganisms. *Annu. Rev. Fluid Mech.* 24:313-358.

Polin M, Tuval I, Drescher K, Gollub JP, Goldstein RE. (2009) *Chlamydomonas* Swims with Two "Gears" in a Eukaryotic Version of Run-and-Tumble Locomotion. *Science*, 325:487-490.

Kessler JO. 1985. Hydrodynamic focusing of motile algal cells. *Nature.* 313:218-20.

Richerson P, Armstrong R, Goldman CR. (1970) Contemporaneous disequilibrium, a new hypothesis to explain the "Paradox of the Plankton". *Proc. Natl. Acad. Sci. USA* 67:1710-1714.

Roberts AM, Deacon FM. (2002) Gravitaxis in motile micro-organisms: the role of fore-aft body asymmetry. *J. Fluid Mech.* 452:405-23.

Ryan JP, McManus MA, Sullivan JM. (2010) Interacting physical, chemical and biological forcing of phytoplankton thin-layer variability in Monterey Bay, California. *Cont. Shelf Res.* 30:7-16.

Smayda TJ. (1997) Harmful algal blooms: their ecophysiology and general relevance to phytoplankton blooms in the sea. *Limnol. Oceanogr.* 42:1137-1153.

Sournia A, Chrdtiennot-Dinet M-J, Ricard M. (1991) Marine phytoplankton: how many species in the world ocean? *J. Plankton Res.* 13:1093-1099.

Steele JH. (1974) Spatial heterogeneity and population stability. *Nature.* 248: 83.

Stramski D, Bricaus A, Morel A (2001) Modeling the inherent optical properties of the ocean based on the detailed composition of the planktonic community. *Appl Opt* 40:2929-2945.

Sullivan JM, Donaghay PL, Rines JEB. (2010) Coastal thin layer dynamics: consequences to biology and optics. *Cont. Shelf Res.* 30:50-65.

Tiselius P. (1992) Behavior of *Acartia tonsa* in patchy food environments. *Limnol. Oceanogr.* 37:1640-51.

Tiselius P, Jonsson PR, Verity PG. (1993) A model evaluation of the impact of food patchiness on foraging strategy and predation risk in zooplankton. *Bull. Mar. Sci.* 53:247-64.

CHAPTER 1

Disruption of vertical motility by shear
triggers formation of thin phytoplankton layers

William M. Durham[1], John O. Kessler[2], and Roman Stocker[1]*

[1]Department of Civil and Environmental Engineering, Massachusetts Institute of Technology, Cambridge, MA 02139, USA. [2]Department of Physics, University of Arizona, Tucson, AZ 85721, USA.

Thin layers of phytoplankton are important hotspots of ecological activity that are found in the coastal ocean, metres beneath the surface, and contain cell concentrations up to two orders of magnitude above ambient. Current interpretations of their formation favor abiotic processes, yet many phytoplankton species found in these layers are motile. We demonstrated that layers form when the vertical migration of phytoplankton was disrupted by hydrodynamic shear. This mechanism, which we call gyrotactic trapping, can be responsible for the thin layers of phytoplankton commonly observed in the ocean. These results reveal that the coupling between active microorganism motility and ambient fluid motion can shape the macroscopic features of the marine ecological landscape.

Advances in underwater sensing technology over the past three decades have revealed the occurrence throughout the oceans of intense assemblages of unicellular photosynthetic organisms known as thin layers. Thin layers are centimetres to metres thick (*1*) and extend horizontally for kilometres (*2*). They often occur in coastal waters (*1-4*), in regions of vertical gradients in density where they are partially sheltered from turbulent mixing (*1*), and can persist for hours to days (*2,5-7*). Thin phytoplankton layers contain elevated levels of marine snow and bacteria (*6,8*), enhance zooplankton growth rates (*7*) and provide the prey concentrations essential for the survival of some fish larvae (*9*). On the other hand, as many phytoplankton species found in these layers are toxic (*2,3,5,10,11*), thin layers can disrupt grazing, enhance zooplankton and fish mortality, and seed harmful algal blooms at the ocean surface (*2,5,10*). The large biomass found in thin layers can influence optical and acoustic signatures in the ocean (*1,6,8*). Understanding the mechanisms driving thin layer formation is critical for predicting their occurrence and ecological ramifications.

Phytoplankton species found in thin layers are often motile (*2,3,5,9,11*). The interplay between motility and fluid flow can result in complex and ecologically important phenomena, including localized cell accumulations (*12,13*) and directed swimming against the flow in zooplankton (*13*), bacteria (*14*) and sperm (*15*). Phytoplankton motility, coupled with shear, can lead to a striking focusing effect known as gyrotaxis (*12*). Shear, in the form of vertical gradients in horizontal fluid velocity, can be generated by tidal currents (*1*), wind stress (*1*) and internal waves (*16*), and is often enhanced within thin layers (*4,17*). Here we propose a mechanism for thin layer formation in which a

population of motile phytoplankton accumulates where shear exceeds a critical threshold: we have called this phenomenon gyrotactic trapping.

Many phytoplankton species exhibit gravitaxis, a tendency to swim upwards against gravity. Gravitaxis can result from a torque caused by asymmetry in shape (*18*), distribution of body density (*12*), or through active sensing (*19*). Hydrodynamic shear imposes a viscous torque on cells. The swimming direction θ is then set by the balance of viscous and gravitactic torques (Fig. 1A) and cells are said to be gyrotactic (*12*). Consider a spherical cell of radius a and mean density ρ (Fig. 1A), with an asymmetric density distribution creating an offset L between its centre of mass and its centre of buoyancy (an equivalent L can be used to characterise gravitaxis due to shape or sensing). When exposed to shear S, the cell swims upwards in the direction $\sin\theta = BS$ (*12*), where $B=3\mu/\rho Lg$ is the gyrotactic reorientation time scale, μ the dynamic fluid viscosity and g the acceleration of gravity. This results from the vorticity component of shear, whereas elongated cells would further be affected by the rate of strain component.

Here we show that vertical gradients ($S=\partial u/\partial z$) in horizontal velocity u can disrupt vertical migration of gyrotactic phytoplankton, causing them to accumulate in layers. When $|S|>S_{CR}=B^{-1}$, the stabilizing gravitational torque that acts to orient cells upwards is overwhelmed by the hydrodynamic torque that induces them to spin: upward migration is disrupted, because no equilibrium orientation exists ($|\sin\theta|$ must be ≤ 1), and cells tumble end over end, accumulating where they tumble (Fig. 1B). We demonstrated that gyrotactic trapping triggers layer formation by exposing the green alga *Chlamydomonas nivalis* and the toxic raphidophyte *Heterosigma akashiwo* (Figs. 2B,D), to a linearly varying shear $S(z)$ (Figs. 2B,D) in a 1 cm deep chamber (Fig. 1C). *C. nivalis* is a classic model for gyrotaxis (*12*), while *H. akashiwo* has been the culprit of numerous large-scale fish kills and is known to form thin layers (*11*).

In our experiments, *C. nivalis* consistently formed intense thin layers (Fig. 2A). The dynamics of thin layer formation were captured using video-microscopy (Fig. 3A). Initially ($t=6$ min, $x=11.5$ cm), cells entered the field of view with a broad distribution. Subsequently ($t=8.5$ min, $x=16.5$ cm), a 4 mm wide thin layer formed, as a result of the uppermost cells becoming trapped where $S_{CR}\approx 0.2$ s^{-1} and the cells beneath them still swimming upwards. The location of cell accumulation corresponded to a gyrotactic reorientation time $B=1/S_{CR}\approx 5$ s, in good agreement with previous literature values ($B\approx 1$-6 s; *20,21,22*). The thin layer grew more intense over time, peaking at $t=12$ min. Importantly, motility was critical for layer formation: no layers were observed to form when we used dead cells. *H. akashiwo* also produced thin layers, so intense that they were visible to the naked eye (Fig. 2C), at a depth corresponding to $S_{CR}\approx 0.5$ s^{-1}.

Was gyrotaxis the mechanism underlying layer formation? According to theory, the mean upward speed w of a population of gyrotactic cells decreases with increasing shear. Measured vertical profiles of $w(z)$ from 70,000 *C. nivalis* trajectories (Fig. 3B) strongly support the occurrence of gyrotactic trapping: $w(z)$ peaked at $S=0$ and decreased above and below. These observations were corroborated by numerical simulations of 50,000 cell trajectories under conditions mimicking the experiments (*23*). The simulations

16

resulted in the formation of an intense thin layer (Fig. 4A), with cell concentration $C(z)$ closely matching observations (Fig. 3A). Furthermore, $w(z)$ decayed with increasing S, as in experiments (Fig. 3B).

Gyrotactic trapping requires a transition in swimming kinematics when $|S|=S_{CR}$ for a thin layer to form. To verify the existence of this transition, we tracked individual *C. nivalis* cells. Trajectories clearly revealed two distinct regimes (Fig. 4B): for $|S|<S_{CR}$, cells swam upwards, whereas for $|S|>S_{CR}$ they tumbled. Numerical and experimental trajectories exhibited striking similarities in the amplitude and frequency of tumbles, the rate of upward swimming for $|S|<S_{CR}$, and the presence of cells temporarily expelled from the lower side of the layer only to swim back upward moments later.

Can gyrotactic trapping contribute to layer formation in the ocean, where vertical distances are of the order of meters and turbulence may destroy vertical heterogeneity? To find out, we developed a continuum model of cell concentration C in the upper 10 m of the ocean, starting with a uniform distribution and accounting for turbulence levels typical of thin layers (24) via a uniform eddy diffusivity $D = 10^{-5}$ m^{2}s^{-1}. Even for a conservatively low maximum upward swimming speed $w_{max}=100$ μm s^{-1} (11,25), phytoplankton began to accumulate just beneath the depth of maximum shear within three hours and the intensity of the layer strengthened over 12 hours, until the supply of phytoplankton from beneath the layer was exhausted (Fig. 5B). These time scales are consistent with field observations (7). Turbulent dispersion subsequently eroded the layer, reducing peak concentration by 50% after 30 hours. Consideration of a local reduction in eddy diffusivity, typically encountered at the pycnocline, further increases layer intensity and duration. Importantly, we predict layer formation for shear rates ($S=0.12$ s^{-1}) comparable to those observed in thin layers (up to $S=0.088$ s^{-1}) (1,4), particularly considering that the latter likely underestimate peaks in shear due to coarse (meter-scale) sampling (1,4). Furthermore, recent high-resolution measurements find S in excess of 0.5 s^{-1} in coastal waters (26), although the temporal coherence of these events remains to be determined.

Given the wide range of environmental conditions and species associated with thin layers, it is unlikely that a single mechanism is responsible for all layers (27). While several mechanisms have been hypothesized, including *in situ* growth (24), buoyancy (26), and motility towards optimal resource levels (5), straining of a phytoplankton patch by shear is currently the most invoked (4,16,24,27). Our findings offer an alternative explanation of the role of shear: regions of enhanced shear disrupt vertical motility and trigger sharp-peaked cell accumulations *ex novo* (Fig. 5B). This could occur routinely in natural water bodies, as many species of phytoplankton are gyrotactic (28). Contrary to straining, gyrotactic trapping predicts that a mixture of phytoplankton species with differing gyrotactic behaviour (e.g. B) will be sorted into multiple monospecific layers at different depths: such vertical species separation is often observed in the ocean (29) and can affect zooplankton foraging and the spread of viral epidemics.

Gyrotactic trapping suggests that stabilization against tumbling might represent an evolutionarily selected trait for vertically migrating phytoplankton species. The parameter B^{-1} measures a cell's stability against overturning by shear. While no stabilization ($B^{-1}=0$)
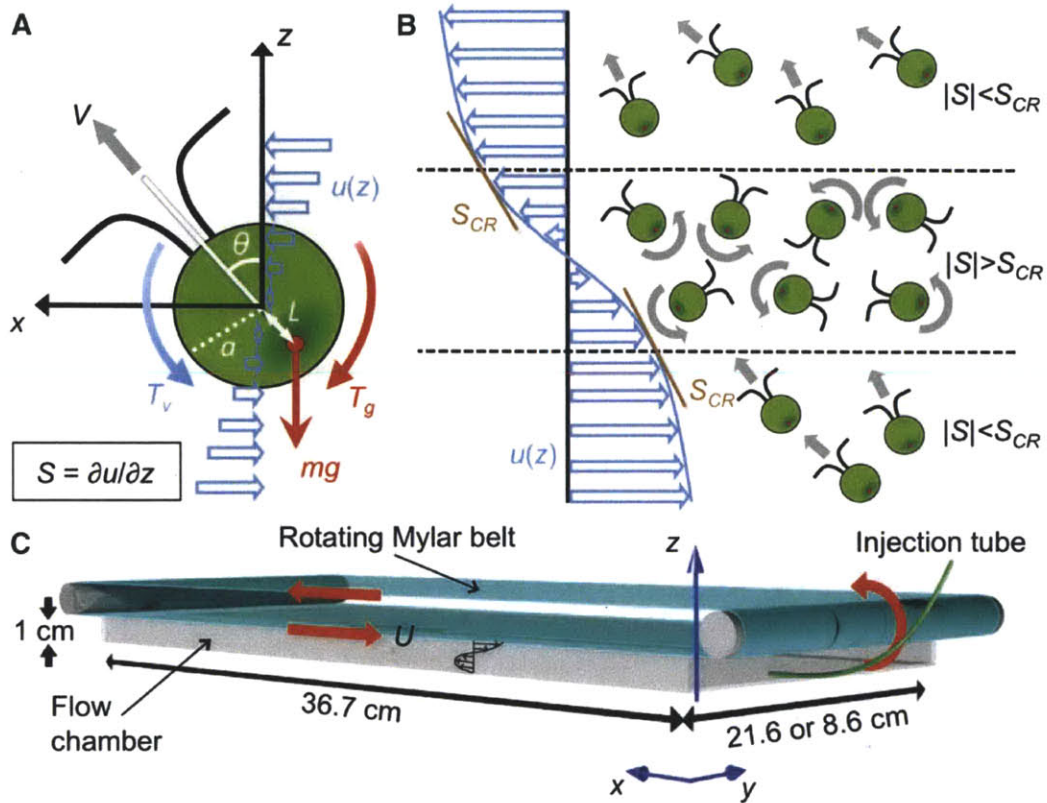
leaves the cell at the mercy of flow even at very small shear rates, stabilization is limited by biomechanical constraints (e.g. how bottom-heavy a cell can be) and excessive stabilization hinders manoeuvrability in exploiting nutrient patches and escaping predators. While a simple model suggests that biomechanical constraints are not the only determinants of cell stability (23), further investigation is needed to establish the importance of stabilization in determining cell morphology.

The importance of motility in governing the spatial distribution of microorganisms in the ocean has been emphasized in recent years, chiefly for bacteria navigating patchy distributions of organic matter (30,31). Here we have demonstrated that motility and shear can generate intense thin layer accumulations of phytoplankton by gyrotactic trapping. By focusing resources, thin layers shape ecological interactions and can significantly impact trophic transfer and biogeochemical fluxes (31). Our results reveal how prominent macroscopic features of the marine landscape can originate from the microscopic coupling between flow and the motility of some of its smallest inhabitants.

References and Notes:

1. M. M. Dekshenieks *et al.*, *Mar. Ecol. Prog. Ser.* **223**, 61-71 (2001).
2. T. G. Nielsen, T. Kiørboe, P. K. Bjørnsen, *Mar. Ecol. Prog. Ser.* **62**, 21-35 (1990).
3. D. W. Townsend, N. R. Pettigrew, A. C. Thomas, *Deep-Sea Res. II* **52**, 2603-2630 (2005).
4. J. P. Ryan, M. A. McManus, J. D. Paduan, F. P. Chavez, *Mar. Ecol. Prog. Ser.* **354**, 21-34 (2008).
5. P. K. Bjørnsen, T. G. Nielsen, *Mar. Ecol. Prog. Ser.* **73**, 263-267 (1991).
6. M.A. McManus *et al.*, *Mar. Ecol. Prog. Ser.* **261**, 1-19 (2003).
7. T. J. Cowles, R. A. Desiderio, M. Carr, *Oceanogr.* **11**, 4-9 (1998).
8. A. L. Alldredge *et al.*, *Mar. Ecol. Prog. Ser.* **233**, 1-12 (2002).
9. R. Lasker, *Fish. Bull.* **73**, 453-462 (1975).
10. P. L. Donaghay, T. R. Osborn, *Limnol. Oceanogr.* **42**, 1283-1296 (1997).
11. S. Yamochi, T. Abe, *Mar. Biol.* **83**, 255-261 (1984).
12. J. O. Kessler, *Nature* **313**, 218-220 (1985).
13. A. Genin, J. S. Jaffe, R. Reef, C. Richter, P. J. S. Franks, *Science* **308**, 860-862 (2005).
14. J. Hill, O. Kalkanci, J.L. McMurray, H. Koser, *Phys. Rev. Lett.* **98**, 068101 (2007).
15. F. P. Bretherton, L. Rothchild, *Proc. R. Soc. Lond.* **153**, 490-502 (1961).
16. P. J. S. Franks, *Deep-Sea Res. I* **42**, 75-91 (1995).
17. T. J. Cowles, in *Handbook of scaling methods in aquatic ecology: measurements, analysis, simulation*, L. Seuront, P. G. Strutton, Eds. (CRC Press, Boca Raton, 2003), pp. 31-49.
18. A. M. Roberts, F. M. Deacon, *J. Fluid Mech.* **452**, 405-423 (2002).
19. M. Lebert, D. P. Häder, *Nature* **379**, 590 (1996).
20. M. S. Jones, L. Le Baron, T. J. Pedley, *J. Fluid Mech.* **281**, 137-158 (1994).
21. N. A. Hill, D. P. Häder, *J. Theor. Biol.* **186**, 503-526 (1997).
22. T. J. Pedley, N. A. Hill, J. O. Kessler, *J. Fluid Mech.* **195**, 223-237 (1988).
23. See materials and methods below.
24. D. A. Birch, W. R. Young, P. J. S. Franks, *Deep-Sea Res. I* **55**, 277-295 (2008).
25. D. Kamykowski, R. E. Reed, G. J. Kirkpatrick, *Mar. Biol.* **4**, 319-328 (1992).

26. J. G. Mitchell, H. Yamazaki, L. Seuront, F. Wolk, H. Li, *J. Mar. Syst.* **69**, 247-253 (2008).

27. M. T. Stacey, M. A. McManus, J. V. Steinbuck, *Limnol. Oceanogr.* **52**, 1523-1532 (2007).

28. J. O. Kessler, *Prog. Phycol. Res.* **4**, 257–307 (1986).

29. L. T. Mouritsen, K. Richardson, *J. Plankton Res.* **25**, 783-797 (2003).

30. R. Stocker, J. R. Seymour, A. Samadani, D. E. Hunt, M. F. Polz, *Proc. Natl. Acad. Sci.* **105**, 4209-4214 (2008).

31. F. Azam, F. Malfatti, *Nature Rev. Microbiol.* **5**, 782-791 (2007).

Fig. 1. Gyrotactic trapping. **(A)** A gyrotactic phytoplankton's center of mass (red) is displaced from its center of buoyancy ($x=z=0$). As a result, the swimming direction θ in a shear flow, $u(z)$, is set by the balance of gravitational (T_g) and viscous (T_v) torques. V is swimming speed and m is mass. **(B)** Schematic of gyrotactic trapping. Cells can migrate vertically at low shear, but tumble and become trapped where $|S|>S_{CR}$, accumulating in a thin layer. **(C)** Experimental apparatus to test gyrotactic trapping. The rotating belt generated a depth-varying shear $S(z)$ in the underlying flow chamber.
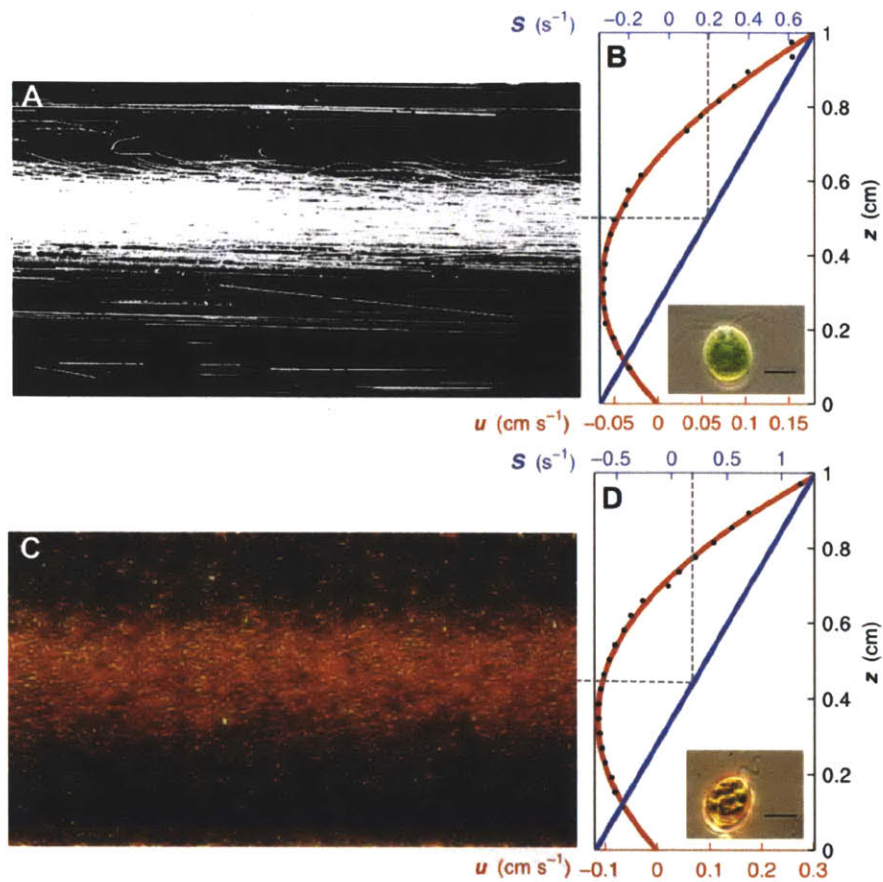
Fig. 2. Thin phytoplankton layers. **(A)** Multiple-exposure image showing a thin layer of *Chlamydomonas nivalis* (t=12 min, x=21.5 cm). Cells in high shear (z>0.5 cm) were trapped, while those beneath ($|S|<S_{CR}$) swam upwards, forming a thin layer. **(B)** Corresponding profile of measured flow velocities u (black dots), along with a quadratic fit (red) and the associated shear $S=\partial u/\partial z$ (blue). As $u(z)$ was parabolic, S increased linearly with z. **(B inset)** *C. nivalis,* showing the two flagella used for swimming. Bar = 10 μm. **(C)** Thin layer of *Heterosigma akashiwo.* **(D)** Same as b, for experiments in Fig. 2C. **(D inset)** *H. akashiwo*, showing one flagellum (a second resides in a ventral groove). Bar = 10 μm.
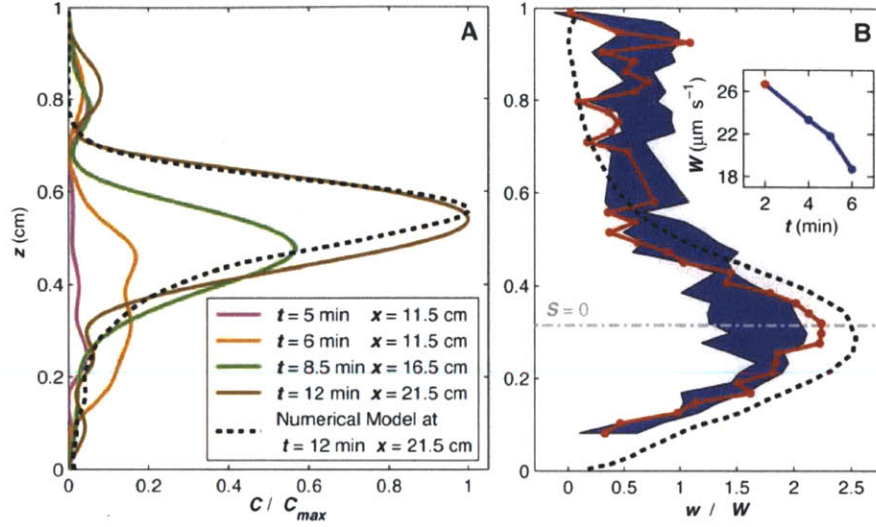
Fig. 3. Formation of a thin layer. **(A)** Cell concentration profiles $C(z)$ observed experimentally (solid lines) and numerically (dashed line), normalized by C_{max} observed at t=12 min, x=21.5 cm. **(B)** Upward swimming speed w at t=2 min (red line) and standard deviation across four observations (blue strip and inset). W is the depth-averaged value of w. The dashed line shows the numerical simulation. The peak in $w(z)$ at $S \approx 0$ (grey line) and the deterioration in $w(z)$ for $|S| > 0$ are consistent with gyrotaxis and were responsible for layer formation. **(B inset)** W decreased with time, as the proportion of cells reaching their critical shear rate increased.
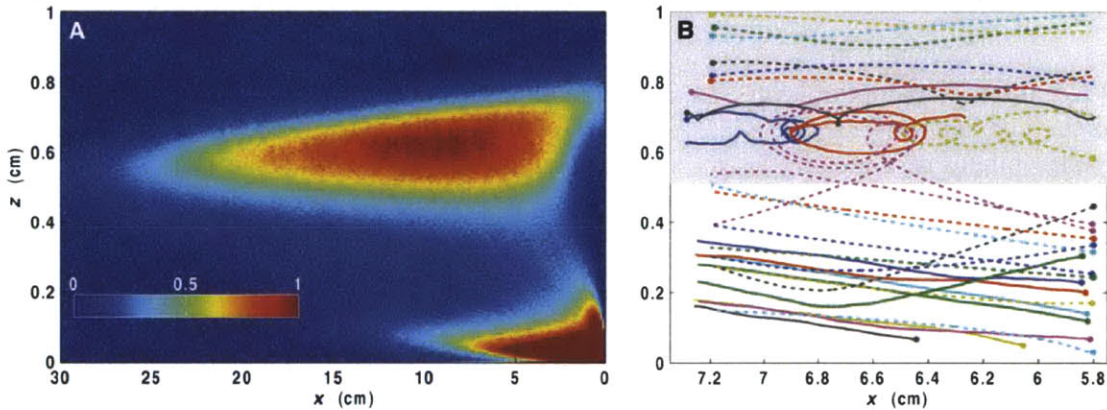
Fig. 4. Cell accumulation and trajectories. **(A)** Thin layer obtained from the numerical model at t=12 min for conditions that simulated experiments with *C. nivalis* (Fig. 3A). Color denotes normalized cell concentration (the high concentrations at the lower right represent the region of injection). **(B)** Transition between two swimming regimes, demonstrated by experimental (solid) and numerical (dashed) trajectories. Where $|S| < S_{CR}$ (white background) cells migrated upwards, while $|S| > S_{CR}$ (grey background) triggered tumbling and trapping. Shading represents the mean critical shear rate S_{CR}=0.2 s^{-1}, though a statistical variability existed among cells. Dots mark beginning of trajectories.

22
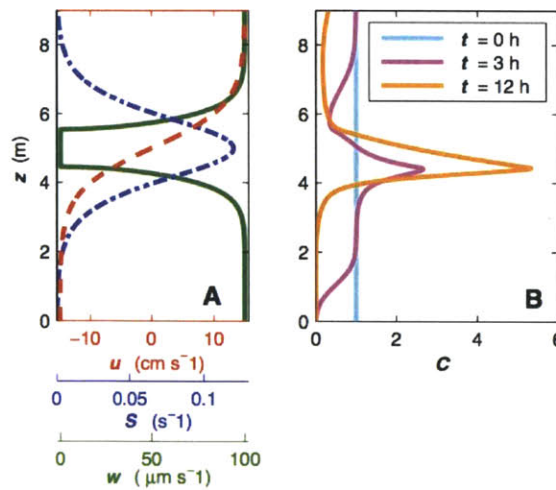
Fig. 5. Thin layer formation by gyrotactic trapping in the ocean. **(A)** A flow velocity profile (red line) typical of regions where thin layers are observed (*1,4*) was used in a continuum model to predict the effect of gyrotactic trapping in the ocean. Enhanced shear $S=\partial u/\partial z$ (blue line) triggers a reduction in upward swimming speed w (green line). **(B)** The model shows that an initially uniform population (cyan line) develops a localized accumulation within 3 hours (pink line) and forms an intense thin layer within 12 hours (orange line). Turbulence was parameterized by a vertical eddy diffusivity $D=10^{-5}$ m^{2}s^{-1}.

SUPPLEMENTARY MATERIAL

Materials and Methods

Experimental setup

The lid-driven cavity flow was produced by the rotation of a Mylar belt driven by a DC motor, generating a recirculating flow in the underlying Plexiglas flow chamber. The latter was h=1 cm deep, 36.7 cm long and 21.6 or 8.6 cm wide (for *C. nivalis* and *H. akashiwo*, respectively). The belt speed U was 0.18 cm s^{-1} (*C. nivalis*) or 0.30 cm s^{-1} (*H. akashiwo*). Tracking of non-motile particles yielded the velocity profile, $u(z)$, which was found to be quadratic in z, giving a linear $S(z)$. Dye injection studies verified the flow was two-dimensional and laminar (Reynolds number $=Uh/v$=18-30, where v=1.0x10^{-6} m^{2}s^{-1} is the kinematic viscosity).

To prevent thermal convection, the flow chamber was submerged in a 20 l acrylic tank filled with deionized water, with addition of 31 g/l of Ultramarine Synthetica sea salt (Waterlife Industries) for *H. akashiwo*. Residual thermal convection was negligible (<5 μm s^{-1}) compared to upward swimming speed (60 μm s^{-1}). Phytoplankton cultures were injected into the flow chamber using PEEK tubing (Upchurch Scientific; 0.76 mm inner diameter). In thin layer experiments, cultures were continuously injected into the flow chamber (at $x=z=0$, $y=3.6$ cm) with negligible entrainment at 1.7 nl s^{-1} using a syringe pump (Harvard Apparatus). In experiments to measure w, a culture was instantaneously

23

injected into the flow chamber manually: the resulting entrainment spread phytoplankton uniformly over the depth. The flow disturbance decayed within 2 min, after which data collection began.

Two sources of light were used. Illumination for imaging purposes (40 μE $m^{-2}s^{-1}$; in the y-direction) was generated by a slide projector (AF-2, Kodak) fitted with an infrared cut-off filter (HA-30, Hoya Optics). To ensure cells reached the depth at which $S=S_{CR}$ before being advected to the end of the chamber, the cells' natural tendency to swim upwards was enhanced by inducing negative phototaxis using an overhead projector (Model 213, 3M; 2.2 mE $m^{-2}s^{-1}$, in the z-direction) without the upper mirror assembly. Analogous to the negative phototaxis in our experiments, in the ocean low-intensity light from above promotes upwards motility via positive phototaxis.

Data acquisition

In *C. nivalis* experiments, a CCD camera (PCO 1600, Cooke) was attached to a rail-mounted microscope (SMZ1000, Nikon) that could translate along x. The 1.13x1.51 cm^2 field of view was focused at $y=3.6$ cm. Experiments on thin layer formation were repeated four times by recording 150-frame sequences at 13 frames/s (a 'movie') at different x and t. Image analysis (IPLab, BD; Matlab, The Mathworks) yielded cell positions and thus vertical cell concentration profiles $C(t,z)$. The first such profile (Fig. 3A, pink line), taken while no cells were in the field of view, yielded a nearly uniform distribution of passive debris, small amounts of which were unavoidable in the flow chamber. Thin layers of *H. akashiwo* were imaged with an eight-megapixel DSLR camera (EOS20D, Canon) attached to the microscope and experiments were repeated four times.

In experiments with *C. nivalis* to measure w, four 500-frame movies (32 frames/s) were recorded over 6 min at $x=13.5$ cm. Cell trajectories were reconstructed using in-house designed cell-tracking software (BacTrack). Ambient flow was subtracted from each trajectory and non-motile cells and inert particles were excluded from the analysis by retaining only trajectories with mean speed >32 μm s^{-1}. The mean and standard deviation of w over all trajectories were calculated in 50 discrete bins equally spaced over h. Bins with fewer than 30 trajectories were omitted.

In experiments with *C. nivalis* to detect the transition in swimming kinematics, 900-frame movies (3.3 frames/s) were recorded. Rotation of cells about their axes caused intermittent blinking, preventing automated tracking. To obtain sufficiently long trajectories (>45 s) to observe tumbles, cell positions were digitized manually using ImageJ (NIH) with the Manual Tracking plug-in (F. Cordelieres, Institut Curie).

24

Phytoplankton

C. nivalis was grown by inoculating 2 ml of exponential phase culture in 25 ml of Bold 1NV medium (*S1*), then incubating at 25°C under continuous fluorescent illumination (70 $\mu E\ m^{-2}s^{-1}$). Cells were harvested after 21 days (1.1×10^6 cells/ml) and directly used in experiments. On average, cells had a radius of $a=6.1$ μm and swam at $V=81$ $\mu m\ s^{-1}$. In control experiments, cells were killed with ethanol (10% v/v), centrifuged at 7750g for 5 min, and the pellet was resuspended in Bold 1NV medium to achieve the same density and cell concentration as the live cell culture.

H. akashiwo was grown by inoculating 2 ml of exponential phase culture in 25 ml of O3 medium (*S2*), then incubating at 25°C under continuous fluorescent illumination (70 μE $m^{-2}s^{-1}$). Cells were harvested after 21 days and their concentration was increased five-fold (to 1.0×10^7 cells/ml) by centrifugation at 550g for 5 min. Cells had $a=7$ μm and $V=84$ μm s^{-1}.

Individual-based model

To support experimental observations, we developed an individual-based model mimicking experimental conditions. Two-dimensional numerical cell trajectories were obtained by integrating the discretized equations of motion (*S3,S4*):

$$\omega_k^{n+1} = \frac{1}{2}\left(S(z_k^n) - \sin\theta_k^n / B_k \right)$$

$$\theta_k^{n+1} = \theta_k^n + \omega_k^{n+1}\Delta t + \Delta\theta$$

$$x_k^{n+1} = x_k^n + \left(V_k \sin\theta_k^{n+1} + u(z_k^n) \right)\Delta t$$

$$z_k^{n+1} = z_k^n + V_k \cos\theta_k^{n+1}\Delta t$$

where $\omega = \partial\theta/\partial t$ is the cell's angular velocity, with a forward Euler scheme (*S4*) implemented in Matlab. The equations provide the updated (time step $n+1$) position (x,z,θ) of a given cell, k, using its position at time step n. Cells were released at $x=z=0$ with a random initial orientation θ and tracked over time with a time step $\Delta t = 0.1$ s (convergence was successfully tested using $\Delta t = 0.01$ s). Experimental measurements were used for $u(z)$ and $S(z)$ (Fig. 2B). Each cell was assigned values of B and V drawn from measured distributions for *C. nivalis*. The distribution of B (=$3\mu/\rho Lg$) was computed by assuming $\mu=1.0 \times 10^{-3}$ kg m^{-1}s^{-1} (for freshwater at 20°C), $\rho = 1050$ kg m^{-3} and $L/a = 0.01$ (S3), where the distribution of cell radii a (6.1 ± 1.2 μm) was directly obtained by image analysis of 609 *C. nivalis* cells. This resulted in $B = 5.0 \pm 1.3$ s, comparable to previous estimates for this species (~1-6 s; *S5-7*). The distribution of swimming speeds V (81 ± 46 μm s^{-1}) was measured from 17,000 trajectories using BacTrack. At each time step, randomness in swimming direction was modelled as a random change in direction $\Delta\theta = \pm(2D_R\Delta t)^{1/2}$ with a rotational diffusivity $D_R=0.01$ s^{-1} (*S8*). To compare layer formation

with experiments, cells were continuously released and $C(z)$ was constructed from cell positions at $t=12$ min, $x=21.5$ cm (Fig. 3A). To measure $w(z)$, cells were instantaneously released uniformly over depth, as in the experiments, and w was recorded over 2 min in 50 vertical bins.

Continuum model

To predict layer formation by gyrotactic trapping in the ocean, we developed a mathematical model. The velocity profile $u(z)=u_o\tanh[(z-z_o)/\delta]$ was assumed to have a smooth transition of thickness $\delta=1.25$ m at depth $z_o=5$ m between two fluid layers moving in opposite directions at speed $u_o=15$ cm s^{-1}, mimicking velocity profiles recorded in the ocean (*S9,S10*) and yielding $S(z)=(u_o/\delta)\text{sech}^2[(z-z_o)/\delta]$. Combining this with $\sin\theta=BS$ results in the upward swimming speed $w(z)=w_{max}\{1-[(Bu_o/\delta)^2 \text{sech}^4((z-z_o)/\delta)]\}^{1/2}$ (Fig. 5A), where w_{max} is the upward swimming speed in the absence of shear. Where $|S|>S_{CR}$, $w=0$ (tumbling regime). Cell concentration profiles $C(t,z)$ were obtained by numerically integrating the advection-diffusion equation $C_t = - (Cw)_z + DC_{zz}$ (subscripts denote differentiation), where the advective component is generated by swimming, with no-flux boundaries at $z=0$ and 10 m, and a vertical eddy diffusivity $D=10^{-5}$ m^{2}s^{-1}. Our choice of $w_{max}=100$ μm s^{-1} is conservative, as many species of phytoplankton have $w_{max}>350$ μm s^{-1} (*S11, S12*), resulting in faster and more intense layer formation. We used $B=10.0$ s in simulations, resulting from $\mu=1.4\times10^{-3}$ kg m^{-1}s^{-1} (for salt water at 10°C), $\rho=1070$ kg m^{-3}, $a=4$ μm and $L/a=0.01$ (*S3*). We note that turbulence also contains vorticity, like the region of enhanced shear, but turbulent vorticity does not cause cell accumulation because it varies randomly in space and time.

Biomechanical Stability Model

To estimate a cell's maximal resistance to overturning by shear we developed a simple model for the stability of a bottom-heavy cell. Bottom-heaviness can arise from dense organelles (e.g. starch-rich chloroplasts) residing off-centre in the cell (*S3*). We considered a spherical cell of radius a comprised of a less dense hemisphere (ρ_L) and a more dense hemisphere (ρ_H), giving a mean cell density $\rho=(\rho_L+ \rho_H)/2$. This results in a distance between the centre of buoyancy and the centre of mass of $L=(3a/8)(\rho_H -\rho_L)/(\rho_H +\rho_L)$. Considering a *C. nivalis* cell ($a=6.1$ μm; $\rho=1050$ kg m^{-3} (*S3*)), which has a single large chloroplast occupying the posterior side of the cell (*S13, S14*), and using a typical chloroplast density of $\rho_H=1100$ kg m^{-3} (*S15*), one obtains $L=0.018a$ and thus $B=\rho Lg/3\mu=2.7$ s. For $\rho_H=1127$ kg m^{-3} (*S15*) one finds $B=1.7$ s. If one instead models the chloroplast as a 4.1 μm radius sphere ($\rho_H=1127$ kg m^{-3}) located 2 μm off-center, B is 4.5 s. These estimates are smaller than our measured value ($B\approx5$ s), suggesting that the stability of *C. nivalis* is not limited by biomechanical constraints but also influenced by other factors, like manoeuvrability. However, in light of the significant variability in the predictions, reflecting the uncertainty in chloroplast density and cell morphology, one

26

cannot at present reach a definitive conclusion, and this model provides primarily a framework to evaluate cell stability. It must further be noted that this model holds for bottom-heavy cells, but there are other mechanisms for gravitactic reorientation, such as shape anisotropy (*S16*), flagellar drag (*S7*) and active sensing (*S17*), each of which can result in gyrotactic trapping.

Supporting Material References

S1. R. C. Starr, J. A. Zeikus, *J. Phycol.* **29**, Suppl, 1-106 (1993).

S2. L. McIntosh, R. A. Cattolico, *Anal. Biochem.* **91**, 600-612 (1978).

S3. J. O. Kessler, *Nature* **313**, 218-220 (1985).

S4. M. M. Hopkins, L. J. Fauci, *J. Fluid Mech.* **455**, 149-174 (2002).

S5. N. A. Hill, D. P. Häder, *J. Theor. Biol.* **186**, 503-526 (1997).

S6. T. J. Pedley, N. A. Hill, J. O. Kessler, *J. Fluid Mech.* **195**, 223-237 (1988).

S7. M. S. Jones, L. Le Baron, T. J. Pedley, *J. Fluid Mech.* **281**, 137-158 (1994).

S8. A. M. Roberts, in *Swimming and Flying in Nature.* T. Wu, C. J. Brokaw, C. Brennan, Eds. (Plenum Press, New York, 1975), pp. 377-394.

S9. M. M. Dekshenieks *et al., Mar. Ecol. Prog. Ser.* **223**, 61-71 (2001).

S10. J. P. Ryan, M. A. McManus, J. D. Paduan, F. P. Chavez, *Mar. Ecol. Prog. Ser.* **354**, 21-34 (2008).

S11. S. Yamochi, T. Abe, *Mar. Biol.* **83**, 255-261 (1984).

S12. D. Kamykowski, R. E. Reed, G. J. Kirkpatrick, *Mar. Biol.* **4**, 319-328 (1992).

S13. B. Eddie, C. Krembs, S. Neuer, *Mar. Ecol. Prog. Ser.* **354**, 107-117 (2008).

S14. T. Müller, W. Bleiß, C-D. Martin, S. Rogachewski, G. Fuhr, *Polar Biol.* **20**, 14-32 (1998).

S15. J. L. Salisbury, A. C. Vasconcelos, G. L. Floyd, *Plant Physiol.* **56**, 399-403 (1975).

S16. A. M. Roberts, F. M. Deacon, *J. Fluid Mech.* **452**, 405-423 (2002).

S17. M. Lebert, D-P. Häder, *Nature.* **379**, 590 (1996).

CHAPTER 2

Gyrotaxis in a steady vortical flow

William M. Durham,[1] Eric Climent[2] and Roman Stocker[1]

[1] Department of Civil and Environmental Engineering, Massachusetts Institute of Technology, 77 Massachusetts Avenue, Cambridge, Massachusetts 02139, USA

[2] Institut de Mécanique des Fluides, Université de Toulouse, INPT–UPS–CNRS, Allée du Pr. Camille Soula, F-31400 Toulouse, France

We show that gyrotactic motility within a steady vortical flow leads to tightly clustered aggregations of microorganisms. Two dimensionless numbers, characterizing the relative swimming speed and stability against overturning by vorticity, govern the coupling between motility and flow. Exploration of parameter space reveals a striking array of patchiness regimes. Aggregations are found to form within a few overturning timescales, suggesting that vortical flows might be capable of efficiently separating species with different motility characteristics.

Spatial heterogeneity, or 'patchiness', in the distribution of organisms affects important ecological processes, including competition, predation, the spread of epidemics, and the maintenance of species diversity [1]. We report on a biophysical mechanism that rapidly generates small-scale patchiness in the distribution of microorganisms and might have implications for marine phytoplankton. These unicellular, photosynthetic organisms are responsible for half of the world's oxygen production [2] and represent the base of the oceans' food web [3]. Patchiness in the distribution of phytoplankton is strongly coupled to ecosystem productivity [4] and has been found to extend down to centimeter scale [5-9].

Active locomotion is used by many organisms to achieve and maintain advantageous positions with respect to resources, predators, and each other, thereby conferring enhanced fitness [10]. Although many marine microorganisms are motile, their motility is often neglected because swimming speeds are typically smaller compared to ambient flow speeds. Using a well-established flow model, we show that a coupling between motility and vortical fluid motion can drive aggregations of gyrotactic cells, with a rich diversity of steady-state cell distributions.

Motile phytoplankton often swim in a preferred direction, k (typically vertical, to perform daily migration through the water column), owing to a stabilizing torque that can arise from an asymmetry in shape [11] or body density [12], or the ability to sense the direction of gravity [13]. In moving fluids, cells further experience rotation due to

gradients in velocity and cells are said to be gyrotactic [12] (Fig. 1(a)). Modeling cells as prolate ellipsoids, their swimming direction, **p**, is governed by [14]

$$\frac{d\mathbf{p}}{dt^*} = \frac{1}{2B}\left[\mathbf{k} - (\mathbf{k}\cdot\mathbf{p})\mathbf{p}\right] + \frac{1}{2}\boldsymbol{\omega}^* \times \mathbf{p} + \alpha\mathbf{p}\cdot\mathbf{E}^* \cdot \left[\mathbf{I} - \mathbf{pp}\right]. \tag{1}$$

Starred quantities indicate dimensional variables: $\boldsymbol{\omega}^*$ is the fluid vorticity, $\mathbf{E}^*$ is the rate of strain tensor, $\mathbf{I}$ is the identity matrix, t^* is time, B is the characteristic time a perturbed cell takes to return to orientation $\mathbf{k}$ if $\boldsymbol{\omega}^* = 0$, and $\alpha = (\gamma^2 - 1)/(\gamma^2 + 1)$, where γ is the ratio of the cell's major to minor axes. For phytoplankton, $B \sim 1 - 10$ s, with the uncertainty stemming from the paucity of data [15-17]. When there is no preferred swimming direction ($B^{-1} = 0$) Jeffery orbits [18] are recovered. Equation 1 applies to organisms much smaller than the scale of ambient velocity gradients, which allows cells to be modeled as point particles.

The study of particle motion in vortical flows has a rich history, partly due to its importance in marine [19] and atmospheric [20] processes. Though many models of vortical flow exist, the Taylor-Green vortex flow (TGV; [21]) has been widely used [19, 20, 22], largely because of its tractability. The TGV flow is a two-dimensional array of steady, counter-rotating vortices (Fig. 1(b)), with spacing L and maximum vorticity ω_0 at the center of vortices. The nondimensional velocity $\mathbf{u} = [u, 0, w]$ and vorticity $\boldsymbol{\omega} = [0, \omega, 0]$ fields are given by $u = -\frac{1}{2}\cos x \sin z$, $w = \frac{1}{2}\sin x \cos z$, and $\omega = -\cos x \cos z$, where lengths, velocities and vorticities are non-dimensionalized by $1/m$, ω_0/m and ω_0, respectively, and $m = 2\pi/L$.

To determine how populations of gyrotactic cells might respond to vortical flows, we computed the trajectories of individual gyrotactic organisms swimming at constant speed V_C within a TGV flow (phytoplankton can swim at up to $V_C = 3$ mm s^{-1} [7]). The nondimensional equations of motion for a cell are then

$$\frac{d\mathbf{p}}{dt} = \frac{1}{2\Psi}\left[\mathbf{k} - (\mathbf{k}\cdot\mathbf{p})\mathbf{p}\right] + \frac{1}{2}\boldsymbol{\omega}(\mathbf{X}) \times \mathbf{p} + \alpha\mathbf{p}\cdot\mathbf{E}(\mathbf{X})\cdot\left[\mathbf{I} - \mathbf{pp}\right], \tag{2}$$

$$\frac{d\mathbf{X}}{dt} = \Phi\mathbf{p} + \mathbf{u}(\mathbf{X}), \tag{3}$$

where $\mathbf{X} = [x, y, z]$, $\Psi = B\omega_0$, $\Phi = V_C m/\omega_0$, and time was non-dimensionalized by $1/\omega_0$. We neglected the effect of cells on flow.

We first considered spherical cells ($\alpha = 0$) swimming within a vertical plane (x-z), for which equation 2 becomes $d\theta/dt = -\frac{1}{2}(\cos x \cos z + \sin\theta/\Psi)$ [12], where θ is the swimming direction relative to the vertical (Fig. 1(a)). With these assumptions, the two parameters, Φ and Ψ, fully control the fate of the cells. Φ measures the swimming speed relative to

the flow speed and Ψ is a measure of orientational stability; if $\omega\Psi > 1$ the cell can be overturned by vorticity [17] (red circles, Fig. 1(c)).

We find that the spatial distribution of gyrotactic cells in vortical flow is highly dependent upon Ψ and Φ. We begin by comparing trajectories of three cells with different Ψ and Φ parameters, all initialized with the same orientation and position (Fig. 1(b)). The slow, intermediately stable red cell ($\Phi = 0.2$, $\Psi = 1$) spirals inwards towards a single point, the fast and stable green cell ($\Phi = 20$, $\Psi = 0.1$) rapidly finds an upward path, whereas the slow and unstable blue cell ($\Phi = 0.5$, $\Psi = 100$) wanders aimlessly. These strikingly different behaviors highlight the complex interaction between motility and flow and suggest the existence of multiple regimes of phytoplankton aggregation in vortical flows.

A systematic exploration of Φ–Ψ parameter space revealed ten distinct, time-invariant patchiness regimes (Fig. 2; at $t = 2000$). The strongest aggregation occurs when all cells converge to points where the equilibrium cell orientation is such that motility exactly balances flow ($d\theta/dt = dx/dt = dz/dt = 0$; Figs. 1(c), 2(b,c)). This can occur at either a single point ($x = \pi/2$, $z = \cos^{-1}(-2\Phi)$; Fig. 2(b)) or two points ($x = \cos^{-1}(\pm\Gamma^{1/2})$, $z = \tan^{-1}(-2\Psi\Phi)$, $\Gamma = (16\Psi^2\Phi^4 + 4\Phi^2 - 1)/(4\Psi^2\Phi^2 - 1)$; Figs. 1(c), 2(c)) within each vortex.

Gyrotactic cells are known to collect in downwelling regions ($w<0$) and retreat from upwelling regions ($w>0$) [12], a mechanism that was suggested to produce accumulation in turbulent flows [24]. We recover accumulation in downwelling regions in the 'vertical migrator' regime (Fig. 2(d)), in which cells focus into vertical bands between vortices and swim upwards ($x = \pm\pi/2$, $\theta = 0$). Though these cells traverse both upwelling and downwelling regions, convergence prevails because cells spend more time in regions where swimming and flow oppose one another.

In contrast with earlier predictions [24], accumulation in downwelling regions is only one of many possible patterns of aggregation: a multitude of patterns arise in Φ–Ψ parameter space (Fig. 2). Unstable cells ($\Psi>1$) are more susceptible to being rotated by vorticity. Slow unstable cells ($\Phi<0.3$) are unable to escape vortices, leading to closed trajectories (Fig. 2(e)). In contrast, fast unstable cells ($\Phi>0.3$) are locally reoriented by vorticity, but can escape from vortices. They weave from one vortex to the other, producing diverse patterns (Fig. 2(g, i, j)), including some peculiar figure eights (Fig. 2(h,k)). Finally, very fast unstable cells ($\Phi>2$) have little time to be deflected by vorticity and can move diagonally in addition to vertically upwards (Fig. 2(f)). Although for slow swimmers ($\Phi<1$) there exist regimes where accumulation patterns did not emerge (Fig. 2(m)) or converge (Fig. 2(l)) by $t = 2000$, the diversity of accumulation patterns and their occurrence over a wide range of parameter space indicate that strong patchiness of gyrotactic cells is the norm within vortical flows, rather than the exception.

In addition to producing patchiness, vortical flow can stifle vertical migration. This effect can be quantified using the normalized vertical migration rate, $W = <dz/dt>/\Phi$, defined as the net upward speed of a cell averaged over all cells and over time ($t = 0$–10), normalized by Φ (Fig. 3(c)). The upward movement of stable cells ($\Psi<1$) is largely

unaffected by flow (W~1). In contrast, vertical migration of unstable cells (Ψ>1) is severely impeded (W<<1), showing that vortical flow can trap gyrotactic cells at depth. The suppression of vertical migration is in line with both a simple scaling analysis [25] and simulations utilizing more complex flow fields [26].

To quantify patchiness, we partitioned the domain into a 15×15 grid of boxes and computed the box occupancy function, $f(n)$ [27], where n is the number of cells in a box (with mean λ). As cells accumulate in some boxes and leave others empty, the standard deviation of $f(n)$, σ, increases relative to its initial (Poisson) value, σ_P ($=\lambda^{1/2}$). Thus, the accumulation index $N = (\sigma - \sigma_P)/\lambda$ is a measure of patchiness [27]. Fig 3(a) shows N in Φ–Ψ space at $t = 10$. Cells with motility faster than the flow (Φ>0.5) and intermediate stability (Ψ~1) exhibit marked patchiness by $t = 10$, hence accumulation by this mechanism can be rapid (within a few vortex time scales). Cells that accumulate the most swiftly belong primarily to the 'vertical migrator', 'equilibrium', and 'skater' regimes (Fig. 2). This is also observed by computing the time, τ, required for a randomly distributed population to reach a time-invariant spatial distribution. The latter was calculated by fitting $N(t)$ with the exponential $\kappa (1 - e^{-t/\tau})$, where κ is a constant. The same region of parameter space (Φ>0.5, Ψ~1) exhibits the fastest accumulation (Fig. 3(b)). These findings are readily rationalized: to accumulate, cells must swim across streamlines. Fast swimmers are able to make significant progress across streamlines, while intermediate stability represents a trade-off between persistent tumbling (Ψ>>1), which negates directed swimming, and excessive stability (Ψ<<1), which prevents cell orientation from being perturbed by the flow.

These findings assume that the fluid vorticity is orthogonal to the preferred swimming direction, **k**. To determine the effect of vortex orientation, we performed three-dimensional (3D) simulations for spherical cells ($\alpha = 0$) by extruding the TGV flow in the **y**-direction and allowing **k** to assume any orientation, prescribed by polar and azimuthal angles (η, β). The swimming direction was computed using equations 2 and 3. When **k** = **z** ($\eta = \beta = 0$), the x-z projection of the 3D time-invariant cell distribution is identical to the 2D simulation. As one varies **k**, additional patchiness regimes emerge compared to Fig. 2. Patchiness occurs over all orientations of **k**, with the exception of a small region about **k** = **y** ($\eta = \beta = \pi/2$; Fig. 4(a)), where cell orientation is unaffected by flow ($\omega \times \mathbf{k} \approx 0$). Thus, the proposed patch generation mechanism is robust when cells are permitted to swim within three-dimensional space.

Phytoplankton morphology is highly diverse: many species have non-spherical cell bodies [28] or flagella that alter their effective eccentricity [29]. Elongated swimming particles in TGV flow, in the absence of a preferential swimming direction (Ψ=∞), have been shown to aggregate along flow separatrices [30]. We determined how elongation influences the aggregation of gyrotactic cells for ten values of Ψ and Φ (Fig. 2(a), symbols), for each of them varying the cell aspect ratio, γ, from 1 to 100. Cells were confined to the x-z plane, hence equation 2 simplifies to $d\theta/dt = \frac{1}{2}(\alpha \sin x \sin z \sin 2\theta - \sin\theta/\Psi - \cos x \cos z)$. We found that including elongation further strengthens the conclusion that gyrotactic motility in vortical flow generates patchiness. While

elongation does not affect patch topology for some values of Ψ and Φ, it produces new spatial aggregations for others (Fig. S1 [23]) and can generate patchiness in some low stability (i.e. large Ψ) regions, where spherical cells remain randomly distributed. Changes in patchiness caused by cell elongation were quantified by calculating $N_E - N$, the difference in N relative to that obtained for spherical cells (Fig. 4(b)). Out of the ten values of Ψ and Φ tested, only one gave $N_E \lesssim N$, indicating that cell elongation generally enhances patchiness. A similar conclusion was previously found in the limit of $\Psi = \infty$: cells with larger γ are more likely to escape vortices and aggregate along separatrices [30].

The influence of buoyancy, inertia, and motility on the motion of particles within vortical flows has been studied extensively [19, 20, 22, 24, 30]. Particles that can move only vertically relative to the flow, for example as a result of buoyancy, correspond to $\Psi = 0$ and can not generate patchiness in unbounded flows (i.e. $N(t) = 0$; [20]). Particle inertia can in principle induce patchiness [20], but phytoplankton's small size and density contrast (<10% denser than seawater) preclude them from aggregating via inertia in most natural flows [31]. In contrast, we have shown that a simple vortical flow can trigger rapid accumulation of gyrotactic phytoplankton over a broad range of dimensionless parameter space, suggesting that motility might play an important role in determining the spatial distribution of these microorganisms in the environment, if this mechanism proves robust in turbulent flows. Partial support for this hypothesis comes from observations that motile species are more likely to be aggregated at small scales than non-motile species [7, 9], though alternate mechanisms including chemotaxis [32] and phototaxis [33] may also be responsible.

An additional prediction borne out of this model is that different motility characteristics may drive widely different spatial cell distributions. If verified, it would imply that the interaction of motility and flow may control the success of different species in processes like the competition for nutrients and sexual reproduction. One may further speculate that cells could actively control their spatial distribution by adjusting their position in (Φ, Ψ) space (Fig. 2) to favor or prevent aggregation, by either regulating their swimming speed (i.e. Φ) [34] or altering their stability (i.e. Ψ) via changes in morphology [35], chloroplast position [36], or flagellar stroke [29].

One must, however, be very cautious in extending findings from an idealized flow model to realistic flows. While the steady TGV flow is often used as a crude analogue for turbulence [20, 22], the latter is time-dependent, fully three-dimensional, and incorporates a range of scales, including larger-scale fluid motion that can disperse aggregations formed at smaller scales [37]. Therefore, in the same spirit as studies that examined the motion of inertial particles in TGV flow [20], the results presented here open new hypotheses that await to be tested with more realistic flow models (e.g. direct numerical simulation) or in laboratory experiments.

OCE-0744641-CAREER to RS.

References:

[1]   P. Legendre, and M. J. Fortin, Vegetatio **80**, 107 (1989).
[2]   C. B. Field *et al.*, Science **281**, 237 (1998).
[3]   T. Fenchel, Annu. Rev. Ecol. Syst. **19**, 19 (1988).
[4]   J. H. Steele, Nature **248**, 83 (1974).
[5]   H. Yamazaki *et al.*, Geophys. Res. Lett. **33** (2006).
[6]   J. G. Mitchell *et al.*, J. Mar. Syst. **69**, 247 (2008).
[7]   S. M. Gallager, H. Yamazaki, and C. S. Davis, Mar. Ecol. Prog. Ser. **267**, 27 (2004).
[8]   R. L. Waters, J. G. Mitchell, and J. Seymour, Mar. Ecol. Prog. Ser. **251**, 49 (2003).
[9]   L. T. Mouritsen, and K. Richardson, J. Plankton Res. **25**, 783 (2003).
[10]   G. Flierl *et al.*, J. Theor. Biol. **196**, 397 (1999).
[11]   A. M. Roberts, and F. M. Deacon, J. Fluid Mech. **452**, 405 (2002).
[12]   J. O. Kessler, Nature **313**, 218 (1985).
[13]   M. Lebert, and D. P. Hader, Nature **379**, 590 (1996).
[14]   T. J. Pedley, and J. O. Kessler, Annu. Rev. Fluid Mech. **24**, 313 (1992).
[15]   K. Drescher *et al.*, Phys. Rev. Lett. **102** (2009).
[16]   N. A. Hill, and D. P. Hader, J. Theor. Biol. **186**, 503 (1997).
[17]   W. M. Durham, J. O. Kessler, and R. Stocker, Science **323**, 1067 (2009).
[18]   G. B. Jeffery, Proc. R. Soc. A **102**, 161 (1922).
[19]   H. Stommel, J. Mar. Res. **8**, 24 (1949).
[20]   M. R. Maxey, and S. Corrsin, J. Atmos. Sci. **43**, 1112 (1986).
[21]   G. I. Taylor, Philos. Mag. **46**, 671 (1923).
[22]   S. R. Dungan, and H. Brenner, Phys. Rev. A. **38**, 3601 (1988).
[23]   See supplemental material at http://link.aps.org/ supplemental/10.1103/PhysRevLett.106.238102.
[24]   J. G. Mitchell, A. Okubo, and J. A. Fuhrman, Limnol. Oceanogr. **35**, 123 (1990).
[25]   M. Maar *et al.*, Limnol. Oceanogr. **48**, 1312 (2003).
[26]   D. M. Lewis, Proc. R. Soc. Lond. A **459**, 1293 (2003).
[27]   J. R. Fessler, J. D. Kulick, and J. K. Eaton, Phys. Fluids **6**, 3742 (1994).
[28]   W. R. Clavano, E. Boss, and L. Karp-Boss, Oceanogr. Mar. Biol. Annu. Rev. **45**, 1 (2007).
[29]   M. S. Jones, L. Le Baron, and T. J. Pedley, J. Fluid Mech. **281**, 137 (1994).
[30]   C. Torney, and Z. Neufeld, Phys. Rev. Lett. **99** (2007).
[31]   J. Jimenez, Scientia Marina **61**, 47 (1997).
[32]   J. R. Seymour, Marcos, and R. Stocker, Am. Nat. **173**, E15 (2009).
[33]   C. Torney, and Z. Neufeld, Phys. Rev. Lett. **101** (2008).
[34]   R. N. Bearon, D. Grünbaum, and R. A. Cattolico, Mar. Ecol. Prog. Ser. **306**, 153 (2006).
[35]   M. J. Zirbel, F. Veron, and M. I. Latz, J. Phycol. **36**, 46 (2000).
[36]   W. Haupt, Bioscience **23**, 289 (1973).
[37]   L. P. Wang, and M. R. Maxey, J. Fluid Mech. **256**, 27 (1993).
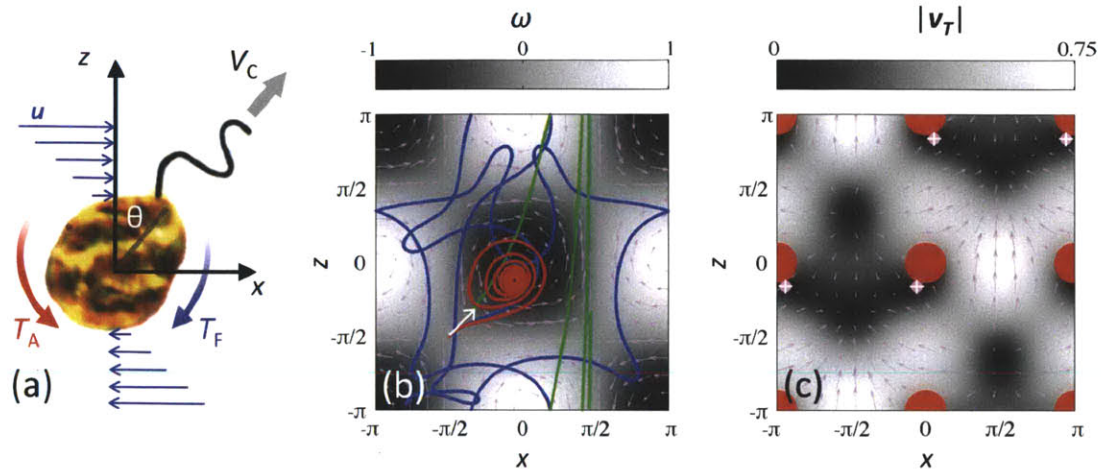
FIG. 1 (a) Gyrotactic microorganisms, such as the toxic marine phytoplankton *Heterosigma akashiwo* shown here (diameter ≈ 14 µm), swim in a direction, θ, set by a balance of torques. The torque due to the fluid (T_F) tends to rotate the cell, whereas the torque due to cell asymmetry (T_A) – for example bottom heaviness – tends to restore the cell to its preferential orientation, **k**. V_C is the swimming speed.

(b) Three cells, with different Ψ and Φ, initialized at the same location and orientation ($x = z = -\pi/2$; $\theta = \pi/4$; white arrow) in a TGV flow follow very different trajectories. Trajectories correspond to (Ψ, Φ) = (0.1, 20)(green); (1, 0.2)(red); (100, 0.5)(blue). The dimensionless TGV velocity and vorticity fields are shown by arrows and by shading, respectively. The domain is doubly periodic. The **y** axis extends into the page.

(c) The most intense cell accumulation occurs when cells converge to equilibrium points, where total cell velocity $V_T = (dx/dt, dz/dt) = (0, 0)$. Shown here is the 'equilibrium double' regime ($\Psi = 1.1$, $\Phi = 0.25$). White crosses are numerical predictions of the equilibria, pink circles are analytical results. Arrows and shading show V_T and $|V_T|$, respectively. Red circles denote regions where vorticity can overturn cells ($\omega\Psi > 1$).
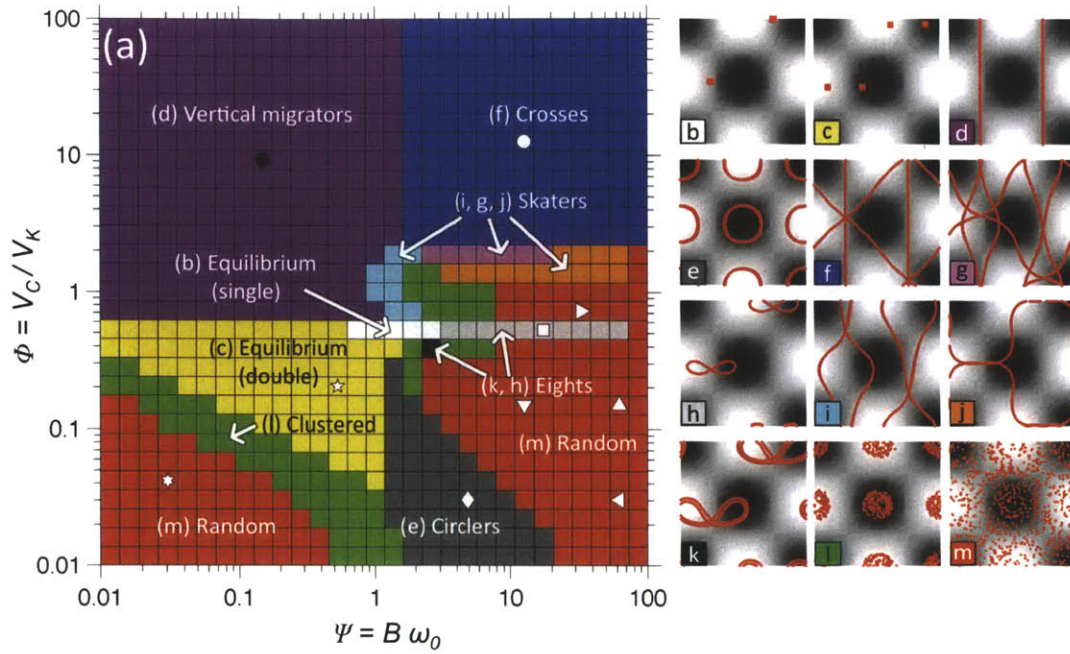
FIG. 2 (a) Parameter space of gyrotactic swimming in TGV flow, showing different patchiness regimes. Each square represents one of 900 simulations. In each simulation the trajectories of 400 randomly initialized cells were integrated until $t = 2000$. Ten distinct patterns emerge (b-k), not including the cases in which accumulation does not occur (m) or has not converged (l). For the 'equilibrium' regimes (b,c), all cells reside at the equilibrium points. The symbols in (a) correspond to (Ψ, Φ) values that are analyzed in Fig. 4(b) to investigate the role of cell elongation.
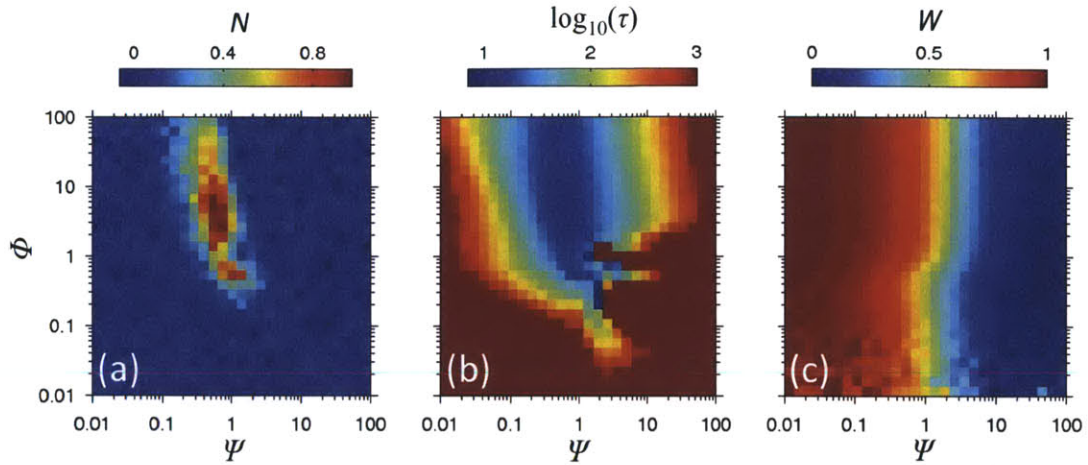
FIG. 3 (a) The degree of patchiness at time $t = 10$, quantified by the accumulation index N, for the same matrix of simulations as in Fig. 2. $N = 0$ corresponds to a random (Poisson) distribution, while $N > 0$ indicates aggregation.

(b) The time, τ, (non-dimensionalized by $1/\omega_0$) required for cells to reach a time-invariant spatial pattern.

(c) The normalized vertical migration rate, W. Vertical migration is unhindered when $W = 1$ and entirely suppressed by flow when $W = 0$.
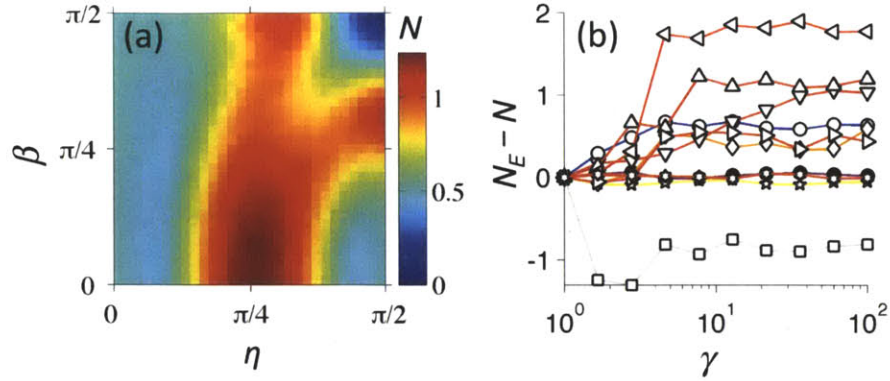
FIG. 4 (a) Gyrotactic cells swimming within a 3D TGV flow form aggregations for almost any vortex orientation. Plotted here is the accumulation index, N, at $t = 10$ and $\Phi = \Psi = 1$, as a function of the polar and azimuthal angles, η and β.

(b) Cell elongation (aspect ratio $\gamma > 1$) produces an increase in patchiness in most regimes, compared to the case of spherical cells ($\gamma = 1$). Shown is the change in the accumulation index, $N_E - N$, due to elongation, at $t = 2000$. Symbols and colors correspond to Φ, Ψ values and aggregation regime color in Fig. 2(a), respectively. Representative cell distributions for each case can be found in Fig. S1 [23].

(a) $\Psi = 0.13$, $\Phi = 7.8$	(b) $\Psi = 11$, $\Phi = 11$	(c) $\Psi = 0.45$, $\Phi = 0.17$	(d) $\Psi = 0.026$, $\Phi = 0.036$	(e) $\Psi = 15$, $\Phi = 0.45$
(f) $\Psi = 4.2$, $\Phi = 0.026$	(g) $\Psi = 11$, $\Phi = 0.13$	(h) $\Psi = 53$, $\Phi = 0.13$	(i) $\Psi = 53$, $\Phi = 0.026$	(j) $\Psi = 28$, $\Phi = 0.62$
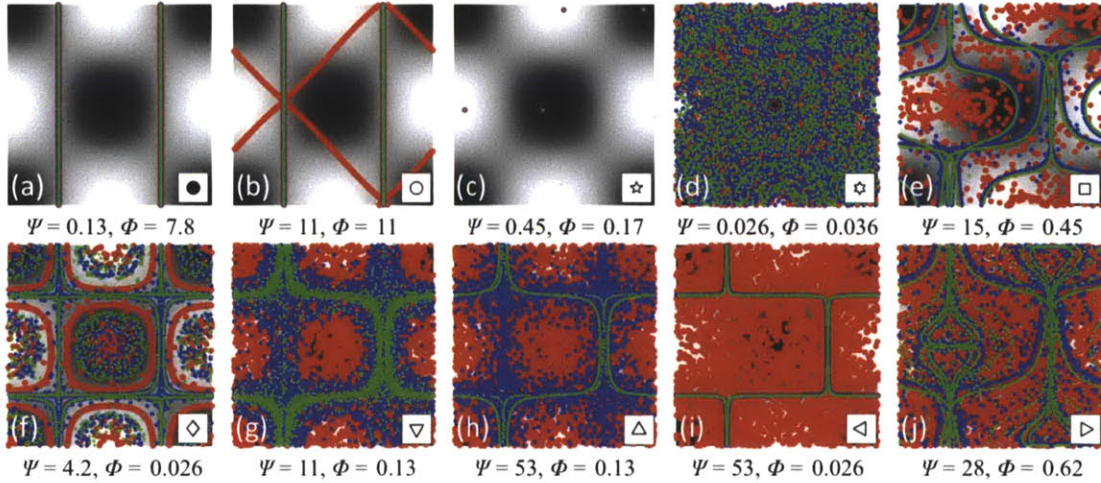
FIG. S1: The position of cells at $t = 2000$ for three different cell aspect ratios, γ. Red, blue, and green dots denote cells with $\gamma = 1$, 4.6, and 21, respectively. Symbols on the lower right correspond to those in Figs. 2(a) and 4(b) and refer to the Φ, Ψ values provided beneath each panel. Elongated cells produce patchiness whenever spherical cells do (a,b,c,e,f), and further produce patchiness in some low stability (*i.e.* high Ψ) regions where spherical cells do not (g-j). In (a) and (b), cells of all three types are distributed along the vertical lines. In (c), all cell types reside at each of the equilibrium points.

CHAPTER 3

Turbulence drives microscale aggregation of motile phytoplankton

William M. Durham[1], Michael Barry[1], Eric Climent[2], and Roman Stocker[1]

[1] Department of Civil and Environmental Engineering, Massachusetts Institute of Technology, 77 Massachusetts Avenue, Cambridge, Massachusetts 02139, USA

[2] Institut de Mécanique des Fluides, Université de Toulouse, INPT–UPS–CNRS, Allée du Pr. Camille Soula, F-31400 Toulouse, France

The distribution of marine phytoplankton exhibits multiscale heterogeneity, with gradients in concentration spanning more than nine orders of magnitude in length scale. Patchiness at sub-meter scales is often considered to result from turbulent stirring: this 'top-down' process transfers heterogeneity to successively smaller length scales. However, recent measurements at the centimeter scale have revealed that motile phytoplankton species are more heterogeneously distributed than non-motile species, suggesting that self-propulsion plays an important role in plankton's small-scale distribution. Here, we propose a new, 'bottom-up' biophysical mechanism that drives patchiness via an interaction of motility with small-scale turbulent shear. Using a cavity-driven vortical flow with dimensions commensurate with small-scale turbulent vortices in the ocean, we show that the motile phytoplankton *Heterosigma akashiwo* rapidly form highly clustered aggregations, whereas non-motile cells remain randomly distributed. Experimental observations are in remarkable agreement with a mathematical model. To explore whether this patchiness is robust in realistic turbulent flows, we implement the same model within a homogeneous, isotropic turbulent flow generated via Direct Numerical Simulations. We find that turbulence drives strong, *de novo* aggregations of motile plankton, due to cell focusing within Kolmogorov-scale downwelling regions, and we develop a simple metric to predict the level of patchiness. Because this mechanism dramatically reduces the mean distance between neighboring cells, it can markedly affect encounter rates and cell-to-cell interactions and thus have broad implications on phytoplankton ecology and marine productivity.

Organisms are rarely spaced evenly. Microbes are no exception: heterogeneous spatial distributions and the processes that shape them play a central role in their ecology and evolutionary dynamics (Levin 1992, Zhang *et al*. 2011). In the ocean, patchiness in the distribution of phytoplankton, and the hotspots in marine productivity that it sustains, have for centuries intrigued fisherman and scientists alike (Darwin 1845, Hardy 1936, Uda 1938). Gradients in the concentration of these primary producers span a wide range of length scales, ranging from regions of enhanced concentration with length scales of thousands of kilometers due to persistent upwelling at the equator (Marañón *et al*. 2001)

to ephemeral microscale patchiness at the scale of centimeters (Mitchell *et al.* 2008, Malkiel *et al.* 1999).

Phytoplankton patchiness has profound and diverse implications on the marine ecosystem, including the maintenance of diversity (Bracco *et al.* 2000), overall ecosystem productivity (Steele 1974), predator-prey dynamics (Tiselius 1992, Tiselius *et al.* 1993), and fish recruitment (Lasker 1975). The observed variance in the distribution of phytoplankton exceeds that of a random process (Mackas 1985) and multiple mechanisms have been proposed to explain this variability (Martin 2003). At the mesoscale (order ~100 kilometers), these mechanisms often invoke the coupling of phytoplankton growth with other processes such as predation, heterogeneity in carrying capacity, and flow (Martin 2003). However, growth can only produce heterogeneity at scales where patches form faster than turbulent mixing destroys them. A scaling argument yields the minimum length scale at which this can occur: the timescale for a turbulent eddy to transfer its energy to eddies half its size must be larger than the plankton's doubling time (Denman and Platt, 1976). This argument predicts a minimum length scale of a few kilometers, whereas at smaller scales phytoplankton are largely considered to behave as passive, conservative tracers. In contrast, coherent non-turbulent fluid motion can drive variability at scales <1 kilometer via biophysical interactions with motility and sedimentation, such as the aggregation of plankton within Langmuir cells (Stommel 1949), at fronts (Franks, 1992), and in thin layers of enhanced shear (Durham and Stocker 2009).

The differential survival of organisms is shaped by the interaction of individuals with their local environment. Thus, to garner a fundamental understanding of the processes that mediate the differential survival of plankton and ultimately how they regulate marine productivity, effort must be directed at resolving these processes at the level of an individual (Seymour *et al.* 2010). A vast array of ecological interactions in the plankton depend on the rate at which organisms encounter each other and their predators and prey. Patchiness can greatly increase encounter rates by reducing the median distance between neighbors. A phytoplankton cell, whose length scale ranges from 1 to 1000 μm, inhabits an environment whose spatial structure is much smaller than can be sampled using traditional techniques, such as Niskin bottles and plankton nets. Over the last 15 years, significant strides have been made to bridge this gap by directly observing the distribution of phytoplankton *in situ* at the millimeter to centimeter scale. A number of different techniques have been employed including high-resolution fluorometers (Mitchell *et al.* 2008, Yamazaki *et al.* 2006, Cowles *et al.* 1998), underwater videomicroscopy (Gallagher *et al.* 2004), three-dimensional holography (Malkiel *et al.* 1999) and pneumatically operated arrays of syringes (Maar *et al.* 2003, Owen 1989, Mouritsen and Richardson 2003, Waters and Mitchell 2002, Waters *et al.* 2003). The latter three techniques afford the ability to distinguish cell type and their use has shown that motile phytoplankton species often have a much more patchy distribution than non-motile species (Gallagher *et al.* 2004, Maar *et al.* 2003, Owen 1989, Mouritsen and Richardson 2003, Malkiel *et al.* 1999). Yet, although phytoplankton motility is acknowledged to contribute to the formation of this small-scale variability, the underlying mechanism has remained unclear.

Motility is a pervasive trait of phytoplankton, with 90% of the species that form harmful algal blooms being able to actively swim (Smayda 1997). Self-propelled vertical migration through the water column likely confers a selective advantage to motile over non-motile cells when the euphotic zone is nutrient-limited (Margalef 1978): migrating cells can reside in the well-lit surface layer during daylight hours, while accessing deeper pools of inorganic resources (Ryan et al. 2010) and avoiding their zooplankton predators at night (Bollens et al. 2011). To bias their motility in the vertical direction, many phytoplankton cells generate a stabilizing torque that orients them vertically via a process known as gravitaxis. Gravitaxis can result from active steering guided by a cells' ability to sense gravity (Lebert and Hader 1996) or can arise passively via either an asymmetry in cell density (Kessler 1985) or an asymmetry in drag due to flagellar motion (O'Malley and Bees 2011). However, fluid motion is inevitable in most phytoplankton environments, and the associated shear (spatial gradients in fluid velocity) exerts a viscous torque upon cells that tends to make them overturn. The cell's swimming direction at equilibrium is governed by the competition of shear, which has a destabilizing effect, and self-stabilization, and the cell is said to undergo gyrotaxis (Kessler 1985).

One of the primary forms of shear that phytoplankton experience results from turbulent fluid motion. In the ocean, turbulence encompasses a wide range of scales: the largest, 'integral' scale fluctuations transmit their energy, without dissipation, to successively smaller eddies, down to a scale – the Kolmogorov scale – where the fluid viscosity suppresses the cascade. Kolmogorov vortices have a characteristic length $\eta_K \sim (v^3/\varepsilon)^{1/4}$ ($\sim$ mm–cm in the ocean) and a shear rate $\omega_K \sim (\varepsilon/v)^{1/2}$ ($\sim 0.01 - 10$ s^{-1}), where v is the kinematic viscosity of seawater and ε the rate at which turbulent energy is dissipated. Phytoplankton experience turbulent shear as a time-varying, linear velocity gradient (of magnitude ω_K), because they are nearly always much smaller than η_K (Lazier and Mann 1989). A Kolmogorov vortex persists for a timescale of ω_K^{-1}, the time required for the vortex to overturn. In isotropic turbulence, the separation between the integral scale and the Kolmogorov scale (the length of the 'inertial subrange' of the flow) increases with the Taylor-Reynolds number, Re$_\lambda = u'\lambda/v$, where $\lambda = (15vu'^2/\varepsilon)^{1/2}$ is the Taylor length scale and u' the root-mean-square fluid velocity (Tennekes and Lumley 1972).

The dynamics of particle motion in turbulent flows has a rich history, owing to its importance in a broad range of environmental and industrial processes. Kolmogorov-scale fluid motion is well known to aggregate dense particles by centrifuging them out of regions of high vorticity, counteracting the mixing performed by integral scales that tends to homogenize particle concentrations (Wang and Maxey, 1993). However, the density of phytoplankton exceeds that of the water in which they live by only a few percent (Eppley et al. 1967, Van Ierland and Peperzak 1984, Kamykowski et al. 1992), hence their drift across streamlines due to centrifugal effects is marginal during the lifetime of a Kolmogorov vortex, rendering this mechanism ineffective at sustaining plankton aggregations in the face of turbulent mixing (Jimenez 1997). On the other hand, mathematical models of gyrotactic swimming within steady vortical flows have revealed that motility may drive a multitude of cell aggregation patterns (Mitchell et al. 1990, Bearon et al. 2011, Durham et al. 2011), some of them within only a few vortex overturning timescales (Durham et al 2011). It remains unknown, though, if these simple

models accurately capture phytoplankton behavior in real turbulent flows. Though simple vortical flows are often used as first proxies of turbulence (*e.g.* Maxey and Corrsin 1986), they do not account for the unsteadiness, mixing, and multiple scales of fluid motion found in turbulence. Here we experimentally demonstrate that a vortical flow with dimensions commensurate with the Kolmogorov scale of marine turbulence can drive dramatic aggregations of motile phytoplankton and then, using a numerical model, we show this mechanism is robust in realistic turbulent flows.

In an effort to experimentally generate a flow similar to the Taylor-Green vortex array (Taylor 1923), which has been used in previous modeling studies of gyrotaxis (Bearon *et al.* 2011, Durham *et al.* 2011), we developed a device that produces two counter-rotating vortices via a cavity flow (Figure 1). A syringe pump is used to drive equal flows of a culture of the ichthyotoxic raphidophyte *Heterosigma akashiwo* along each side of the device, producing symmetric vortical flows in the central test section (Figure 1a, blue dotted line). A laser sheet was used to illuminate cells along the centerline of the device, where flow is two-dimensional due to symmetry. An initially random distribution of cells was generated by clamping one of the supply tubes that feeds the side channels, inducing a unidirectional flow through the central test section. Once the tube was unclamped, vortical flow was restored and the experiment began. The position of cells swimming within vortices was obtained using custom software to quantitatively measure the distribution of cells within the device. We could only image <100 cells within a single image, because of our narrow light sheet (1.6 mm in thickness) and the occurrence of bioconvective instabilities beyond a threshold cell concentration (Pedley and Kessler 1992). Therefore, to achieve robust statistics, cell positions from a $\approx$ 4-minute period of the experiment were compiled to produce a single histogram of cell distribution (see Methods and Materials section).

Experiments using motile cells produced strong aggregations (Figure 2a), whereas cells from the same phytoplankton culture, killed with a small amount of ethanol, remained randomly distributed (Figure 2b). Aggregations in the former case occurred in two distinct locations: at the center of the vortices and within the downwelling region between the vortices. The convergence of gyrotactic phytoplankton in regions of downwelling flow has been repeatedly observed and predicted (Kessler 1985, Pedley and Kessler 1992) and stems from vorticity orienting the cells towards the center of downwelling regions. In our experiments, the upward swimming velocity of the cells exceeds the downward fluid velocity in the relatively quiescent downwelling portion of the test section, and thus cells in the downwelling region can reach the upper boundary of the device and collect there. In contrast, the cell aggregations at the center of the vortices arise from the superposition of recirculating vortical flow and gyrotactic motility: similar aggregations were found using individual-based models of gyrotaxis in a steady, Taylor-Green vortex flow (Durham *et al.* 2011).

To verify that the observed cell aggregations resulted from the interaction between motility and flow, we quantified the divergence field associated with the cell velocities. The two-dimensional flow field at the central plane, $\mathbf{u} = (u, w)$, is divergence-free ($\partial u/\partial x + \partial w/\partial z = 0$) because of incompressibility. In contrast, the velocity field of the phytoplankton cells, which results from the superposition of motility and flow, is not

expected to be divergence-free: regions of negative divergence denote the locations where aggregation occurs.

In the experiments, we captured the trajectories of individual cells by particle tracking velocimetry. By calculating the median cell velocity within discrete two-dimensional bins, we converted the Lagrangian cell trajectories into a Eulerian velocity field (Figure 1B), which we used to calculate the divergence (see Methods and Materials section). The divergence field of motile cells (Figure 3A) exhibits two ring-shaped regions of negative divergence, in which cells converge to form aggregations. In comparison, in the divergence field of non-motile cells no clear pattern emerges from noise (Figure 3C).

To support the conclusion that the observed accumulation resulted from the interaction of motility and vertical flow, we coupled an individual-based model of gyrotactic swimming within a model of the flow field within our experimental device. The flow field was generated with COMSOL Multiphysics using the same geometry and boundary conditions as our experimental device. Gyrotactic motility was modeled by integrating the equation for the evolution of the swimming direction of a bottom-heavy spherical cell (Pedley and Kessler 1992),

$$\frac{d\mathbf{p}}{dt} = \frac{1}{2B}\left[\mathbf{k}-(\mathbf{k}\cdot\mathbf{p})\mathbf{p}\right]+\frac{1}{2}\boldsymbol{\omega}\times\mathbf{p}\,, \tag{1}$$

where $\mathbf{p}$ is the unit vector along the swimming direction, $\boldsymbol{\omega}=\nabla\times\mathbf{u}$ is the fluid vorticity, $\mathbf{u}$ = $[u\ v\ w]$ is the three-dimensional fluid velocity, t is time, $\mathbf{k}$ is the unit vector in the vertical direction, positive upwards, and B is the gyrotactic reorientation timescale, the characteristic time a perturbed cell takes to return to vertical if $\boldsymbol{\omega}=0$. The first term on the right hand side describes the tendency of a cell to remain aligned along the vertical direction due to bottom-heaviness, while the second term captures the tendency of shear to overturn a cell by imposing a viscous torque on it. We neglect the effect of cells on the flow and cell elongation. In the simulations, cell positions and orientations were initialized at random locations within the device and uniformly over a unit sphere, respectively. The cell position, $\mathbf{X}=(x,y,z)$, was computed by integrating the velocity resulting from the superposition of swimming with speed V_C on the flow $\mathbf{u}$, as

$$\frac{d\mathbf{X}}{dt} = V_C\mathbf{p}+\mathbf{u}(\mathbf{X})\,. \tag{2}$$

The swimming velocity of each cell, V_C, was drawn from a distribution measured within the experimental device and had a mean of 75 μm s^{-1} (Figure S1). The gyrotactic reorientation parameter was assumed to be the same for all cells, $B = 2$ s, based on a previous estimate for this species (Durham et al. 2009).

From the simulated phytoplankton trajectories, we calculated the spatial distribution of cells and the divergence of the cell velocity field, limited to the center-plane of the flow region, as in the experiments. The cell distribution (Figure 2B) bears strong resemblance to the observations (Figure 2A), with similar aggregations in the downwelling region and in the center of vortices. The additional spatial structure in the simulations (notice the two concentric ring-shaped accumulations about the vortices) likely results from neglecting

42

the random component of cell motility, which tends to smooth the distribution of cells. The simulated divergence field (Figure 3C) exhibits circular regions of negative divergence similar to those observed in the experiments, suggesting that the same process of underlies the aggregations in the two cases. Taken together, the strong correlations between simulations and experiments indicate that the mathematical parameterization of gyrotactic motility can capture the generation of phytoplankton patches in vortical flow fields and support its application in a turbulent flow field, often modeled as a collection of vortices of different sizes (Lewis 2003).

While models of the motion of suspended particles and bubbles in turbulent flows were once limited to simple vortical flows and kinematic representations of disordered fluid motion (*e.g.* Maxey and Corrsin 1986, Lewis 2003), in the past two to three decades increasing computational power has led to the proliferation of realistic models of homogenous, isotropic turbulence. In these models, energy is imparted on the fluid using random body forces, applied spectrally at low wavenumbers, and the ensuing cascade of smaller scale fluctuations is resolved by solving the full Navier-Stokes equations down to the Kolmogorov scale. Because a 'closure' scheme is not needed in this approach, it is known as a Direct Numerical Simulation (DNS) and yields the most accurate representation of a turbulent flow. This technique has been widely successful in the prediction of particle dynamics in a number of different processes, including the coalescence of water droplets in clouds and the transport of suspended particles in open channel flows (Shaw 2003, Rouson and Eaton 2001). In contrast, despite the ubiquitous presence of turbulence in plankton's natural environments, studies of particles within DNS flows with sizes and density contrasts typical of planktonic microorganisms has been very limited. A previous DNS study (Squires and Yamazaki 1995a) reported that particles with a density contrast comparable with that of phytoplankton aggregated via particle inertia within a turbulent flow, but these findings were later found to be in error (Squires and Yamazaki 1995b, Jimenez 1997).

To determine whether gyrotaxis can generate cell patchiness in turbulent flows, we generated an isotropic, homogenous flow within a computational box with triply periodic boundary conditions. After the flow had reached statistical steady state, we initialized 10^5– 3.2×10^6 gyrotactic swimmers with random orientations and positions in the domain. The evolution of each cell's position was calculated with the same model as above. To generalize results, we nondimensionalized the phytoplankton traits B and V_C by the Kolmogorov shear rate, ω_K, and velocity, V_K, obtaining two dimensionless parameters that control the cells' fate. The first one, $\Phi = V_C\, V_K^{-1}$, measures the swimming speed of the cells relative to the characteristic velocity of the smallest eddies. The second one, $\Psi = B\omega$, controls how unstable the cells are to overturning by velocity gradients. To understand the role of Ψ, it is instructive to consider the steady case, where ω_K is replaced by a coherent steady horizontal vorticity (Durham et al. 2009). In this case, Ψ controls how effective the cells' vertical migration is. Assuming a constant shear rate, when $\Psi < 1$ cells swim at an angle θ to the vertical, with $\sin\theta = \Psi$. When $\Psi > 1$, cells tumble end over end at an angular velocity $d\theta/dt = (\Psi - \sin\theta)/2$, completely losing their ability to migrate vertically (Figure 8A).

To quantify patchiness, we used two metrics: N, the normalized standard deviation of the box probability function (Fessler *et al* 1994, Durham *et al* 2011); and Q, the normalized concentration of the most aggregated 10% of cells. N was computed by dividing the numerical domain into equal boxes and counting the number of cells, n, in each box, to obtain the box probability function, $f(n)$. As cells accumulate in some boxes and leave others empty, the standard deviation of $f(n)$, σ, increases relative to its initial (Poisson) value, $\sigma_P = b^{1/2}$, where b is the mean of $f(n)$. Thus, the index $N = (\sigma - \sigma_P)/b$ is a measure of patchiness. Q was obtained by determining the three-dimensional Voronoi tessellation of the cell distribution using the C++ routine Voro++ (Rycroft *et al.* 2006), which accounts for the periodic boundary conditions to find the polyhedron associated with each cell. The inverse of the polyhedron's volume is a measure of the local cell concentration: the volume of the polyhedron associated with a cell in a patch is much smaller than that of a cell in a region of low cell density. We defined the 10% of the cells with the largest local concentrations as belonging to patches and computed the normalized patch concentration as $Q = (C - C_P)/C_M$, where C is the median cell concentration within all patches, C_P is its counterpart if cells are Poisson-distributed, and C_M is the mean cell concentration of all particles (the number of particles divided by the size of the entire numerical domain). Thus, Q represents the increase in the cell concentration within patches relative to the Poisson case.

First, to probe how the cell distribution is affected by the dimensionless parameters Ψ and Φ, we ran 27 simulations with different $[\Psi, \Phi]$ values. Each simulation tracked 10^5 cells with identical motility parameters and the same flow field ($Re_\lambda = 60$). We calculated N over time, as each simulation ran, to determine when the cell distribution had reached steady state. This occurred typically after ~20 Kolmogorov timescales. Thereafter, we exported snapshots of particle locations to calculate Q. The simulations revealed (Figure 4) that while the majority of non-motile cells ($\Phi = 0$) remain relatively disperse, motility ($\Phi > 0$) allowed some cells to achieve highly aggregated states. Quantitatively, motile cells achieved patch concentrations up to 30 times more intense than their non-motile counterparts, as measured by the Q metric (Figure 5). Concentrations within patches were found to increase with the relative swimming speed, Φ, and to peak at an intermediate stability value, $\Psi \approx 1$, both of which are in agreement with results for gyrotactic motility in a two-dimensional, steady vortical flow (Durham *et al.* 2010). This finding is readily rationalized: to accumulate, cells must swim across streamlines. Fast swimmers make significant progress across streamlines, while intermediate stability represents a trade-off between persistent tumbling ($\Psi \gg 1$), which negates directed swimming, and excessive stability ($\Psi \ll 1$), which prevents cell orientation from being perturbed by the flow.

We expected that an increase in Re_λ would decrease the patchiness intensity, due to an increase in the size of the largest scales of fluid motion, which dominate dispersion. To test if aggregations are sensitive to Re_λ and ensure that our choice of using Kolmogorov scales in the dimensionless formulation is robust, we performed selected simulations at four different Taylor Reynolds numbers ($Re_\lambda = 38, 60, 94, 123$). We find that patchiness is not significantly affected by the Taylor Reynolds number (Figure 6): an increase in Re_λ from 38 to 123 reduces the intensity of patchiness by less than a factor of two.

44

Furthermore, in all simulations the maximum level of patchiness occurred for $\Psi{\sim}1$, confirming that cell aggregation is controlled at the Kolmogorov scale (Figure 6).

Simulations of gyrotactic motility in a two-dimensional, steady vortical flow had earlier revealed a diverse array of aggregation regimes, each of which attracts cells to a different region of the flow, depending on the values of Ψ and Φ, (Durham *et al.* 2011). To determine whether the accumulations in turbulent flow can be rationalized in terms of any of these regimes, we calculated the mean fluid properties at the locations of the cells classified as belonging to patches. We find that, as the concentration within patches increases, aggregated cells have a greater tendency to reside within regions of downwelling flow (Figure 7A). Furthermore, more concentrated patches have a slight tendency to reside in regions where the magnitude of the z-vorticity, ω_z, is large (Figure 7B). This observation is likely explained in terms of vortex stretching: extensional flows tend to amplify vorticity (Jumars *et al.* 2009), and in turbulent flows the principal axes of strain are correlated with the direction of most intense vorticity (Jimenez 1992). Thus, because enhanced vertical velocities drive regions of locally elevated vertical vorticity by 'stretching' vertically oriented vortices, the patches in our simulation are correlated with regions of large vertical vorticity. Overall, these findings suggest that, while there exist many potential regimes of aggregation (Durham *et al.* 2011), accumulation in downwelling regions is the dominant means of aggregation in turbulent flows.

The finding that aggregations within a turbulent flow occur in downwelling regions allowed us to develop a simple model to predict the intensity of the aggregation based on the relative stability, Ψ, and the relative swimming speed, Φ, of the cells. We consider a downwelling region with a typical vorticity ω_K, for simplicity taken to be constant over the downwelling region and resulting from one component of the velocity gradient only, $\partial w/\partial x$ (Figure 8A). Neglecting advection by the flow, the speed at which cells enter the region of downwelling corresponds to the mean horizontal drift velocity due to swimming (Figure 8B), which depends on the swimming direction. Cells with $\Psi<1$ swim straight at a constant angle, $\theta = \sin^{-1}(\Psi)$, to the vertical, whereas cells with $\Psi>1$ tumble end over end into regions of downwelling (Figure 8A). To estimate a cell's mean horizontal orientation $<p_x>$ for $\Psi>1$, one can integrate the rotation rate of the cell, $d\theta/dt = (\Psi -\sin\theta)/2$, to find its horizontal projection, $\sin\theta$, over the period of a tumble, $T = 2\pi/(\Psi^2-1)^{1/2}$ to obtain $<p_x> = \Psi - (\Psi^2-1)^{1/2}$. (Ghorai and Hill 1999). Both $<p_x>$ is plotted in Figure 8b as a function of Ψ. The cell swimming speed, V_{in}, towards regions of enhanced downwelling is given by the product of the horizontal projection of the swimming direction with the swimming speed, $V_{in} = \Phi<p_x>$. We plotted the V_{in} of our 27 simulations performed at different $[\Psi,\Phi]$ values as a function of the patch intensity Q (Figure 9). Surprisingly, in light of the simple assumptions of this model, V_{in} was found to be an excellent predictor of patch concentration. Furthermore, a least-squares regression suggests a power-law relationship with $Q \sim V_{in}^{1.87}$ for $\Psi \geq 1$ and $Q \sim V_{in}^{1.06}$ for $\Psi < 1$. This relationship likely results from the competition between aggregation within downwelling and turbulent dispersion.

A scaling analysis may offer some insight on how this power-law dependence arises. Assuming aggregation occurs in the x,y plane with a dimensionality d ($d = 1$ if cell

motility converges to a horizontal line; $d = 2$ if cells swim radially inwards to a point), conservation of the number of cells dictates that the cell concentration, c, will be inversely proportional to the characteristic patch size, r, and can be expressed as $c \sim (1/r)^d$. Assuming that mixing induced by the flow can be modeled with an effective turbulent dispersion coefficient, κ, one infers that the patch size r is set by the balance of inwards motility and turbulent dispersion, $r \sim \kappa/V_{in}$. This predicts that the patch concentration displays a power-law dependence, $c \sim (V_{in}/\kappa)^d$, which matches our observations if $d \approx 2$ for $\Psi \geq 1$ and $d \approx 1$ for $\Psi < 1$. These predictions of the dimensionality of the aggregations are consistent with the morphology of the simulated patches: for $\Psi \geq 1$ patches form long filamentous structures, while for simulations with $\Psi < 1$ patches have a more elongated horizontal structure (Figure 4).

Our results predict that aggregation will be most significant when Ψ is order unity and Φ is larger than 1. Turbulence in the ocean can have a broad range of intensities: rates of turbulent dissipation range from $\varepsilon = 10^{-10} \, m^2 \, s^{-3}$ in the deep ocean to $\varepsilon = 10^{-4} \, m^2 \, s^{-3}$ in the upper mixed layer (Gallagher *et al.* 2004, Marr *et al.* 2003, Jumars *et al.* 2009). This leads to Kolmogorov vortices with size $\eta_K \sim (v^3/\varepsilon)^{1/4} = 0.3 - 10$ mm, vorticity $\omega_K \sim (\varepsilon/v)^{1/2} = 0.01 - 10 \, s^{-1}$ and velocity $V_K \sim \eta_K \omega_K \sim (v\varepsilon)^{1/4} = 0.1 - 3$ mm s^{-1}. While the gyrotactic reorientation parameter B has only been quantified for a few model species (Kessler 1985, Hill and Hader 1997, Drescher *et al.* 2009, Durham *et al.* 2009, Maar *et al.* 2003), we surmise that for most phytoplankton it lies between 1 and 10 s. Phytoplankton motility is extremely rapid, as cells swim at tens or even hundreds of body lengths per section: swimming velocities of up to $V_C = 1500 \, \mu m \, s^{-1}$ have been observed (Kamykowski et al. 1992, Horstmann 1980). Thus, Ψ is expected to vary between 10^{-2} and 10^2 and Φ between 0 and 15, revealing that the entire $[\Psi,\Phi]$ parameter space analyzed here (Figure 5) is physically realistic. Our results, then, predict that patchiness will most readily occur at the intermediate turbulence intensities ($\varepsilon \sim 10^{-7}$ to $10^{-6} \, m^2 \, s^{-3}$), where $\Psi \sim 1$. Furthermore, typical values of the Taylor Reynolds number range from $Re_\lambda \approx 20$ in the pycnocline, to $Re_\lambda \approx 150$ in the deep chlorophyll maximum, to $Re_\lambda \approx 300$ in the upper mixed layer (Tennekes and Lumley 1972, Marr *et al.* 2003). Thus, the fluid flows used here ($Re_\lambda = 38 - 123$) approximate the integral of scales of fluid motion phytoplankton typically encounter, with the exception of the upper mixed layer, where Taylor Reynolds numbers are approximately double the largest used here.

Historically, most studies have neglected the role of motility in the formation of patchy phytoplankton distributions, assuming that at scales <1 km patches result from turbulent mixing (Yamazaki *et al.* 2006). Since the magnitude of phytoplankton swimming velocities is typically much smaller than the root-mean-square turbulent velocity, a prevalent view is that motility is ineffective at controlling the small-scale spatial distribution (Gallagher *et al.* 2004). Our results suggest that, at least at the smallest scales of turbulent fluid motion, phytoplankton cannot be considered to be passive tracers of the fluid motion. Instead, motility can be a highly effective driver of phytoplankton aggregation. This conclusion is supported by field observations that demonstrate that motile organisms are much more aggregated than their non-motile counterparts (Gallagher *et al.* 2004, Maar *et al.* 2003, Owen 1989, Mouritsen and Richardson 2003, Malkiel *et al.* 1999).

46

While it is well known that turbulent fluid motion can profoundly affect the relative fitness of phytoplankton species (Margalef 1978), much remains unknown about the mechanisms by which this occurs or, in other words, how turbulence affects phytoplankton ecology at the level of an individual cell. To date, most studies have focused on the effects of turbulence on phytoplankton by measuring population dynamics within large (relative to an individual) batch reactors. Results have been varied: for example, while turbulence can stymie the growth of some species, it promotes that of others (Gibson and Thomas 1995, Peters *et al.* 2006), and in either case the underlying mechanism often remains largely unclear. In addition, it is known that small-scale turbulent motion can dramatically increase the encounter rates among planktonic organisms, with potentially dramatic effects on a spectrum of processes, from predator-prey contact (Rothschild and Osborn, 1988) to diatom coagulation (Kiorboe *et al.* 1990). Furthermore, small-scale turbulence can impact nutrient acquisition (Karp-Boss *et al.* 1996) and parasite infectivity (Llaveria *et al.* 2010). For other aspects, the impact of turbulence remains controversial. For example, experimental observations suggest that turbulent fluid motion can enhance the sedimentation rate of non-motile phytoplankton experimentally (Ruiz *et al.* 2004), yet models of this process have proven inconclusive (Marcholli *et al.* 2007).

The frequency at which most ecological interactions in the plankton occur is wholly dependent on the rates of encounter between the constituents at play. Since encounter rates within a population scale with the square of the cell concentration (Kiorboe 2008), our results – demonstrating a 30 fold increase in concentration within phytoplankton patches – may have dramatic implications on the rates of encounter of motile phytoplankton with members of their own species and, furthermore, with cells of other species, predators, and parasites.

Because our mechanism results from active motility, as opposed to passive mixing, it entails some level of control by the cells. Such evolutionary pressures might be partly responsible for (i) the incredible diversity in phytoplankton morphology (Taylor *et al.* 2008), which dictates a cell's stability against overturning, *i.e.* its B parameter (O'Malley and Bees 2011), and (ii) the wide variation in swimming velocities, V_C, encountered across different phytoplankton species (Kamykowski *et al.* 1992).

It remains to be seen whether the aggregations triggered by this mechanism positively impact phytoplankton fitness, or, alternatively, if aggregations are an unavoidable byproduct of vertical migration. On the one hand, patchiness can be detrimental for a range of ecological interactions. For example, under conditions of strong nutrient competition, patchy distributions are less desirable. For example, in eutrophic environments – where large phytoplankton occur at high concentrations – cells are under significant competition for nutrient resources (Siegel 1998). Patchiness may further increase the severity of this competition, especially among cells from the same species that tend to end up within the same patches, due to their similar motility parameters. Patchiness is also less desirable under strong predation risk. Laboratory experiments have revealed that zooplankton possess finely tuned foraging strategies that allow them to retain their position within centimeter-scale patches of their phytoplankton prey (Tiselius

1992), resulting in significantly increased rates of mortality for a patchily distributed phytoplankton population (Tiselius *et al.* 1993).

On the other hand, patchiness might positively impact phytoplankton fitness, for instance by enhancing the effectiveness of allelopathic 'chemical warfare' and by improving rates of sexual reproduction. Many species of phytoplankton excrete chemical compounds that can stifle the growth of competitors, a process known as 'allelopathy.' While the envelope of allelopathic chemicals around individual cells appears unlikely to reach sufficient concentrations to adversely affect other species (Jonnson *et al.* 2009), aggregation of organisms of a given species into denser patches may lead to higher concentrations of the chemical defense compounds. Furthermore, while phytoplankton growth normally occurs asexually, in coastal areas the life cycle of many phytoplankton includes a resting cyst phase that is preceded by sexual reproduction (Kremp and Heiskanen 1999). For sexual reproduction to be successful, two cells of the same species must contact one another such that they can fuse together: the mechanism described here facilitates such interactions by reducing the mean distance between cells of the same species.

Lastly, an intriguing hypothesis that emerges from this work is that motility might be an adaptive trait that phytoplankton can use to regulate their small-scale spatial distribution. Might cells be able to dynamically adjust their position in [Φ, Ψ] space (Figure 5), for example to trigger uniform distributions when predation risks are low or nutrients scarce, or conversely favor patchy distributions during periods of sexual reproduction? The ingredients that might make this possible have been observed: phytoplankton are capable of regulating their swimming speed (Bearon *et al.* 2006), and thus can change Φ, and they could alter their relative stability Ψ by shifting the position of chloroplasts within the cell (Swift and Taylor 2007), changing the flagellar stroke (O'Malley and Bees 2011), or altering their shape in response to changing turbulent conditions. For example, the dinoflagellate *Ceratocorys horrida* undergoes reversible changes in cell morphology in response to changes in the turbulence dissipation rate (Zirbel *et al.* 2000). If proven, the ability of phytoplankton to actively control their microscale spatial distribution would have profound implications on phytoplankton ecology and would give microbial motility a whole new level of ecological significance in the ocean.

References:

Abraham ER. (1998) The generation of patchiness by turbulent stirring. *Nature*. 391:577-580.

Bearon RN, Grunbaum D, Cattolico RA (2006) Effects of salinity structure on swimming behavior and harmful algal bloom formation in *Heterosigma akashiwo*, a toxic raphidophyte. *Mar. Ecol. Prog. Ser.* 306:153-163.

Bearon RN, Hazel AL, Thorn GJ. (2011) The spatial distribution of micro-organisms in laminar flow fields. *J. Fluid Mech.* 680:602-635.

Bollens SM, Rollwagen-Bollens G, Quenette JA, Bochdansky AB. (2011) Cascading migrations and implications for vertical fluxes in pelagic ecosystems. *J. Plankton Res.* 33:349-255.

Bracco A, Provenzale A, Scheuring I. (2000) Mesoscale Vortices and the Paradox of the Plankton. *Proc. Roy. Soc. B.* 267: 1795-1800.

Cowles TJ, Desiderio RA, Carr ME. (1998) Small-scale planktonic structure: persistence and trophic consequences. *Oceanography* 11:4-9.

Darwin CR (1845) The voyage of the Beagle. 2nd Edition, Everyman Library. Dent: London.

Denman KL, Platt T. *(1976)* The *variance spectrum of phytoplankton in a turbulent ocean. J. Mar. Res.* 34: 593–601.

Drescher K, Leptos KC, Tuval I, Ishikawa T, Pedley TJ, Goldstein RE. (2009) Dancing *Volvox*: hydrodynamic bound states of swimming algae. *Phys. Rev. Lett.* 102:168101.

Durham WM, Climent E, Stocker R. (2011) Gyrotaxis in a steady vortical flow. *Phys. Rev. Lett.* 106:238102.

Durham WM, Kessler JO, Stocker R. (2009) Disruption of vertical motility by shear triggers formation of thin phytoplankton layers. *Science* 323:1067--70

Eppley RW, Holmes RW, Strickland JDH. (1967) Sinking rates of marine phytoplankton measured with a fluorometer. *J. Exp. Mar. Biol. Ecol.* 1:191-208.

Fessler JR, Kulick JD, Eaton JK. (1994) Preferential concentration of heavy particles in a turbulent channel flow. *Phys. Fluids* 6: 3742-3749.

Franks PJS. (1992) Sink or swim: accumulation of biomass at fronts. *Mar. Ecol. Prog. Ser.* 82: 1-12.

Gallager SM, Yamazaki H, Davis CS (2004) Contribution of fine-scale vertical structure and swimming behavior to formation of plankton layers on Georges Bank. *Mar. Ecol. Prog. Ser.* 276: 27–43.

Ghorai S, Hill NA. (1999) Development and stability of gyrotactic plumes in bioconvection. *J. Fluid Mech.* 400:1-31.

Gibson CH, Thomas WH. (1995) Effects of turbulence intermittency on growth inhibition of a red tide dinoflagellate, *Gonyaulax polyedra* Stein. *J. Geophys. Res.* 100:24841-24846.

Hardy AC. (1936). Observations on the uneven distribution of oceanic plankton. *Discovery Reports*, 11:511-538.

Hill NA, Häder DP. (1997) A biased random walk model for the trajectories of swimming micro-organisms. *J. Theor. Biol.* 186:503-26.

Horstmann U. (1980) Observations on the peculiar diurnal migration of a red tide Dinophyceae in tropical shallow waters. *J. Phycol.* 16: 481-485.

Eswaran V and Pope SB. (1988) Direct numerical simulations of the turbulent mixing of a passive scalar. *Phys. Fluids* 31: 506-520.

Jimenez J. (1992) Kinematic alignment effects in turbulent flows. *Phys. Fluids A.* 4:652-654.

Jimenez J. (1997) Oceanic turbulence at millimeter scales. *Sci. Mar.* 61:47-56.

Jonsson PR, Pavia H, Toth GB. (2009) Formation of harmful algal blooms cannot be explained by allelopathic interactions. *Proc. Nat. Acad. Sci. USA.* 106:11177-11182.

Jumars PA, Trowbridge JH, Boss E, Karp-Boss L. (2009) Turbulence-plankton interactions: a new cartoon. *Mar. Ecol.* 30:133-150.

Karp-Boss L, Boss E, Jumars P. (1996) Nutrient fluxes to planktonic osmotrophs in the presence of fluid motion. *Oceanogr. Mar. Biol. Annu. Rev.* 34:71–107.

Kiorboe T, Andersen KP, Dam HG. (1990) Coagulation efficiency and aggregation formation in marine phytoplankton. *Mar. Biol.* 107:235-245.

Kiørboe T. (2008). A mechanistic approach to plankton ecology. Princeton University Press, Princeton, NJ.

Kremp A. Heiskanen A.-S. (1999) Sexuality and cyst formation of the spring-bloom dinoflagellate *Scrippsiella hangoei* in the coastal northern Baltic Sea. *Mar. Biol.* 134:771-777.

Lasker R. (1975) Field criteria for survival of anchovy larvae: relation between inshore chlorophyll maximum layers and successful first feeding. *Fish. Bull.* 73: 453-462.

Lazier JRN, Mann KH. (1989) Turbulence and the diffusive layers around small organisms. *Deep-Sea Res.* 36:1721-1733.

Lebert M, Häder D-P. (1996) How *Euglena* tells up from down. *Nature.* 379:590.

Levin SA and Segal LA. (1976) Hypothesis for origin of planktonic patchiness. *Nature.* 259: 659.

Levin SA. (1992) The problem of pattern and scale in ecology. *Ecology.* 73:1943-1967.

Lewis DM (2003) The orientation of gyrotactic spheroidal micro-organisms in a homogeneous isotropic turbulent flow. *Proc. R. Soc. Lond. A.* 459:1293-1323.

Llaveria G, Garces E, Ross ON, Figueroa RI, Sampedro N, Berdalet E. (2010) Small-scale turbulence can reduce parasite infectivity to dinoflagellates, *Mar. Ecol. Prog. Ser.* 412:45–56.

Mackas DL, Denman KL, Abbot MR. (1985) Plankton patchiness: biology in the physical vernacular. *Bull. Mar. Sci.* 37: 652-674.

Maar, M, Nielsen TG, Stips A, and Visser, AW. (2003) Microscale distribution of zooplankton in relation to turbulent diffusion. *Limnol. Oceanogr.* 48: 1312-1325.

Martin AP. (2003) Phytoplankton patchiness: the role of lateral stirring and mixing. *Prog. Oceano.* 57: 125-174.

Malkiel E, Alquaddoomi O, Katz J. (1999) Measurements of plankton distribution in the ocean using submersible holography *Meas. Sci. Technol.* 10: 1142–1152.

Marañón E, Holligan PM, Barciela R, González N, Mouriño V, Pazó MJ, Varela M. (2001) Patterns of phytoplankton size structure and productivity in contrasting open-ocean environments. *Mar. Ecol. Prog. Ser.* 216: 43-56.

50

Marcholli C, Fantoni M, Soldati A. (2007) Influence of added mass on anomalous high rise velocity of light particles in cellular flow field: A note on the paper by Maxey (1987). Phys. Fluids. 19:098101.

Margalef R. (1978) Life-forms of phytoplankton as survival alternatives in an unstable environment. *Oceanologica acta.* 1:493-509.

Malkiel E, Alquaddoomi O, Katz J. (1999) Measurements of plankton distribution in the ocean using submersible holography *Meas. Sci. Technol.* 10: 1142–1152.

Maxey MR, Corrsin S. (1986) Graviational settling of aerosol particles in randomly oriented cellular flow fields. *J. Atmos. Sci.* 43:1112-1134.

Mitchell JG, Okubo A, Fuhrman JA. (1990) Gyrotaxis as a new mechanism for generating spatial heterogeneity and migration in microplankton. *Limnol. Oceanogr.* 35:123-130.

Mitchell JG, Yamazaki H, Seuront L, Wolk F, Li H. (2008) Phytoplankton patch patterns: seascape anatomy in a turbulent ocean. *J. Mar. Syst.* 69:247-53.

Mouritsen L, Richardson K. (2003) Vertical microscale patchiness in nano- and microplankton distribution in a stratified estuary. J. Plankton Res. 25:783-797.

O'Malley S, Bees MA. (2011) The orientation of swimming biflagellates in shear flows. *Bull. Math. Biol.* (in press).

Owen RW. (1989) Microscale and finescale variations of small plankton in coastal and pelagic environments. *J. Mar. Res.* 47:197-240.

Pedley TJ and Kessler JO. (1992) Hydrodynamic phenomena in suspensions of swimming microorganisms. *Annu. Rev. Fluid Mech.* 24:313-358.

Peters F, Arin L, Marrase C, Berdalet E, Sala MM. (2006) Effects of small-scale turbulence on the growth of two diatoms of different size in a phosphorus-limited medium. *J. Mar. Sys.* 61:134-148.

Kamykowski D, Reed RE, Kirkpatrick GJ. (1992) Comparison of sinking velocity, swimming velocity, rotation, and path characteristics among six marine dinoflagellate species. *Mar. Biol.* 113:319-328.

Kessler JO. 1985. Hydrodynamic focusing of motile algal cells. *Nature* 313:218-20.

Roberts AM, Deacon FM. (2002) Gravitaxis in motile micro-organisms: the role of fore-aft body asymmetry. *J. Fluid Mech.* 452:405-23.

Rothschild BJ, Osborn TR. (1988) Small-scale turbulence and plankton contact rates. *J. Plankton Res.* 10:465-474.

Rouson DW, Eaton JK. (2001) On the preferential concentration of solid particles in turbulent channel flow. *J. Fluid Mech.* 428:149-169.

Ruiz J, Macias D, Peters F. (2004), Turbulence increases the average settling velocity of phytoplankton cells. *Proc. Natl. Acad. Sci. USA.* 101:17720-17724.

Ryan JP, McManus MA, Sullivan JM. (2010) Interacting physical, chemical and biological forcing of phytoplankton thin-layer variability in Monterey Bay, California. *Cont. Shelf Res.* 30:7-16.

Rycroft CH, Grest GS, Landry JW, Bazant MZ. (2006) Analysis of granular flow in a pebble-bed nuclear reactor. *Phys. Rev. E.* 74: 021306.

Siegel DA. (1998) Resource competition in a discrete environment: why are plankton distributions paradoxical? *Limnol. Oceanogr.* 43:1133-1146.

Seymour JR, Simo R, Ahmed T, Stocker R. (2010) Chemoattraction to Dimethylsulfoniopropionate in the marine microbial food web *Science*. 329: 342-345.

Shaw RA. (2003) Particle-turbulence interactions in atmospheric clouds. *Ann. Rev. Fluid Mech.* 35:183-227.

Smayda TJ. (1997) Harmful algal blooms: their ecophysiology and general relevance to phytoplankton blooms in the sea. *Limnol. Oceanogr.* 42:1137-1153.

Squires KD, Yamazaki H. (1995a) Preferential concentration of marine particles in isotropic turbulence. *Deep Sea Res. I.* 42: 1989-2004.

Squires KD, Yamazaki H. (1995b) Addendum to the paper "Preferential concentration of marine particles in isotropic turbulence." *Deep Sea Res. I.* 43: 1865-1866.

Steele JH. (1974) Spatial heterogeneity and population stability. *Nature* 248:83

Stommel H. (1949) Trajectories of small bodies sinking slowly through convection cells *J. Mar. Res.* 8, 24-29.

Swift E, Taylor WR. (2007) Bioluminesce and chloroplast movement in the dinoflagellate *Pyrocystis lunula. J. Phycol.* 3: 77-81.

Taylor GI (1923) On the decay of vortices in a viscous medium. *Philos. Mag.* 46: 671-674.

Taylor FJR, Hoppenrath M, Saldarriaga JF. (2008) Dinoflagellate diversity and distribution. *Biodivers. Conserv.* 17:407-418.

Tennekes H, Lumley JL (1972) *A First Course in Turbulence*, MIT Press, Cambridge, MA.

Tiselius P. (1992) Behavior of *Acartia tonsa* in patchy food environments. *Limnol. Oceanogr.* 37:1640-51.

Tiselius P, Jonsson PR, Verity PG. (1993) A model evaluation of the impact of food patchiness on foraging strategy and predation risk in zooplankton. *Bull. Mar. Sci.* 53:247-64.

Uda M. (1938) Researches on "Siome" or current rip in the seas and oceans. *Geophys. Mag.* 11: 307-372.

Vanlerland ET, Peperzak L. (1984) Separation of marine seston and density determination of marine diatoms by density gradient centrifugation. *J. Plankton Res.* 6:29-44

Wang L-P, Maxey MR. (1993) Settling velocity and concentration distribution of heavy particles in homogeneous, isotropic turbulence, *J. Fluid Mech.* 256: 27-68.

Waters RL, Mitchell JG (2002) The centimetre-scale spatial structure of estuarine in vivo fluorescence profiles. *Mar Ecol Prog Ser.* 237:51–63.

Waters RL, Mitchell JG, Seymour JR. (2002) Geostatistical characterization of the centimeter scale spatial structure of in vivo flourescence. *Mar Ecol Prog Ser.* 251:49–58.

Yamazaki H, Mitchell JG, Seuront L, Wolk F, Li W. (2006) Phytoplankton microstructure in fully developed oceanic turbulence. *Geophys. Res. Lett.* 33: L01603.

Zhang Q, Lambert G, Liao D, Kim H, Robin K, Tung C, Pourmand N, Austin RH. (2011) Acceleration of emergence of bacterial antibiotic resistance in connected microenvironments. *Science.* 333:1764-1767.

Zirbel MJ, Veron F, Latz MI. (2000) The reversible effect of flow on the morphology of *Ceratocorys horrida. J. Phycol.* 36: 46-58.
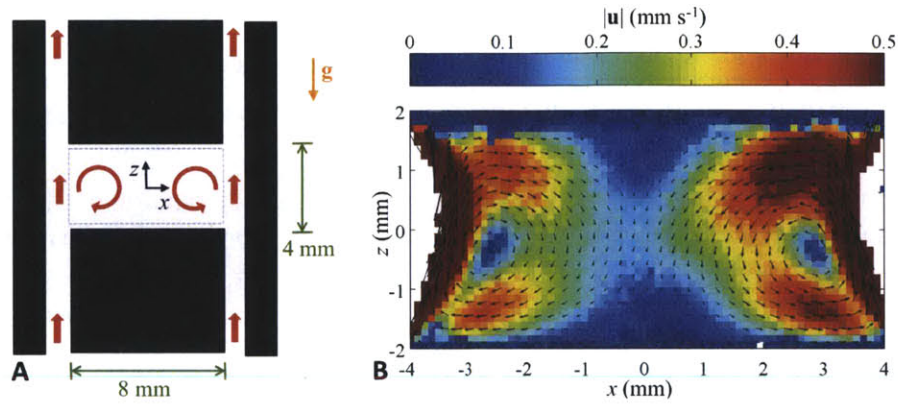
Figure 1: Cavity flow device (A) used to generate vortical flow (B) in experiments. Flow past the central cavity generates two recirculating vortices in the test section (dashed blue rectangle). The y-axis is directed into the plane and gravity, $\mathbf{g}$, acts is the $-z$ direction. In (B), arrows denote the local fluid velocity vector, $\mathbf{u}$, while color denotes the magnitude of fluid velocity $|\mathbf{u}|$.
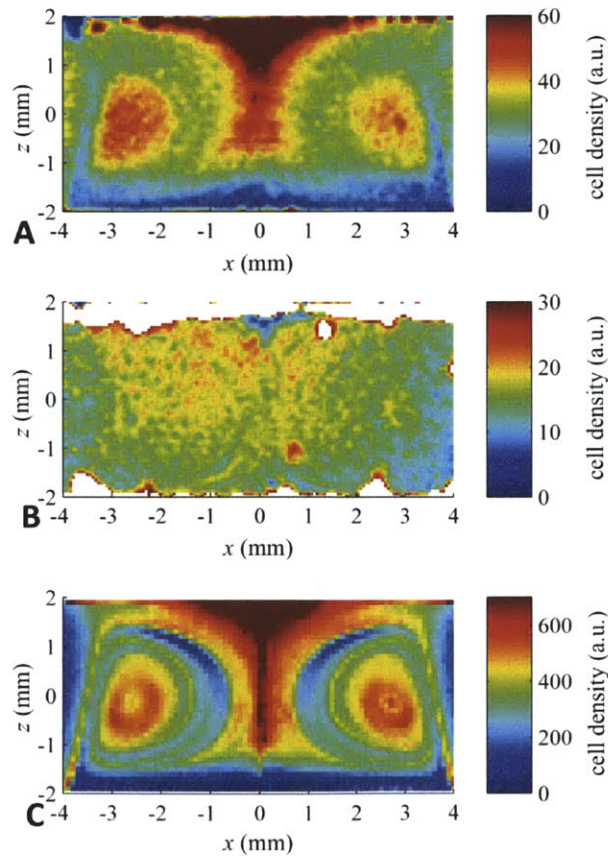
Figure 2: Histograms of cell density from experiments using live (A) and dead (B) cells, and from a model that simulates gyrotactic motility within the experimental flow (C).
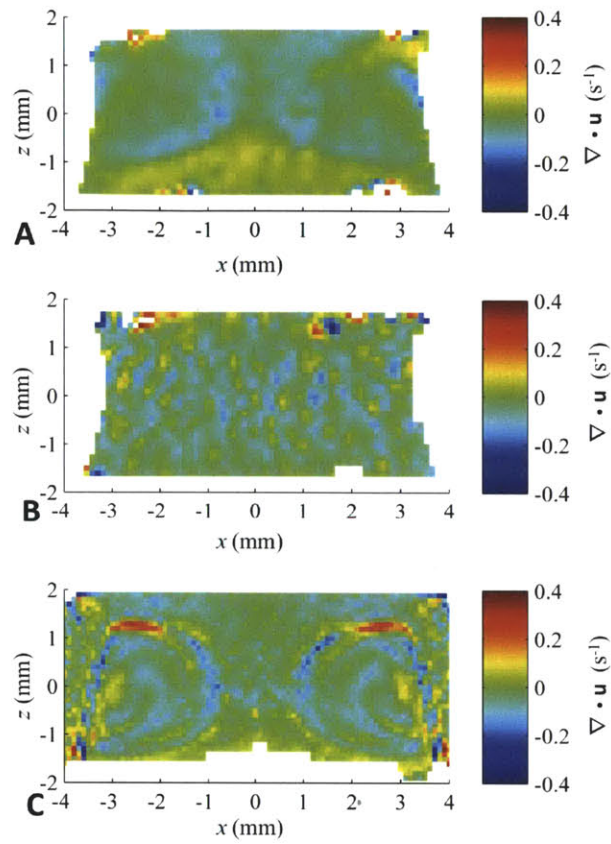
Figure 3: Divergence of cell velocity from experiments using live (A) and dead (B) cells, and from a model that simulates gyrotactic motility within the experimental flow (C).
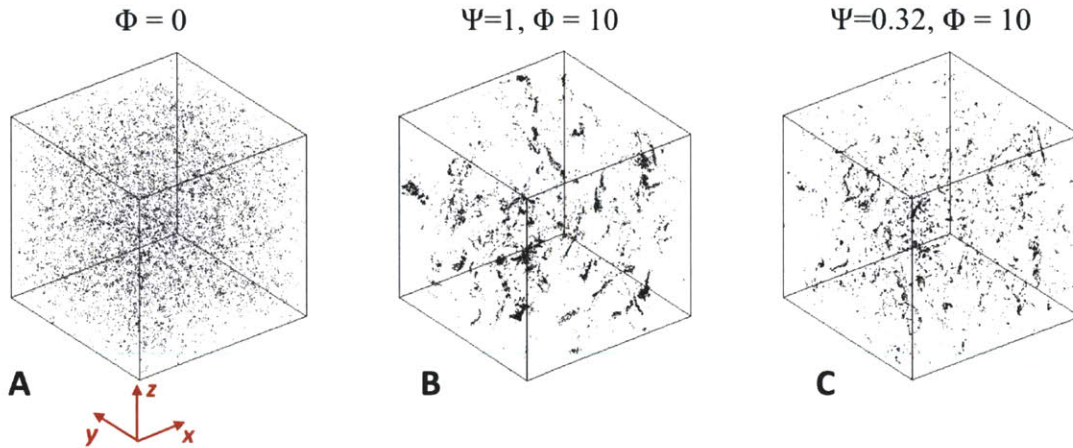
Figure 4: Patch distributions from cells with three different $[\Psi, \Phi]$ values generated by an identical turbulent flow with a Taylor Reynolds number of $Re_\lambda = 60$. We define a 'patch' as the 10,000 most aggregated cells from a total population of 100,000. Non-motile cells remain Poisson distributed; with much less intense patches (A) compared to the highly aggregated patches composed of motile cells (B & C).
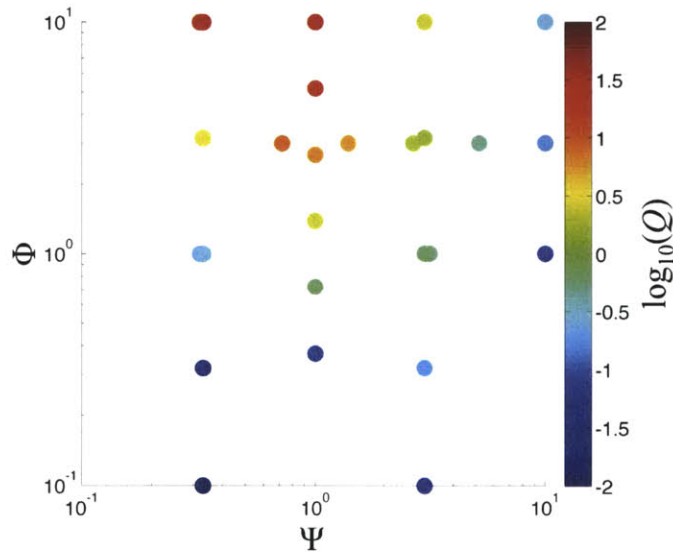
Figure 5: The normalized patch concentration, Q, as a function of the relative cell stability, Ψ, and swimming velocity, Φ. The intensity of patches increases monotonically with cell swimming speed and peaks when cells have a non-dimensional stability of $\Psi \sim 1$. All simulations performed within the identical flow ($Re_\lambda = 60$).
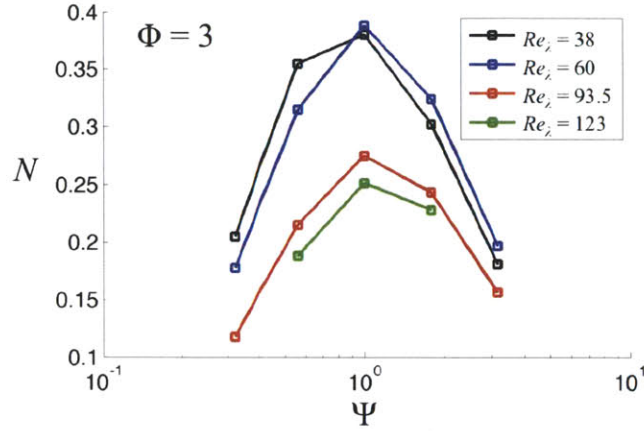
Figure 6: The effect of Taylor Reynolds number, Re_λ, on aggregation intensity, N. Generally, the degree of aggregation decreases as Re_λ increases, as a result of enhanced mixing by integral scale fluid motion. Regardless of the Re_λ, the maximum level of aggregation occurs at a $\Psi\sim 1$, confirming that cell aggregation occurs at the Kolmogorov scale.
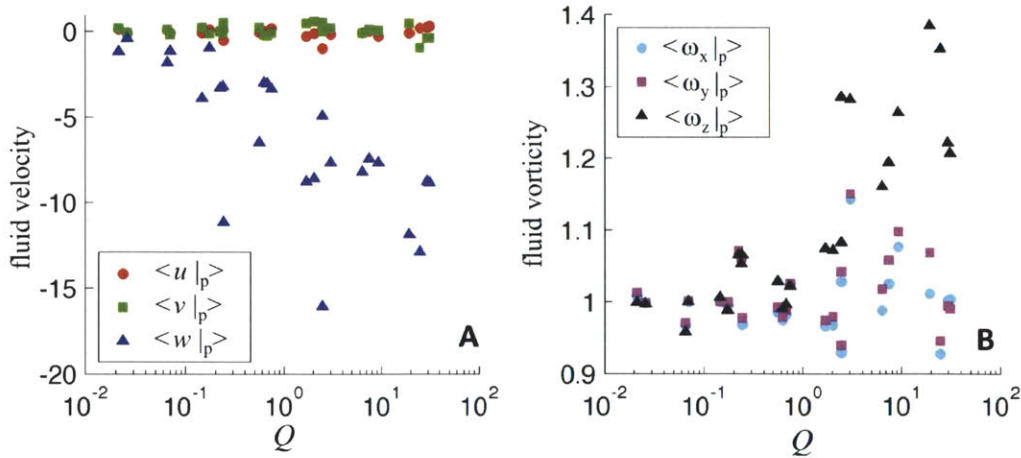
Figure 7: The fluid properties within patches for 27 simulations with different $[\Psi, \Phi]$ values ($Re_\lambda = 60$). Here, $[<u|_p>, <v|_p>, <w|_p>]$ are the mean fluid velocities (A) and $[<\omega_x|_p>, <\omega_y|_p>, <\omega_z|_p>]$ are the mean normalized fluid vorticity magnitude (B) interpolated at the position of cells within patches in the x, y, and z directions, respectively. As the patch concentration increases (increasing Q), patches more likely to reside in regions of enhanced downwelling (small $<w|_p>$) and increased levels of z vorticity (large $<\omega_z|_p>$).
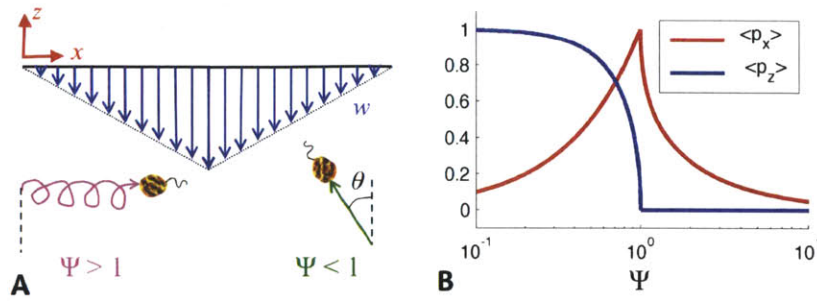
Figure 8: The speed at which gyrotactic cells swim into regions of increased downwelling (larger w) depends on both Ψ and Φ. Panel A: Assuming simple shear, unstable cells ($\Psi>1$, pink trajectory) tumble end over end towards regions of increased downwellling, whereas stable cells ($\Psi<1$, green trajectory) swim smoothly at angle to the vertical, given by $\sin\theta = \Psi$. Panel B: These different motility patterns give rise to a non-trivial dependence in a cell's mean orientation in the horizontal, $\langle p_x \rangle$, and vertical, $\langle p_z \rangle$, directions on Ψ. The speed at which cells swim in the horizontal and vertical directions, is linearly proportional to $[\langle p_x \rangle, \langle p_z \rangle] = [\Psi, (1- \Psi^2)^{1/2}]$ for $\Psi<1$ and $[\langle p_x \rangle, \langle p_z \rangle] = [\Psi - (\Psi^2 - 1)^{1/2}, 0]$ for $\Psi>1$. Intuitively, increasing vorticity orients a larger proportion of a cell's motility in the x direction, until it reaches a maximum at $\Psi = 1$ when cell motility is directed perfectly in the horizontal (red line). Tumbling is initiated for $\Psi > 1$, negating its ability to swim upwards (blue line). As vorticity increases further, cells tumble with a greater temporal frequency, spending more time looping up and down and, therefore, reducing their mean horizontal projection (red line).
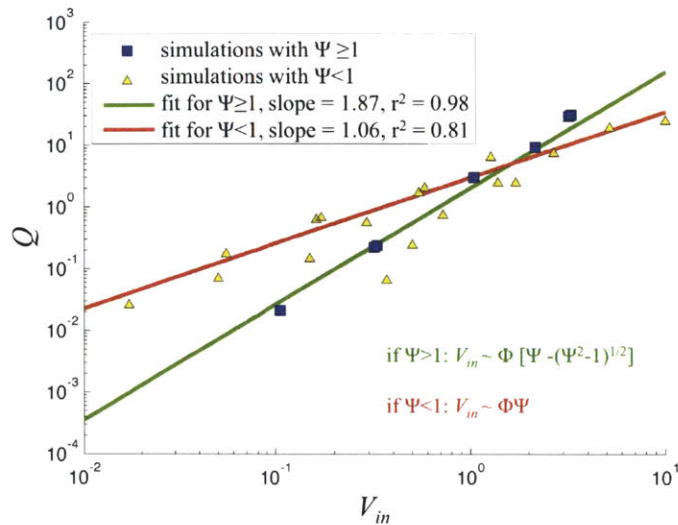
Figure 9: The normalized patch concentration in the DNS simulations, Q, is well predicted by, V_{in}, the estimated speed at which cells swim into downwelling regions. Assuming that the flow is steady and Kolmogorov-scale regions of downwelling are composed of simple shear (Figure 8a), V_{in}, is the mean horizontal projection of motility directed in the horizontal direction $\langle p_x \rangle$, (Figure 8b), multiplied by the normalized swimming velocity, Φ. Two different scaling regimes emerge: for $\Psi \geq 1$ the fitted slope suggests a quadratic power-law dependence of V_{in} on Q, whereas for $\Psi < 1$ the slope indicates a linear correlation.

Methods and Materials:

Experimental setup

The experimental device (Fig. 1A) was constructed from acrylic using traditional milling techniques. Flow through the side channels was generated by a syringe pump (Harvard Apparatus, PHD 2000), containing two identical syringes (Monoject, 140 ml). Flexible tubing (Cole Parmer C-Flex, ID 3mm) was used to connect the syringes to the experimental device and to a reservoir that collected the effluent phytoplankton culture. A continuous wave 8mW Helium-Neon laser (Uniphase model 1105P) was used to create a light sheet with a thickness of 1.6 mm. All images were captured with at 20 Hz with a CCD camera (PCO 1600, Cooke) attached to a stereomicroscope (SMZ1000, Nikon).

Phytoplankton culture

Cultures of *Heterosigma akashiwo* were grown by inoculating 2 ml of exponential phase culture in 25 ml of f/2 medium, then incubating at 25°C under continuous fluorescent illumination (70 μE m^{-2}s^{-1}). Cells were harvested after 21 days and 75 ml of culture was diluted in 500 ml of f/2 media for use in the experimental device.

Image analysis

Histograms of live and dead cell density (Figure 1A and 1B) were generated from a single period of uninterrupted flow lasting 4.4 minutes (5300 images) and 3.8 minutes (4540 images) respectively. The [x,y] positions of cell centroids were counted within 114 μm x 114 μm bins using a custom Matlab routine.

Divergence fields (Figure 2A and 2B) were generated from four and three different 'experiments' for the live and dead cases respectively. (A single experiment is composed of a single period of uninterrupted flow.) We tracked individual cells between subsequent frames to obtain the cell's velocity [u, v] and its instantaneous location [x, y]. Cell velocities were averaged within 114 μm x 114 μm bins find the mean cell velocity vector at each bin location, from which the divergence ($= \partial u/\partial x + \partial w/\partial y$) was calculated. For live cells, we processed a total of 13,800 images to obtain a total of 591,142 cell trajectories. For dead cells, we processed a total of 12,240 images to obtain a total of 1,011,954 cell trajectories.

Direct Numerical Simulations of Turbulence

The flow is simulated in a fully periodic domain, of size $2\pi \times 2\pi \times 2\pi$, using a Fourier pseudo-spectral code. The turbulent flow is sustained by a random forcing at low wavenumbers to achieve a statistically stationary state. The simulation procedure is similar to that used by Wang and Maxey (1993) with the random forcing term applied over a shell of small wavenumbers (Eswaran and Pope 1988). This unsteady forcing drives the integral length scales of the flow. The forcing parameters are the same in all simulations and the energy input from the forcing and the viscous dissipation rate, ε, were found to be equivalent. A sufficiently large separation between production and dissipation scales ensures that the small-scale fluid structures exhibit the universal characteristics of a turbulent flow. The trajectories of gyrotactic organisms are integrated using a second order Adams-Bashford scheme. Fluid flow properties (velocity and vorticity) at the particle are calculated using a 3 dimensional linear interpolation at each time step of the simulation. To fully resolve the Kolmogorov scale, we increase the number of mesh points as Re_λ increases, which in turn requires an increased number of cells to conserve cell concentration. A table of the simulation parameters is given below.

Re_λ	Mesh Size	Number of cells
39	64^3	12,500
60	128^3	100,000
93	256^3	800,000
123	512^3	3,200,000

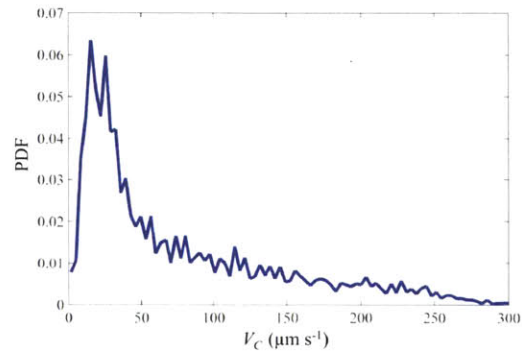Table 1: Characteristics of the Direct Numerical Simulations of Turbulence.

Figure S1: Swimming velocity, V_C, of *Heterosigma akashiwo* as measured within the experimental device.

SUMMARY AND FUTURE DIRECTIONS

In this thesis and appendix, we proposed that the interaction of phytoplankton morphology and fluid shear can drive thin layers and microscale cell accumulations, and changes in the way light propagates through the water column.

In chapter 1, we demonstrated that vertical gradients in horizontal vorticity trigger thin layer accumulations of motile phytoplankton by stifling vertical migration. Above a critical fluid vorticity cells tumble end over end, trapping them at depth. We show that the gyrotactic reorientation timescale, B, is a good predictor of the magnitude of shear required to overturn cells, suggesting that B might be as important as other, classical measurements of motility, like swimming velocity, in the determination of cell fate. While B is widely used in models of bioconvection and has been predicted for a few of the model phytoplankton species used in the laboratory experiments, very little is known about B for marine species known to form thin layers. The relative value of B is likely governed by evolutionary tradeoffs: Very unstable cells (with large B) would be easily overturned by arbitrarily small fluid vorticities, rendering them incapable of efficient vertical migration, whereas overly stable cells would be unmaneuverable, prohibiting them from chemotaxing to more favorable nutrient environments (Seymour et al. 2008) or from escaping from a predator's feeding current (Jakobsen 2001). While there are no theoretical limits to how unstable a cell can be (a perfectly symmetric cell would have B = ∞), a cell's theoretical maximum stability is limited by geometric considerations (Chapter 1, Supplemental Material). Such tradeoffs might be partly responsible for the wide diversity in observed motile phytoplankton morphologies (Taylor et al. 2008) and could be a fruitful path for further work.

The implications of gyrotactic trapping on phytoplankton fitness are unclear. While aggregation into thin layers appear to be beneficial to some toxic species by stifling grazing (Bjornsen and Nielsen 1991, Nielsen et al. 1990), for many thin layers it seems to confer an enhanced predation risk due to the enhanced number of zooplankters often found in their midst (Benoit-Bird et al. 2010). Supporting the latter, zooplankton predators possess finely tuned strategies, known as 'area-restricted searches', to capitalize on patchiness in the distribution of phytoplankton (Tiselius 1992). Whether phytoplankton 'intend' to become trapped together within thin layers for some specific purpose or whether it merely occurs 'by accident', is unknown. In the future, novel field measurements that observe motility in $situ$ may shed light on this issue (after Malkiel et al. 1999). Specifically, measurement of the B of cells within thin layers may allow researchers to unravel how the relative fitness of different phytoplankton species changes as a function of ambient flow conditions. Such knowledge might offer clues on why during certain motile species are able to dominate their competitors during harmful algal bloom events.

In addition, it is unknown whether phytoplankton cells possess the ability to actively sense shear and resist being overturned by the flow. Only some phytoplankton cells have the ability to sense the direction of gravity (Lebert and Häder 1996), thus cells undergoing shear-induced tumbling might not be able recognize that attempting to swim

is futile for the purposes of vertical migration. To experimentally observe the role of 'active' behavior in gyrotactic trapping, one could estimate B in quiescent conditions by measuring cell reorientation in response to stochastic perturbations in flagellar beat (after Hill and Häder 1997) and compare these results to those obtained with the same phytoplankton culture under hydrodynamic shear (as presented in Chapter 1). A smaller estimate of B using the latter technique would indicate that cells could actively resist being overturned.

Aspects of the mechanics of gyrotactic trapping also remain to be explored. While we demonstrated this mechanism using a laminar coherent flow in our experiments, thin layers in the Ocean experience fluctuations resulting from turbulent fluid motion, in addition to the mean flow. The influence of turbulence on gyrotactically-trapped cells is not yet known, but is currently being pursued by Martin Hoecker-Martinez and William Smyth at Oregon State University. One possibility is that turbulent shear fluctuations superimposed upon a mean shear could enhance cell trapping.

In chapters 2 and 3, we showed that turbulence drives microscale aggregations of cells. Two dimensionless numbers, characterizing cell stability and swimming speed relative to the flow, control cell aggregation. In the analytical Taylor-Green vortex flow we found that gyrotactic motility can be described with a relatively simple set of coupled ordinary differential equations, which give rise to diversity of aggregation regimes. We tested this mechanism by subjecting live gyrotactic cells to vortical flows with dimensions similar to those that they would experience in realistic marine environments. We found that live cells formed tightly clustered aggregations, in agreement with a three-dimensional model of gyrotaxis. We then implemented the same gyrotaxis model in an isotropic turbulent flow and found that motile cells tend to aggregate in downwelling regions of Kolmogorov-scale fluid motion. A simple metric, based on the two dimensionless parameters, was developed to estimate a population of cells propensity to aggregate within turbulence.

While particle inertia has long been known to aggregate particles within turbulent flows and has attracted a number of experimental and theoretical studies, the work contained in this chapter opens a new class of aggregation dynamics based on cell motility. The simple model contained in Chapter 2 could be fertile ground for a future studies that resolve the transitions between the various regimes in the Ψ-Φ phase space using the tools of dynamical systems.

In addition, future experiments that image live phytoplankton swimming within isotropic turbulence could shed important light on gyrotaxis within turbulent flow. The tools of holography, which allow a three-dimensional reconstruction of both particle locations and the velocity field, have been applied with great success to resolve the dynamics of inert particles and droplets in a turbulent flow (Gopalan et al. 2008). Two possibilities exist in this arena: using a holographic system mounted to an autonomous underwater vehicle to observe the response of motility in situ to natural marine turbulence (after Malkiel et al. 1999) or observing laboratory cultures of phytoplankton within isotropic grid-driven turbulence (after Gopalan et al. 2008). By measuring aggregation of different

species under different turbulent conditions, one could develop a Ψ-Φ phase portrait of aggregation (similar to figure 5 in Chapter 3) and validate the power-law relationship between V_{in} and Q.

The exciting possibility that cells could transverse Ψ-Φ phase space to favor aggregation or random distributions could be tested by measuring the gyrotactic reorientation parameter and swimming velocity of phytoplankton over their life cycle. Such could be accomplished by through the 'synchronization' of a phytoplankton culture to ensure that all cells are in exactly the same stage of growth (Massie *et al.* 2010). By inducing cells to sexually reproduce, one could potentially observe if cells are more apt to aggregate than during periods of asexual reproduction.

In Part One of the Appendix, we proposed that the shear-induced alignment of elongated microorganisms could alter the propagation of light through the upper ocean. A coupled fluid mechanics and optics model demonstrated that a cell's Peclet number, which parameterizes the competition between alignment by shear and Brownian rotational diffusion, exerts a significant control on a cell's rate of optical scattering. We find that trivial amounts of shear can increase the optical backscatter from a bloom of elongated phytoplankton cells by more than 30%.

It is well known that thin layer aggregations of phytoplankton can significantly attenuate light, reducing its availability for phytoplankton below them in the water column (Sullivan *et al.* 2010). Furthermore, it is well known that thin layers composed of both motile (Sullivan *et al.* 2010) and non-motile (Ryan *et al.* 2008) species tend to coincide with depths of enhanced horizontal vorticity (Appendix: Part Two). Might the tendency for cells to collocate with sheared regions of the water column be a strategy for elongated cells to enhance scattering via preferential alignment, thereby stifling the growth of competitors by reducing their light availability? These interactions could be probed with ecological models that probe the tradeoffs of such behaviors.

Another reason that cells might want to aggregate in regions of enhanced shear is because it allows them to more it more effectively acquire light. Shear allows cells to achieve alignment perpendicular to incident light more frequently, reducing the likelihood that a cell's multiple chloroplasts shade one another. One could envision measuring rates of growth or oxygen production as a function of the ambient shear rate to glean if this effect is significant.

References:

Benoit-Bird KJ, Moline MA, Waluk CM, Robbins IC. (2010) Integrated measurements of acoustical and optical thin layers I: vertical scales of association. *Cont. Shelf Res.* 30:17-28.

Bjornsen PK, Nielsen TG. (1991) Decimeter scale heterogeneity in the plankton during a pycnocline bloom of *Gyrodinium aureolum. Mar. Ecol. Prog. Ser.* 73:263-67.

Hill NA, Häder DP. (1997) A biased random walk model for the trajectories of swimming micro-organisms. *J. Theor. Biol.* 186:503-26.

Jakobsen HH. (2001) Escape response of planktonic protists to fluid mechanical signals. *Mar. Ecol. Prog. Ser.* 214:67-78.

Gopalan B, Malkiel E, Katz J. (2008) Experimental investigation of turbulent diffusion of slightly buoyant droplets in locally isotropic turbulence. *Phys. Fluids.* 20:095102.

Lebert M, Häder D-P. (1996) How *Euglena* tells up from down. *Nature.* 379:590.

Malkiel E, Alquaddoomi O, Katz J. (1999) Measurements of plankton distribution in the ocean using submersible holography *Meas. Sci. Technol.* 10: 1142–1152.

Massie TM, Blasius B, Weithoff G, Gaedke U, Fussmann GF. (2010) Cycles, phase synchronization and entrainment in single-species phytoplankton populations. *Proc. Nat. Acad. Sci. USA.* 107:4236-4241.

Nielsen TG, Kiorboe T, Bjornsen PK. (1990) Effects of a *Chrysochromulina polylepis* subsurface bloom on the planktonic community. *Mar. Ecol. Prog. Ser.* 62:21-35.

Ryan JP, McManus MA, Paduan JD, Chavez FP. (2008) Phytoplankton thin layers caused by shear in frontal zones of a coastal upwelling system. *Mar. Ecol. Prog. Ser.* 354:21-34.

Ryan JP, McManus MA, Sullivan JM. (2010) Interacting physical, chemical and biological forcing of phytoplankton thin-layer variability in Monterey Bay, California. *Cont. Shelf Res.* 30:7-16.

Seymour JR, Marcos, Stocker R (2008) Resource patch formation and exploitation throughout the marine microbial food web. *Am. Nat.* 173: 15-28.

Sullivan JM, Donaghay PL, Rines JEB. (2010) Coastal thin layer dynamics: consequences to biology and optics. *Cont. Shelf Res.* 30:50-65.

Taylor FJR, Hoppenrath M, Saldarriaga JF. (2008) Dinoflagellate diversity and distribution. *Biodivers. Conserv.* 17:407-418.

Tiselius P. (1992) Behavior of *Acartia tonsa* in patchy food environments. *Limnol. Oceanogr.* 37:1640-51.

APPENDIX

PART ONE:

Microbial alignment in flow changes ocean light climate

Marcos[1†], Justin R. Seymour[2,3,4†], Mitul Luhar[2†], William M. Durham[2†],
James G. Mitchell[3], Andreas Macke[5], Roman Stocker[2†*]

[1]Department of Mechanical Engineering, Massachusetts Institute of Technology, 77
Massachusetts Avenue, Cambridge, MA, 02139, USA

[2]Department of Civil and Environmental Engineering, Ralph M. Parsons Laboratory,
Massachusetts Institute of Technology, 77 Massachusetts Avenue, Cambridge, MA,
02139, USA

[3]School of Biological Sciences, Flinders University, GPO 2100, Adelaide, SA, 5001,
Australia

[4]Plant Functional Biology and Climate Change Cluster (C3), University of Technology,
PO Box 123, Broadway, NSW, 2007, Australia

[5]Leibniz Institute for Tropospheric Research, Permoserstraße 15, Leipzig, 04318,
Germany

[†]Authors contributed equally

**The growth of microbial cultures in the laboratory is often informally assessed with
a quick flick of the wrist: dense suspensions of microorganisms produce translucent
'swirls' when agitated. Here, we rationalize the mechanism behind this phenomenon
and show that the same process may affect the propagation of light through the
upper ocean. Analogous to the shaken test tubes, the ocean can be characterized by
intense fluid motion and abundant microorganisms. We demonstrate that the swirl
patterns arise when elongated microorganisms align preferentially in the direction
of fluid flow and alter light scattering. Using a combination of experiments and
mathematical modeling, we find that this phenomenon can be recurrent under
typical marine conditions. Moderate shear rates (0.1 s⁻¹) can increase optical
backscattering of natural microbial assemblages by over 20% and even small shear
rates (0.001 s⁻¹) can increase backscattering from blooms of large phytoplankton by
over 30%. These results imply that fluid flow, currently neglected in models of
marine optics, may exert an important control on light propagation, influencing
rates of global carbon fixation and how we estimate these via remote sensing.**

Sunlight attenuates as it passes through seawater, exerting a fundamental control on
marine productivity by limiting the depth at which photosynthesis can occur (1-3). The
extinction of sunlight is governed by the inherent optical properties (IOPs) of seawater,
which are largely determined by the light scattering characteristics of suspended living

66

and non-living microscopic particles (4). From a technological perspective, backscattered sunlight enables measurements of primary production rates and detection of phytoplankton blooms via remote sensing (3, 5). A major contribution to the IOPs comes from bacteria and phytoplankton (6), as a consequence of their size, pigment content and high concentration (10^9–10^{13} m^{-3}). For example, phytoplankton larger than 3 μm were recently found to be responsible for 50% of the light backscattered in the open ocean (7). While light scattering by marine particles is now routinely computed by optical models (4, 8), frequent discrepancies between predicted and measured IOPs highlight the need to better understand the complex underlying physics (6). Here, we demonstrate that fluid motion can alter the scattering characteristics of seawater by preferentially aligning elongated microbes, indicating that flow modulates the propagation of light through the ocean.

Intriguingly, the biophysical mechanism underlying this process is the same that underpins a method routinely used to qualitatively assess microbial growth in the laboratory. When liquid cultures of microorganisms are shaken within test tubes, visible millimeter-scale patterns often appear (Fig. 1a), almost instantaneously, and persist for several (~1–5) seconds after shaking has ceased (Movie S1). We have observed these patterns in suspensions of several species of bacteria and phytoplankton. Patterns arise as translucent swirls and initially appear paradoxical, as they suggest that stirring causes locally enhanced cell concentrations, rather than homogenizing the suspension. However, neither biological nor physical mechanisms can generate and dissipate cell accumulations so rapidly. The occurrence of patterns in cultures of non-motile and dead cells rules out active congregation by cell motility, and neither sedimentation nor particle inertia are capable of producing aggregations of micron scale organisms (9, 10).

Results and Discussion

Swirls in Culture Tubes.

We examined the pattern formation phenomenon by performing a classic fluid mechanics experiment. Towing a cylinder through a suspension of the bacteria *Pseudoalteromonas haloplanktis* revealed the well-known von Karman vortices (11) (Fig. 1b). This indicates that the patterns reflect gradients in fluid velocity and the microbial suspension acts as a rheoscopic ('flow-visualizing') fluid (12, 13). In rheoscopic fluids, hydrodynamic shear preferentially aligns elongated particles with the flow direction. Because optical scattering is a function of particle orientation (12, 13), particles aligned along different shear planes scatter light differently, mirroring the spatial distribution of shear in the flow. This assessment is supported by our observation that swirls form in test tubes containing rod-shaped and flagellated bacteria, but not with the spherical cyanobacterium *Prochlorococcus* or with 1–5 μm spherical latex beads. Furthermore, when exposed to a vortex generated in a microfluidic device, *P. haloplanktis* displayed strong alignment with the flow streamlines (Fig. 1a, inset).

A Mathematical Model Coupling Alignment by Shear with Light Scattering.

To predict how light scattering by a microbial suspension is affected by shear-induced alignment and to determine the magnitude of this effect in the ocean, we developed a mathematical model that couples fluid dynamics and optics. In most ocean optics models particles are treated as spheres (6) or randomly oriented spheroids (14-16). We model particles as prolate spheroids and explicitly compute their orientation distribution as a function of the shear rate, S (for example, the vertical gradient, du/dz, in horizontal fluid velocity, u). The particle's mean light scattering properties are then calculated as a weighted average over all orientations. The probability distribution, $c(\theta, \phi)$, that the particle's major axis is oriented along polar and azimuthal angles (θ, ϕ) in a spherical coordinate system (17) is computed by solving the steady Fokker–Planck equation (18, 19), $D\nabla^2 c - \nabla \cdot (\bar{\omega} c) = 0$, where D is the rotational diffusivity and $\bar{\omega}(\theta,\phi)$ the shear-induced particle rotation rate (Methods). The Fokker–Planck equation, which governs the degree of alignment of particles with the flow, parameterizes the competition between Brownian rotational diffusion and shear. The former randomizes cell orientation via stochastic collisions with water molecules, whereas the latter causes elongated particles to rotate with deterministic periodic orbits in which cells spend most of their time aligned with the flow. The time scale for a spheroid of aspect ratio r to align with the flow is $(r^2+1)/(rS)$ (Methods). The relative importance of shear and rotational diffusion is quantified by the Peclet number, $Pe = S/D$: large Peclet numbers result in marked alignment, whereas low Peclet numbers yield random orientation. We found that shear rates characteristic of the marine environment can induce strong anisotropy in the orientation of particles of size and shape typical of marine microbes (Fig. 2a). For example, the proportion of time spent by a 1×5 μm spheroid within ±10° of the flow direction is seven times larger at $Pe = 100$ compared to the case of isotropic orientation ($Pe = 0$).

Light scattering by a particle is quantified by its forward and backward optical scattering cross-sections, which measure the ratio of the rate by which energy of a plane parallel wave is scattered by the particle – in the forward and backward directions, respectively – to the incident irradiance on it (20). The total scattering is the sum of forward and backward scattering. We computed the total and backward scattering cross-sections, σ_{tot} and σ_b, for each orientation (θ, ϕ), and found them to be strongly orientation dependent (Fig. 2b). For example, a 1×5 μm spheroid aligned with the incident light has a 20-fold smaller σ_b than the perpendicular orientation. From knowledge of σ_{tot} and σ_b for each orientation, the mean scattering cross sections,

$$\bar{\sigma}_{tot/b} = \int\limits_{0}^{2\pi} \int\limits_{0}^{\pi} \sigma_{tot/b}(\theta,\phi)c(\theta,\phi)\sin\theta d\theta d\phi$$ were then computed as a weighted average over all

particle orientations, with weights given by the probability distribution $c(\theta, \phi)$.

68

Rheoscopic Alignment and Light Transmission

We experimentally quantified the impact of shear on the optical properties of a microbial suspension by measuring the light transmitted through a culture of *Escherichia coli* bacteria exposed to shear in a Couette device (Fig. 3; Methods). When a 2.9 s^{-1} mean shear rate was applied, transmission of light through the bacterial culture increased considerably, while stopping the flow resulted in a return back to the baseline transmissivity (Fig. 3). Relative to quiescent conditions, shear reduced the mean scattering cross-section of the bacteria by 16%. The increase in light transmission under shear might be at first surprising, as shear tends to align bacteria horizontally such that they expose more frontal area to the incident light. However, this effect arises because *E. coli* is comparable in size to the wavelength of light and has been previously observed for red blood cells (21). Our mathematical model predicts a 13% decrease in the mean scattering cross-section, providing further confirmation that the change in transmittance was caused by a shear-induced modulation of optical scattering.

Effect of Rheoscopic Alignment in Aquatic Environments

We propose that preferential orientation of particles in flow (Fig. 2*a*), coupled with the dependence of scattering on orientation (Fig. 2*b*), can strongly influence the IOPs of the ocean (Fig. 4), because many planktonic microbes are elongated (14). Phytoplankton larger than 2 μm, for example, have a mean aspect ratio of ~5. We hypothesize that the orientation of elongated microbes is organized by temporally coherent shear flows produced by wind, currents, tides, fronts, or internal waves, or by ephemeral turbulent shear. An important distinction needs to be made between coherent and turbulent shear. The latter is often stronger (up to 10 s^{-1}) (22) than the former (up to 0.1 s^{-1}) (23, 24), but varies in orientation over small distances (the Kolmogorov scale, mm–cm) (22). In contrast, horizontal flows can produce coherent shear over meters to tens of meters of depth (23, 24). Therefore, the effect of turbulence on light scattering will be locally more pronounced, but coherent shear will yield a larger cumulative effect by inducing horizontal alignment of plankton (Fig. 4*b*) over considerably larger depths.

We computed light scattering by microorganisms of various shapes and sizes under typical marine shear rates (0.001–10 s^{-1}; Fig. 2*c*). Results show that large bacteria (1×2 μm spheroids) will experience alignment only under strong turbulence ($S = 10$ s^{-1}). Flagellated bacteria, having higher aspect ratio (1×5 μm), show an increase in backscattering of ~30% at $S = 1$ s^{-1}. An increase in either size or elongation enhances the effect at small shear rates. Small phytoplankton (3×6 μm) exposed to moderate shear rates (0.2 s^{-1}) show a 10% increase in backscattering, whereas larger phytoplankton (10×50 μm) display an increase in backscattering of ~30% even at very low shear rates (0.001–0.01 s^{-1}).

Assemblages of multiple species were modeled by weighting the contribution of each species by its number density (Methods). We considered the case of seven microbial components, with sizes, number densities and aspect ratios summarized in Table 1.

Contrary to the dense cultures typical of laboratory experiments, these represent realistic microbial concentrations in the ocean. We found that a shear rate of $S = 0.1$ s^{-1} increases backscattering by 21% and total scattering by 13%, indicating that rheoscopic alignment can significantly alter marine IOPs. However, the effect of shear on light climate will vary with the local particle size and shape spectra. In this example, the primary contribution comes from ultra-nanoplankton and larger nanoplankton (Table 1). In general, optical scattering from smaller microbes (picoplankton), even when highly elongated (e.g. viruses), will not be altered by shear, because Brownian rotational diffusion, which is proportional to particle size to the power of -3 (see Methods), renders orientation isotropic at typical marine shear rates. Scattering by spherical microbes will also be unaffected. The effect of this mechanism will be most pronounced when medium to large plankton (Fig. 2c), having large aspect ratio, are present in the water at high concentrations, such as during a bloom of an elongated or chain-forming phytoplankton species.

Conclusions

These results indicate that a subtle interplay of biology, fluid dynamics and optics may shape the light climate in aquatic systems. Though rheoscopic alignment has long been part of the toolbox of experimental fluid dynamicists to visualize fluid flow, its potential effect on light propagation in the ocean has not before been recognized. By altering the way that light is transmitted through the upper ocean (Fig. 4), fluid flow may have profound physical and biological consequences. Because the light climate plays a pivotal role in phytoplankton ecology, this phenomenon may exert a previously neglected selection pressure on phytoplankton community composition and ultimately affect primary production levels by altering rates of light attenuation. Additionally, because remote sensing relies on the backscattering of light from ocean surface waters, shifts in IOPs driven by rheoscopic alignment may affect estimates of chlorophyll concentration obtained from satellite measurements of ocean color (5, 7). These results provide further evidence that biophysical interactions occurring at the microscale can play a key role in global scale marine processes.

Materials and Methods

Light transmission experiments. The non-flagellated *E. coli* strain VS115 was grown in LB medium to mid-exponential phase ($OD_{600} = 0.42$). Cultures were placed between two parallel circular Plexiglas plates (Fig. 3), spaced $H = 5$ mm apart, the upper one fixed and the lower one rotating at 0.5 Hz, producing a shear rate $S = 2.9$ s^{-1} at the measurement location. A collimated light beam (Nikon, NI-150) was passed vertically through the suspension and the transmitted light was measured with a light meter (Newport, 2832-C) and recorded at 25 Hz. The normalized intensity I_q was calculated by dividing the instantaneous intensity by the intensity under the initial quiescent conditions. To compute the change in scattering cross-section due to shear, $\Delta\bar{\sigma}_{tot}$, relative to quiescent conditions, we used Beer's law, $I_q = \exp(-\Delta\bar{\sigma}_{tot} N H)$, where N is the concentration of particles, and

70

the definition of optical density, $10^{-OD} = \exp(-\bar{\sigma}_{tot}NH_{OD})$, where OD was measured separately in an $H_{OD} = 0.8$ mm wide cuvette. Observation of >2000 bacteria with an inverted microscope (Nikon TE2000) showed that VS115 cells are 1.1×3.5 μm spheroids. Control experiments were performed with LB alone. The measurement error in I_q was ~0.03 and resulted primarily from small inhomogeneities in the Plexiglas surfaces.

Towed cylinder experiment. A 200 ml suspension of *P. haloplanktis* bacteria (ATCC 700530; cell body ~2×1 μm), grown in 1% Tryptic Soy Broth to mid-exponential phase ($OD_{600} = 0.44$), was placed in a 20×20×1 cm Perspex container. A 0.63 cm diameter cylinder was towed through the 0.5 cm deep bath of bacteria at 3.3 cm s^{-1}. Illumination was provided from underneath by an overhead projector and images were captured from above at 25 Hz using a stereomicroscope (Nikon, SMZ1000) and a CCD camera (Cooke, PCO1600).

Microfluidic experiment. *P. haloplanktis* (grown as above) were imaged within a microfluidic vortex (25) using an inverted microscope (as above). Significant alignment with streamlines occurred at $S > 2.8$ s^{-1}.

Coupled model for particle orientation and optical scattering. To compute the scattering properties of a microbial suspension exposed to a constant, uniform shear rate, S, we coupled a probabilistic model of particle orientation to models that calculate the optical scattering induced by a spheroidal particle with arbitrary orientation. The probability density function of particle orientation, $c(\theta, \phi, t)$, is governed by the Fokker–Planck equation (18, 19), which expresses the balance between a deterministic 'drift' process, here the rotational velocity of a spheroid $\bar{\omega}$ induced by shear, and a stochastic forcing, which in our case is the Brownian rotational diffusion of a spheroid (parameterized by its rotational diffusivity, D). Since we are interested in the long-term distribution of particle orientation, we compute the steady-state probability distribution, $c(\theta, \phi)$, by numerically integrating the steady Fokker-Planck equation (COMSOL Multiphysics, Natick, MA).

The rotation rate of a spheroid, $\bar{\omega} = \dot{\phi}\hat{e}_\phi + \dot{\theta}\hat{e}_\theta$, in a flow with constant, uniform shear rate is given by the well-known Jeffery-orbit equations (26),

$$\dot{\phi} = -\frac{S}{r^2+1}\left(r^2 \sin^2\phi + \cos^2\phi\right)$$

$$\dot{\theta} = S\left(r^2 - 1\right)\left(\cos\theta\sin\theta\cos\phi\sin\phi\right)/\left(1+r^2\right),$$

where r is the aspect ratio of the spheroid (>1 for prolate spheroids) and θ and ϕ are the polar and azimuthal angles in a spherical coordinate system (identical to that used in ref. 17), with ($\theta = \pi/2$, $\phi = 0$) representing the flow direction and ($\theta = \pi/2$, $\phi = \pi/2$) representing the direction of shear. The Jeffery equations predict rapid rotation when the

71

spheroid is aligned with the direction of shear and slow rotation when it is aligned with the flow direction.

The rotational diffusivity, D, was estimated using the Stokes-Einstein equation, $D = kT/F$, where F is the spheroid's torsional resistance, k is Boltzmann's constant, and T is temperature (20 °C). For a sphere of radius s, $F = 8\pi\mu s^3$, where μ is the dynamic viscosity of the fluid. For a spheroid, F is the torsional resistance in the direction perpendicular to its major axis (27),

$$F = \frac{16\pi\mu\left(b^2 + a^2\right)}{3\left(b^2\beta_0 + a^2\alpha_0\right)},$$

where a and b are the half-major and half-minor axes, α_0 and β_0 are given by

$$\alpha_0 = -\frac{2}{e^2 a} - \frac{1}{e^3}\ln\frac{a-e}{a+e} \quad \text{and} \quad \beta_0 = \frac{a}{e^2 b^2} + \frac{1}{2e^3}\ln\frac{a-e}{a+e},$$

and $e = \sqrt{a^2 - b^2}$ is the spheroid's eccentricity.

Optical scattering by a spheroid with arbitrary orientation with respect to the incident light was computed with the Extended Boundary Condition Method using the 'T-matrix' code (17) for spheroids with equivalent spherical diameter <10 μm, whereas for larger particles the Geometric Optics method (28) was used. The relative refractive index was assumed to be 1.05, appropriate for organic particles (14), and computations were performed for a wavelength of 550 nm. The direction of incident light was fixed at $\theta = \pi/2$, $\phi = 3\pi/2$. The T-matrix code (17) was used to compute the 4×4 scattering phase matrix, Z, of the spheroidal particle. For unpolarized incident light, the first element, Z_{11}, is the differential scattering cross section, $\frac{d\sigma}{d\Omega} = Z_{11}$, a measure of the angular distribution of scattered light (29), where $d\Omega = \sin\theta \, d\theta \, d\phi$ is the differential integration area in spherical coordinates. The total (σ_{tot}) and backward (σ_b) scattering cross sections of a particle with its long axis oriented along the direction (θ, ϕ) were calculated by integrating the differential cross section Z_{11} over all possible directions for σ_{tot} and over all backwards directions (with respect to the incoming light) for σ_b:

$$\sigma_{tot}(\theta,\phi) = \int_0^{2\pi}\int_0^{\pi}\frac{d\sigma}{d\Omega}\sin\theta d\theta d\phi$$

$$\sigma_b(\theta,\phi) = \int_0^{\pi}\int_0^{\pi}\frac{d\sigma}{d\Omega}\sin\theta d\theta d\phi.$$

The cumulative scattering coefficients produced by an assemblage of different species (i.e. different sizes and shapes), were computed by weighing the contribution of each species by its number density, N, as $b_b = \sum_{j=1}^{7} N_j \cdot (\bar{\sigma}_b)_j$, where subscript j refers to the j-th out of 7 species.

Characteristic timescale for alignment in shear. The angular velocity of a spheroid in a shear flow is given by $\dot{\phi} = -\dfrac{S}{r^2+1}\left(r^2 \sin^2 \phi + \cos^2 \phi\right)$ (26), where for simplicity we assumed the spheroid to be aligned with the shear plane, i.e. $\theta = \pi/2$ Integrating with respect to time, one obtains $\tan \phi = -\dfrac{1}{r}\tan\dfrac{rSt}{r^2+1}$. This describes Jeffery orbits, with period $2\pi(r^2+1)/(rS)$, and thus the characteristic timescale of alignment is $(r^2+1)/(rS)$.

References

1. Ryther JH (1956) Photosynthesis in the ocean as a function of light intensity. *Limnol Oceanogr* 1:61-70.
2. Bisset WP et al. (2001) Resolving the impacts and feedback of ocean optics on upper ocean ecology. *Oceanography* 14:30-53.
3. Field CB, Behrenfeld MJ, Randerson JT, Falkowski P (1998) Primary production of the biosphere: integrating terrestrial and oceanic components. *Science* 281:237-240.
4. Stramski D, Bricaus A, Morel A (2001) Modeling the inherent optical properties of the ocean based on the detailed composition of the planktonic community. *Appl Opt* 40:2929-2945.
5. Sathyendranath S, Cota G, Stuart V, Maass H, Platt T (2001) Remote sensing of phytoplankton pigments: a comparison of empirical and theoretical approaches. *Int J Remote Sensing* 22:249-273.
6. Stramski D, Kiefer D (1991) Light scattering by microorganisms in the open ocean. *Prog Oceanogr* 28:343-383.
7. Dall'Olmo G, Westberry TK, Behrenfeld MJ, Boss E, Slade WH (2009) Significant contribution of large particles to optical backscattering in the open ocean. *Biogeosci* 6:947–967.
8. Mobley CD, Stramski D (1997) Effects of microbial particles on oceanic optics: Methodology for radiative transfer modeling and example simulations. *Limnol Oceanogr* 42:550-560.
9. Jimenez J. (1997) Oceanic turbulence at millimeter scales. *In* C. Marrase, E. Saiz, & J. M. Redondo [eds.], Lectures on plankton and turbulence. *Sci Mar* 61:47–56.
10. Maxey MR, Corrsin S (1986) Gravitational settling of aerosol particles in randomly oriented cellular flow fields. *J Atm Sci* 11:1112-1134.
11. Von Karman T (1911) Über den Mechanismus des Widerstandes den ein

bewegter Körper in einer Flüssigkeit erfahrt. *Gott Nachr* 509-517.

12. Savas O (1985) On flow visualization using reflective flakes. *J Fluid Mech* 152:235-248.

13. Hu D, Mendel L, Goreau T, Chan B, Bush JWM (2005) Visualization of a fish with Tobacco Mosaic Virus. *Gallery of Fluid Motion, Phys Fluids* 17:091103-1.

14. Clavano WR, Boss E, Karp-Boss L (2007) Inherent optical properties of non-spherical marine-like particles - from theory to observation. *Oceanogr Mar Biol Ann Rev* 45:1-38.

15. Jonasz M (1991) Size, shape, composition, and structure of microparticles from light scattering. In *Principles, Methods, and Application of Particle Size Analysis,* J.P.M. Syvitski (ed.). (Cambridge University Press, Cambridge), pp 143–162.

16. Gordon HR (2006) Backscattering of light from disklike particles: is fine-scale structure or gross morphology more important? *Appl Opt* 45:7166–7173.

17. Mishchenko MI (2000) Calculation of the amplitude matrix for a nonspherical particle in a fixed orientation. *Appl Opt* 39:1026-1031.

18. Risken H (1989) *The Fokker-Planck Equation.* Berlin. Springer-Verlag.

19. Hill NA, Hader D-P (1997) A biased random walk model for the trajectories of swimming micro-organisms. *J. Theor. Biol.* 186:503-526

20. Bohren CF, Huffman DR (1983) *Absorption and Scattering of Light by Small Particles.* (Wiley, New York).

21. Frojmovic MM, Okagawa A, Mason SG (1975) Rheo-optical transients in erythrocyte suspensions. *Biochem Biophys Res Comm* 62:17-24.

22. Lazier JRN, Mann KH (1989) Turbulence and the diffusive layers around small organism. *Deep-Sea Res* 36:1721-1733.

23. Dekshenieks MM et al. (2001) Temporal and spatial occurrence of thin phytoplankton layers in relation to physical processes. *Mar Ecol Prog Ser* 223:61-71.

24. Ryan JP, McManus MA, Paduan JD, Chavez FP (2008) Phytoplankton thin layers caused by shear in frontal zones of a coastal upwelling system. *Mar Ecol Prog Ser* 354:21-34.

25. Marcos, Stocker R (2006) Microorganisms in vortices: a microfluidic setup. *Limnol Oceanogr Meth* 4:392-398.

26. Jeffery GB (1922) The motion of ellipsoid particles in a viscous fluid. *Proc R Soc A* 102:161-179.

27. Steinberger B, Petersen N, Petermann H, Weiss DG (1994) Movement of magnetic bacteria in time-varying magnetic fields. *J Fluid Mech* 272:189-211.

28. Macke A, Mishchenko MI (1996) Applicability of regular particle shapes in light scattering calculations for atmospheric ice particles. *Appl Opt* 35:4291-4303.

29. Mishchenko MI, Travis LD, Lacis AA (2002) *Scattering, Absorption, and Emission of Light by Small Particles* (Cambridge University Press, Cambridge).

30. Benton ER, Clark A Jr (1974) Spin-up. *Ann Rev Fluid Mech* 6:257-280.

74

AUTHOR CONTRIBUTIONS

ACKNOWLEDGEMENTS
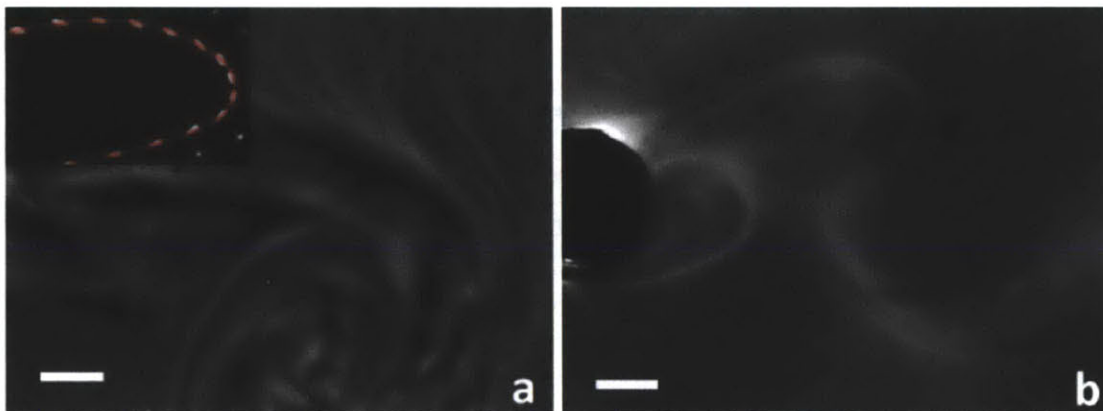
Fig. 1. Rheoscopic alignment produces optical patterns in microbial suspensions exposed to flow, revealing the underlying fluid motion. (*a*) A swirl induced by agitating a culture of *P. haloplanktis* bacteria. Such swirls provide microbiologists a means to rapidly assess cell density in cultures. *P. haloplanktis* has a 1:10 aspect ratio, including the flagellum. Bar = 3 mm. See also Movie S1. (Inset) Multiple-exposure image showing alignment of *P. haloplanktis* with a streamline (in red) within a microfluidic vortex (25). The cell body is approximately 1×2 μm. (*b*) A von Karman vortex street behind a cylinder towed through a suspension of *P. haloplanktis*. Bar = 3 mm.
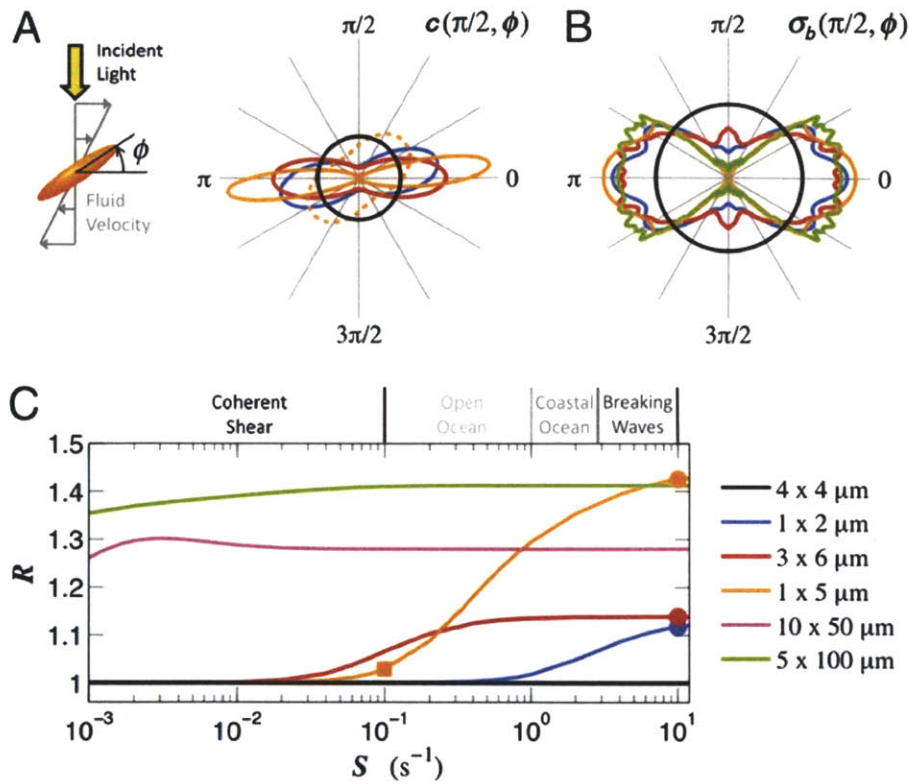
Fig. 2. A coupled fluid mechanics/optics model reveals that flow can significantly affect the inherent optical properties of the ocean. (*a*) Shear tends to align cells in the direction of flow. The probability distribution of particle orientation, $c(\pi/2,\phi)$ shows that alignment increases when cells are either larger or more elongated (see panel *c* for legend). The flow is along $\phi = 0$, the shear is along $\phi = \pi/2$. Dashed lines show results for $S = 0.1$ s^{-1} (square in panel *c*), solid lines are results for $S = 10$ s^{-1} (circles in panel *c*). The black line shows the case of a spherical particle (for any value of S). (*b*) Backscattering cross-section as a function of particle orientation, $\sigma_b(\pi/2,\phi)$. Incident light originates from $\phi = \pi/2$. Profiles are normalized such that they have equal area. (*c*) Flow increases optical backscattering for typical marine microorganisms. R is the mean backscattering cross-section of particles in a flow with shear rate S, normalized by the same quantity computed for $S = 0$ (for which particles assume random orientation). The departure of R from 1 results from the coupling of shear-induced alignment with the flow (panel *a*) and the orientation-dependence of scattering (panel *b*). The magnitude of this effect (i.e. $R-1$) depends on cell size, aspect ratio and shear rate. Typical shear rates are shown above the panel for the case of coherent flows (in black) and turbulent flows (in tones of grey).

76
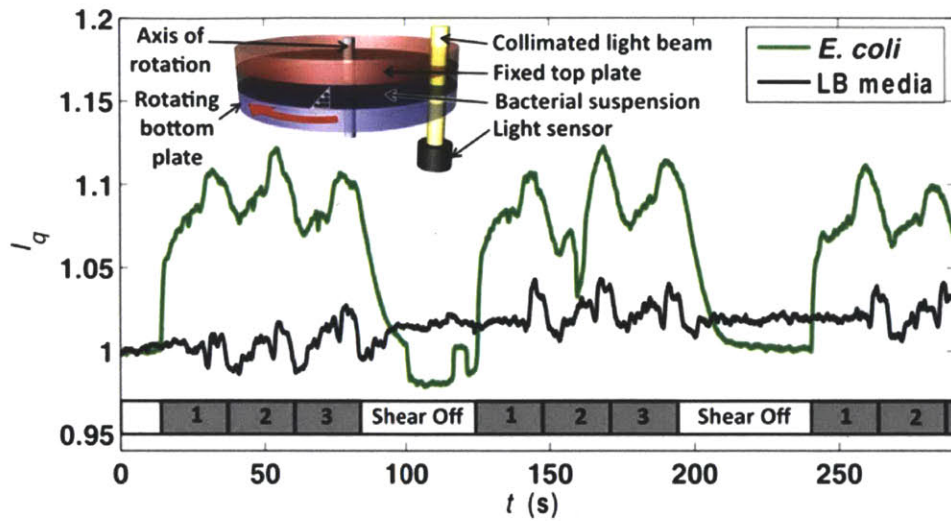
Fig. 3. Shear alters the transmission of light through microbial suspensions. **Inset**, A collimated light beam was passed through a suspension of *E. coli* bacteria in LB medium, sandwiched between two parallel plates. The top plate (red) was held stationary while the bottom plate was rotated at a constant rate for three revolutions, inducing shear within the fluid. **Main Panel**, The time series of normalized transmitted light intensity, I_q (see Methods). Transmittance increases when shear in the *E. coli* suspension is initiated (green line) and decays when the shear is turned off. The asymmetry between the rapid ramp up in I_q (~1-5 s) and the slower decay (~10-20 s) is in line with the known asymmetry in the spin-up versus spin-down times of fluid in cylindrical containers (30). Each gray segment indicates one revolution of the bottom plate. Controls performed is LB medium alone (black line) produce no appreciable difference in transmittance. Experimental noise in the calculation of I_q was ~0.03.
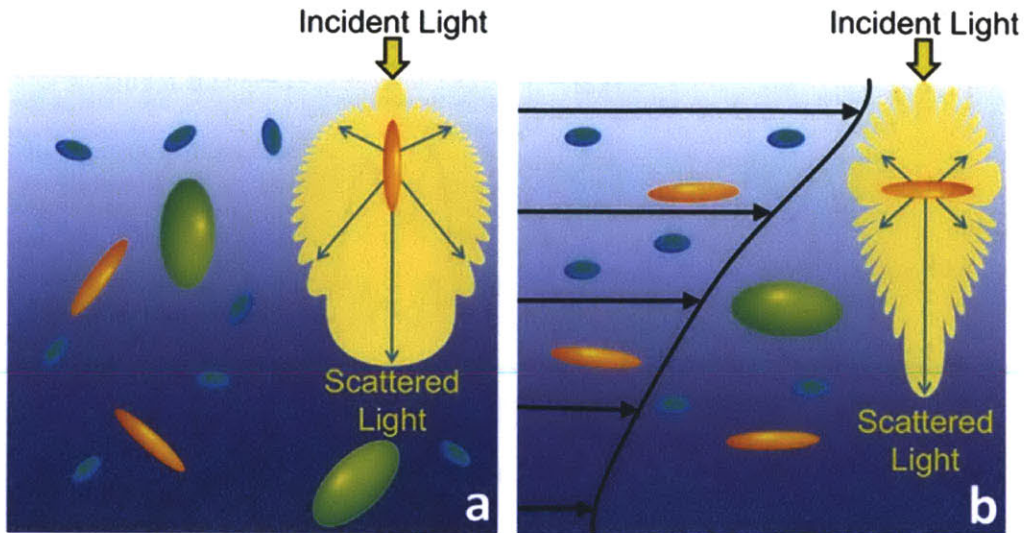
Fig. 4. Flow organizes the orientation of elongated microbes, thereby changing the fluid's bulk optical properties. (*a*) In quiescent conditions microbes are randomly oriented. (*b*) In a shear flow elongated organisms become preferentially aligned with the flow. Because optical scattering is strongly dependent on particle orientation, as shown by the two scattering profiles (panels *a* and *b*, in yellow), this preferential alignment can impact the inherent optical properties of seawater.

PART TWO:

Thin Phytoplankton Layers: Characteristics, Mechanisms, and Consequences

William M. Durham and Roman Stocker

Ralph M. Parsons Laboratory, Department of Civil and Environmental Engineering, Massachusetts Institute of Technology, Cambridge, Massachusetts 02139; email: durham@mit.edu, romans@mit.edu

Abstract For over four decades, aggregations of phytoplankton known as thin layers have been observed to harbor large amounts of photosynthetic cells within narrow horizontal bands. Field observations have revealed complex linkages among thin phytoplankton layers, the physical environment, cell behavior, and higher trophic levels. Several mechanisms have been proposed to explain layer formation and persistence, in the face of the homogenizing effect of turbulent dispersion. The challenge ahead is to connect mechanistic hypotheses with field observations to gain better insight on the phenomena that shape layer dynamics. Only through a mechanistic understanding of the relevant biological and physical processes can we begin to predict the effect of thin layers on the ecology of phytoplankton and higher organisms.

1. INTRODUCTION

The distribution of phytoplankton in the ocean is highly heterogeneous, or patchy, over length scales ranging from thousands of kilometers down to a few centimeters. At large scales, heterogeneity is primarily driven by locally enhanced growth rates, favored by mesoscale processes such as nutrient upwelling and front formation (Lévy 2008). At the smallest scales, patchiness likely arises from interactions of plankton with small-scale chemical or hydrodynamic gradients (Waters et al. 2003, Gallager et al. 2004, Seymour et al. 2009, Durham et al. 2011). This pervasive heterogeneity can affect the mean abundance of both phytoplankton and their predators through their nonlinear interaction (Steele 1974) and may contribute to sustaining the high diversity of plankton (Hutchinson 1961) via habitat partitioning (Bracco et al. 2000).

A particularly dramatic form of patchiness occurs when large numbers of photosynthetic microorganisms are found within a small depth interval. These formations are known as thin phytoplankton layers and have received considerable attention by oceanographers and mathematical modelers, recently culminating in an intensive multi-investigator effort, known as the Layered Organization in the Coastal Ocean project, that took place in Monterey Bay, California during 2005 and 2006, and was reviewed in an editorial by Sullivan et al. (2010b). Thin layers are temporally coherent aggregations of

phytoplankton, typically several centimeters to a few meters thick and often extending for kilometers in the horizontal direction (Dekshenieks et al. 2001, Moline et al. 2010). They are widespread in the coastal ocean, with one study in Monterey Bay reporting thin layers occurring up to 87% of the time (Sullivan et al. 2010a). At times, multiple layers comprising distinct phytoplankton species can occupy different depths in the same water column (Rines et al. 2010).

In what was perhaps the first observation of thin phytoplankton layers (**Figure 1a**), Strickland (1968) noted that standard sampling techniques could lead to substantial errors in the measurement of both the depth-integrated chlorophyll abundance and the concentration of chlorophyll at a given depth. Indeed, traditional techniques for the enumeration of plankton, including nets and bottles, lack the spatial resolution to capture the strong, sharp peaks in cell concentration characteristic of thin layers, resulting in the thinnest phytoplankton peaks being smeared or missed altogether (Donaghay et al. 1992).
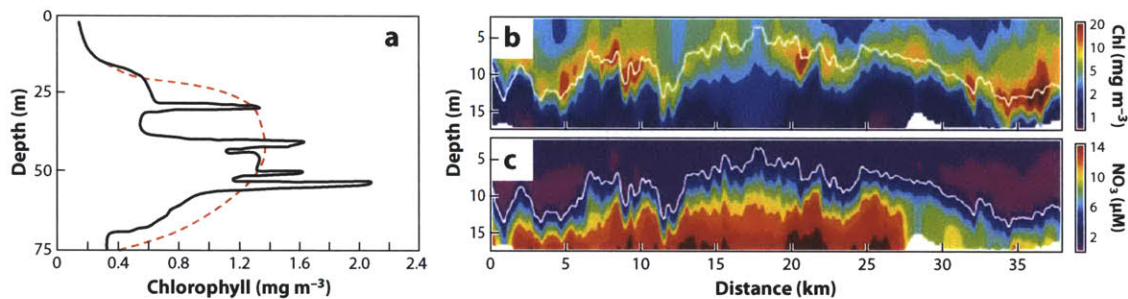
Figure 1 Technological advances over the past four decades have greatly improved our ability to characterize the spatial distribution of phytoplankton. (*a*) Thin layers observed in 1967 off La Jolla, California. The black line shows the continuous vertical chlorophyll concentration profile measured using a submersible pump and a ship-based fluorometer. The red dashed line shows the profile obtained using values from discrete depths, mimicking what would be obtained from bottle casts. This study revealed that the vertical distribution of phytoplankton often contains fine-scale spatial variability that eluded quantification by traditional sampling techniques. (*b*) Thin layers of chlorophyll, likely dominated by the flagellate *Akashiwo sanguinea*, observed at night in Monterey Bay using an autonomous underwater vehicle. (*c*) Concurrent measurements revealing that the upper portion of the water column was depleted of nitrate. Layers formed at night, as a result of downward vertical migration to the nutricline. Phytoplankton cells aggregated at the 3-μM nitrate isocline (*white line* in panels *b* and *c*).

Panel (*a*) was reproduced with permission from Strickland JDH, 1968, A comparison of profiles of nutrient and chlorophyll concentrations taken from discrete depths and by continuous recording. *Limnol. Oceanogr.* 13: 388-91. Copyright 1968 by the American Society of Limnology and Oceanography, Inc.

Panels (*b,c*) are reprinted with permission from Ryan JP, McManus MA, Sullivan JM, 2010, Interacting physical, chemical and biological forcing of phytoplankton

In the past 15 years we have seen a renaissance of thin layer observations, triggered by major advances in our ability to quantify thin layers of phytoplankton---and zooplankton, which prey on them---in situ. Examples include new techniques in optical sensing (Cowles et al. 1998, Twardowski et al. 1999), acoustic sensing (Holliday et al. 1998, Benoit-Bird et al. 2009, 2010), underwater imaging (Alldredge et al. 2002, Prairie et al. 2010), and airplane-based LIDAR (Churnside and Donaghay 2009). Observations of thin layers have now been made in many locations around the world, mostly in the coastal ocean, but also in the open ocean (Churnside & Donaghay 2009, Hodges & Fratantoni 2009). Simultaneously, a number of mechanisms have been put forward to explain the convergence of phytoplankton into thin layers. Here we review key findings from thin layer observations, describe proposed mechanisms of convergence and the methods used to decipher them in field observations, and discuss the ecological interactions of phytoplankton layers with higher trophic levels. We argue that the time is ripe for the next phase of thin layer research, focusing on the development of a quantitative, predictive framework for the processes that shape layer formation and on the formulation of new field and laboratory approaches to better understand their ecological repercussions.

2. CHARACTERISTICS OF THIN PHYTOPLANKTON LAYERS

2.1. How Are Thin Layers Different from Other Phytoplankton Aggregations?

Heterogeneity in the distribution of phytoplankton encompasses a wide range of spatial and temporal scales. How then are thin phytoplankton layers different from other phytoplankton aggregations? Thin layers are readily distinguished from deep chlorophyll maxima by their vertical extent: Deep chlorophyll maxima are typically tens of meters thick, with relatively weak vertical gradients in phytoplankton concentration (Cullen 1982), whereas thin layers have thicknesses of a fraction of a meter to a few meters, much stronger vertical concentration gradients (Dekshenieks et al. 2001), and can harbor phytoplankton concentrations much greater than the background (Section 2.5).

At the other end of the spectrum, thin layers differ from ephemeral centimeter-scale patches (Gallager et al. 2004, Mitchell et al. 2008, Waters et al. 2003) in both shape and persistence time. Thin layers are pancake shaped, have aspect ratios (horizontal to vertical extent) often in excess of 1,000 (Moline et al. 2010) and last hours to weeks (see Section 2.6), whereas small-scale patches have an aspect ratio closer to unity and lifetimes of minutes (Mitchell et al. 2008).

2.2. Criteria for the Identification of Thin Layers

The use of universal criteria to define which phytoplankton aggregations constitute thin layers can facilitate consistent comparisons among observations made at different times and locations by different researchers. A number of independent criteria have been developed, most of which share three requirements (Dekshenieks et al. 2001, Sullivan et al. 2010b): (*a*) The aggregation must be spatially and temporally persistent (e.g., readily identifiable in two subsequent vertical profiles); (*b*) the vertical extent of the aggregation must not exceed a threshold (e.g., 5 m); and (*c*) the maximum concentration must exceed a threshold (e.g., three times the background). Thresholds differ among studies and some studies use additional criteria. Experience has revealed that a single criterion cannot be applied to all thin layers, given the diversity of organisms, instrumentation, and environmental conditions (Sullivan et al. 2010b). However, when possible, there is significant value in using consistent criteria to identify layers.

2.3. Horizontal Extent of Thin Layers

Thin layers have traditionally been observed with vertical profiles of the water column and information on their horizontal extent is thus often in short supply (see Cheriton et al. 2010 for an overview of studies that measure horizontal layer dimensions). Moline et al. (2010) performed an extensive analysis of the spatial decorrelation scale of chlorophyll in Monterey Bay using data collected with two autonomous underwater vehicles and a ship-based system. The horizontal scale decreased dramatically over the course of a few years: In 2002 and 2003, the average layer length was ≈7 km, whereas in 2006 and 2008, it was just ≈1 km. This decrease was correlated with a shift in Monterey Bay's taxonomic composition, from nonmotile diatoms[1] to motile dinoflagellates, during the summer of 2004 (Jester et al. 2009, Rines et al. 2010). The relation between motility and horizontal layer extent remains largely unexplored.

Layers can be considerably larger in some environments. For example, Hodges & Fratantoni (2009) observed a thin layer off the continental shelf in the Philippine Sea that was >75 km long, while Nielsen et al. (1990) reported on a persistent, largely monospecific thin layer in the Kattegat/Skagerrak (the strait connecting the North and Baltic Seas) that extended for hundreds of kilometers.

2.4. Frequency of Occurrence of Thin Layers

The frequency of occurrence of thin layers varies greatly with geographical location and time of day. Dekshenieks et al. (2001) found thin layers in 54% of 120 profiles collected during three multi-day cruises in East Sound, Washington, and Steinbuck et al. (2010) found them in 21% of 456 profiles collected over two weeks in the Gulf of Aqaba (Red Sea). Benoit-Bird et al. (2009) observed strong diel variation: out of 632 profiles collected over a three-week period in Monterey Bay, thin layers were found in only 2% of the profiles acquired during the daytime but in 29% of those collected at night.

---

[1] Although some diatoms can glide along surfaces, they are largely incapable of motility in the water column and will thus be considered nonmotile for the purposes of this review.

82

Using 80,000 km of airplane-based LIDAR measurements, Churnside & Donaghay (2009) found thin layers to be relatively common in some regions. Off the Oregon and Washington coasts, they occurred 19% (during the daytime) and 6% (at night) of the time, over a 9 day period. In contrast, near Kodiak Island, Alaska, thin layers were found only 1.6% (during the daytime) and 0.2% (at night) of the time, during a three-week period. These results come with some caveats, as LIDAR does not detect layers beyond a certain depth ($\approx$20 m) and, more importantly, cannot discriminate among phytoplankton, zooplankton, and other particles (Churnside & Donaghay 2009).

The variability in the frequency of occurrence can be large even in a single location. For example, analysis of data from Monterey Bay revealed thin phytoplankton layers 87%, 56%, and 21% of the time over 1–3 week sampling periods in 2002, 2005, and 2006, respectively (Sullivan et al. 2010a). As suggested above, these changes might have been driven by a shift in the community composition.

2.5. Concentration Enhancement and Depth-Integrated Phytoplankton Fraction

Two metrics are often used to quantify the intensity of a thin layer: (*a*) the maximum phytoplankton concentration within the layer, relative to the background, and (*b*) the fraction of phytoplankton contained within the layer, relative to the total amount in the water column. In terms of the first metric, peak phytoplankton concentrations within a thin layer can be nearly two orders of magnitude larger than the background. For example, Ryan et al. (2008) reported a maximum chlorophyll concentration that was 55 times above the background. More typically, peak concentrations are several times that of the background (McManus et al. 2003, Sullivan et al. 2010a). This metric is directly relevant to processes that rely on encounter rates, such as the formation and subsequent settling of aggregates, sexual reproduction, and cell-cell communication, all of which to the first order scale with the square of cell concentration. In terms of the second metric, observations have revealed that a substantial fraction of the phytoplankton in the water column can reside within a thin layer. For example, Sullivan et al. (2010a) found that, based on chlorophyll concentrations, this fraction ranged from 33% to 47% in Monterey Bay.

2.6. Persistence Time of Thin Layers

Thin layers persist for periods ranging from hours to weeks. Layers detected at night in the nutricline in Monterey Bay lasted only a few hours (Sullivan et al. 2010a), whereas pycnocline-associated layers in East Sound lasted for days (Menden-Deuer & Fredrickson 2010) and layers in the Kattegat/Skagerrak persisted for weeks (Bjornsen & Nielsen 1991, Nielsen et al. 1990). However, tracking a thin layer from its formation to its demise is challenging because of the extensive sampling effort required and the advection of the layer by the ambient flow. Thus layer persistence time remains difficult to measure, hindering quantitative comparisons with mathematical predictions (see Section 3).

2.7. Correlation with Stratification and Shear

The depths at which thin layers occur are frequently correlated with strong gradients in fluid density (stratification) and vertical shear, both of which tend to occur at the bottom of the mixed layer (Johnston & Rudnick 2009).

Stratification plays a dual role in layer formation. First, it can produce layers because sinking cells often reach neutral buoyancy at a pycnocline, where they accumulate (see Section 3.3). Second, stratification stifles vertical turbulent dispersion, favoring layer formation by other mechanisms (see Section 3). The importance of stratification is supported by the observation that thin layers are often correlated with thermoclines (Steinbuck et al. 2009) or haloclines (Rines et al. 2002). For instance, Dekshenieks et al. (2001) found that 71% of the thin layers they observed in East Sound in 1996 were associated with a pycnocline.

Layers often occur where the horizontal velocity sharply changes direction over depth, and some mechanisms invoke shear as a means of layer formation (see Sections 3.1 and 3.4). Ryan et al. (2008) found that 92% of the thin layers they recorded in Monterey Bay in 2003 were associated with peaks in shear, with a mean shear rate of $S \approx 0.02$ s^{-1}. Dekshenieks et al. (2001) reported that thin layers in East Sound were thinnest during spring tides, when shear was enhanced within layers ($S = 0.003$--0.09 s^{-1} for all layers). Cheriton et al. (2009) found that the shear rate within a thin layer in Monterey Bay oscillated about a mean value of $S \approx 0.07$ s^{-1} over an 8.5-h period, at times exceeding 0.1 s^{-1}. Layers can occur at different positions relative to the peak in shear: Ryan et al. (2008) found the maximum shear in the middle of layers, whereas Sullivan et al. (2010a) observed shear to peak 1--2 m above the layers. A note of caution is in order when interpreting shear rates because in several cases these are obtained with acoustic Doppler current profilers, which can systematically underestimate shear maxima owing to coarse (meter-scale) sampling resolutions (Cowles 2004).

Shear is a double-edged sword for thin layers: it can favor layer formation via straining (see Section 3.1) or gyrotactic trapping (see Section 3.4), but it can also trigger hydrodynamic instabilities and turbulence that dissipate layers. These instabilities are resisted by stratification and the net stability of the water column is determined by the gradient Richardson number, $Ri = N^2 / S^2$, which measures the relative importance of stratification and shear: When $Ri < 1/4$, the water column is expected to be unstable (Kundu & Cohen 2004). This prediction is corroborated by observations in East Sound that found no layers when $Ri < 0.23$ (Dekshenieks et al. 2001), likely because of dissipation due to turbulence.

2.8. Phytoplankton Motility

Approximately 90% of the phytoplankton species known to form harmful algal blooms (HABs) can actively swim (Smayda 1997). Vertical migration allows cells to shuttle to depth at night, where limiting nutrients are abundant and predation risks reduced (Bollens et al. 2011), and to reside in the well-lit surface waters during the day (Ryan et al. 2010, Sullivan et al. 2010a). Many thin layers are composed of motile cells (Bjornsen

& Nielsen 1991, Koukaras & Nikolaidis 2004, Nielsen et al. 1990, Steinbuck et al. 2009, Sullivan et al. 2010a, Townsend et al. 2005, Tyler & Seliger 1978), although thin layers of nonmotile species, such as diatoms, are also frequent (Alldredge et al. 2002, Stacey et al. 2007, Sullivan et al. 2010a). However, a comprehensive knowledge of the role that motility plays in layer formation is still lacking, partly because the species composition of many layers remains undetermined.

The overwhelming majority of motile phytoplankton species are eukaryotic and swim by propagating bending waves along their flexible flagella (Guasto et al. 2012). The arrangement and kinematics of the flagella are diverse: Some green algae beat two nearly identical flagella in a breaststroke motion (Polin et al. 2009), whereas most dinoflagellates wave two dissimilar flagella in combination for propulsion and steering (Fenchel 2001). For some species, the mechanism of propulsion remains unknown, as in *Synechococcus*, which lacks flagella (Brahamsha 1999, McCarren & Brahamsha 2009). Swimming velocities of phytoplankton vary widely: The motile clade of *Synechococcus* ($\approx$1-μm diameter) swims at up to $w_s \approx 25$ μm s^{-1} (Waterbury et al. 1985), whereas larger eukaryotic cells (tens of micrometers in diameter) can swim at $w_s = 100$--500 μm s^{-1} (Fauchot et al. 2005, Kamykowski et al. 1992, Sullivan et al. 2010a). Care should be taken when interpreting swimming velocities, as they are often measured along the cell trajectory. The net migration speed (e.g. the vertical projection of the swimming velocity can be considerably smaller because of randomness in the swimming direction (Hill & Häder 1997) or the influence of turbulent shear (Durham et al. 2011).

2.9. Thin Layers of Toxic Species

Thin layers are often trophic hotspots, correlated with high abundance of bacteria, zooplankton, and fish (Benoit-Bird et al. 2009, 2010; McManus et al. 2003, 2008) (see Section 5). In contrast, some thin layers composed of toxic phytoplankton exhibit lower zooplankton concentrations than the surrounding waters (Bjornsen & Nielsen 1991, Nielsen et al. 1990), suggesting that aggregation into layers provides a selective advantage by offering a refuge from predation. Many toxic species have been observed to form thin layers, including *Pseudo-nitzschia australis* (McManus et al. 2008), *Chrysochromulina polylepis* (Nielsen et al. 1990), *Gyrodinium aureolum* (Bjornsen & Nielsen 1991), *Dinophysis* spp. (Koukaras & Nikolaidis 2004), *A. fundyense* (Townsend et al. 2005), and *Prorocentrum minimum* (Tyler & Seliger 1978).

Whereas some zooplankters suffer deleterious effects, including death, from toxic phytoplankton and avoid aggregations of toxic species, others predate on them seemingly with impunity (Nielsen et al. 1990, Turner & Tester 1997). These immune zooplankters might substantially increase their foraging rate within a thin layer, compared to when they are exposed to a homogeneous prey distribution, and thereby enhance the transfer of toxins up the marine food web. Thus, toxic species might pose a greater risk to higher trophic levels, such as marine mammals and seabirds, when they are concentrated in a thin layer (McManus et al. 2008).

Toxic thin layers are believed to play an important role in the instigation of HABs (Donaghay & Osborn 1997, Gentien et al. 2005, McManus et al. 2008, Sellner et al.

2003). Because large quantities of cells can be harbored meters beneath the surface, thin layers pose a challenge for the detection of subsurface blooms that might later spread to the entire water column. Monitoring programs relying on surface sampling or coarse sampling over depth might miss a thin layer, offering little warning time, for example, to alert fishery managers (McManus et al. 2008). Although many factors contribute to HABs (Smayda 1997), accounting for thin layer dynamics in existing HAB models (after Franks 1997) may hold the key to improving our ability to both understand and predict these events (Donaghay & Osborn 1997).

Tyler & Seliger (1978) found that in Chesapeake Bay, thin layers play a crucial role in annual blooms of the toxic dinoflagellate *P. minimum*, a species responsible for shellfish poisoning in humans (Heil et al. 2005). Every year, a population of *P. minimum* near the bay's mouth forms a thin layer, which is transported by density currents over 200 km upstream into shallower waters. During the journey the layers receive little light at depth, which limits growth. As layers reach shallower depths and light becomes abundant, a large bloom occurs. This surface bloom is eventually transported back to the mouth of the bay, forming the basis of the following year's bloom. Sellner et al. (2003) conjectured that a similar seeding process is responsible for *Dinophysis* blooms along the coasts of Spain and Sweden and for *Karenia mikimotoi* blooms in the English Channel.

Toxic thin layers do not have to instigate a surface bloom to profoundly affect the marine ecosystem. Perhaps the most striking example of the destructive potential of a thin layer is the pycnocline-associated layer of the toxic flagellate *C. polylepis* that formed in 1988 over 75,000 km² of the Skagerrak and Kattegat, which killed ≈10 million euros worth of farmed fish and ravaged the natural pelagic and benthic communities (Gjosaeter et al. 2000). The mortality of some pelagic organisms, such as codfish, was very high during the bloom, but the most dramatic repercussions of the thin layer occurred in the benthos, demonstrating the complex feedbacks in the marine ecosystem. Heavy mortality of sea stars and other predators greatly favored the mussel *Mytilus edulis*, which remained largely unaffected by the *Chrysochromulina* toxin and thus outcompeted other sessile organisms (cf. Paine 1966). Significantly increased numbers of mussel beds persisted for 2 years, until their predators rebounded and the sublittoral zone recovered. (Gjosaeter et al. 2000).

3. MECHANISMS OF LAYER FORMATION AND PERSISTENCE

Several mechanisms have been proposed to explain the formation and persistence of thin layers. Here we present and contrast these mechanisms as a basis for interpreting observations of thin layers in the field.

3.1. Straining of Phytoplankton Patches by Shear

Vertical gradients in horizontal velocity can transform horizontal gradients of scalars into vertical gradients. This occurs by differential advection, whereby portions of a patch at different depths are transported at different flow velocities, until the patch is transformed into a thin layer (**Figures 2a** and **3a,b**). This mechanism, proposed by Eckardt (1948) to

86

explain field observations of fine-scale vertical variability in temperature, was later extended to thin phytoplankton layers (Franks 1995, Osborn 1998). Here we summarize the spatial and temporal scales that characterize layer formation by straining, following the scaling analysis by Stacey et al. (2007) and the comprehensive treatment of Birch et al. (2008), who considered the straining of a two-dimensional Gaussian patch.
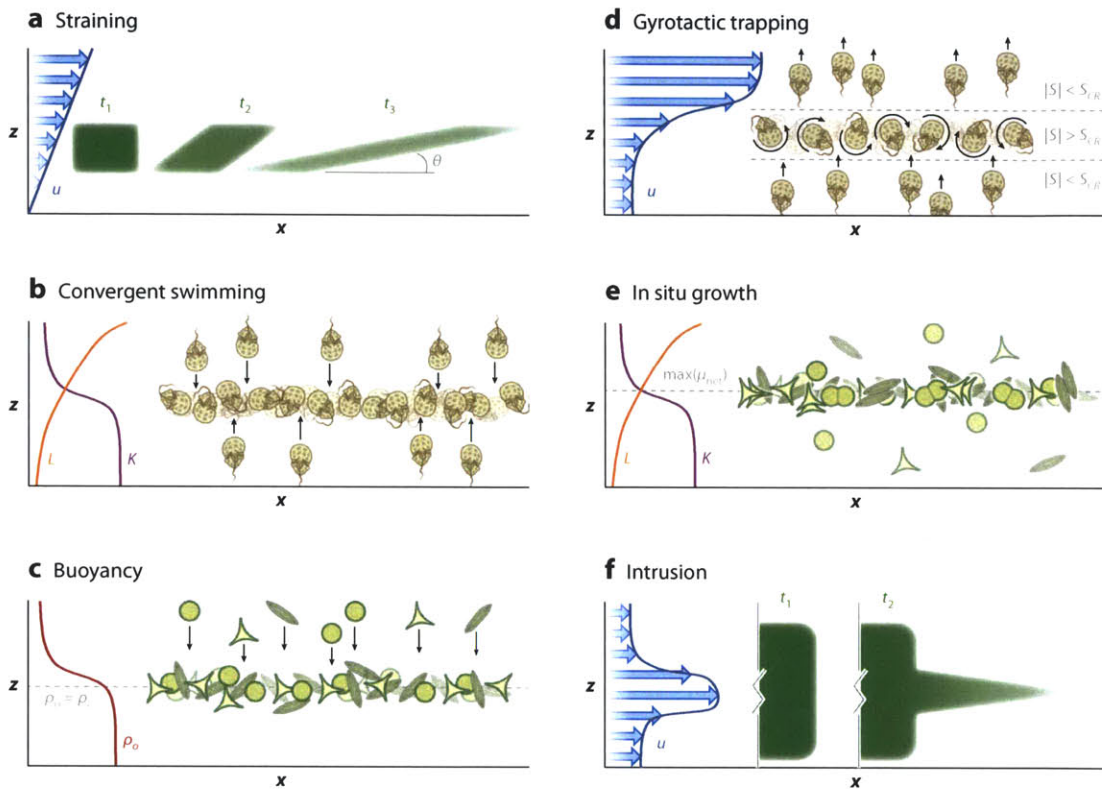
Figure 2 Diverse mechanisms can drive the formation of thin phytoplankton layers. (*a*) Straining transforms initial (time t_1) horizontal phytoplankton heterogeneity into a thin layer (t_3), by progressively tilting (t_2) a phytoplankton patch. This effect results from the differential advection of the patch over depth (see Section 3.1). (*b*) The accumulation of cells in layers can also result from directed motility, guided by cues that drive cells towards desirable conditions (e.g., a specific light intensity, *L*, or nutrient concentration, *K*; see Section 3.2). (*c*) Nonmotile cells whose density differs from that of the surrounding water sink (if heavier) or rise (if lighter) and accumulate at their depth of neutral buoyancy (dotted line), typically occurring at pycnoclines (see Section 3.3). (*d*) The vertical migration of motile phytoplankton can be suppressed in regions of high fluid shear, forming layers through gyrotactic trapping. As cells swim into a region where the magnitude of the shear rate, |*S*|, exceeds a threshold, S_{CR}, flow induces tumbling of the cells, trapping them at depth in the form of a thin layer (see Section 3.4). (*e*) Thin layers can also form when growth rates are enhanced at mid-depth. For example, this can occur when light intensity, *L*, and nutrient concentration, *K*, are both suitable for growth over a small depth interval (as shown here). The depth of maximal growth rate is denoted

by a dotted line (see Section 3.5). (*f*) Intrusions can form thin layers by transporting waters containing high phytoplankton concentrations into adjacent waters containing lower concentrations (see Section 3.6).
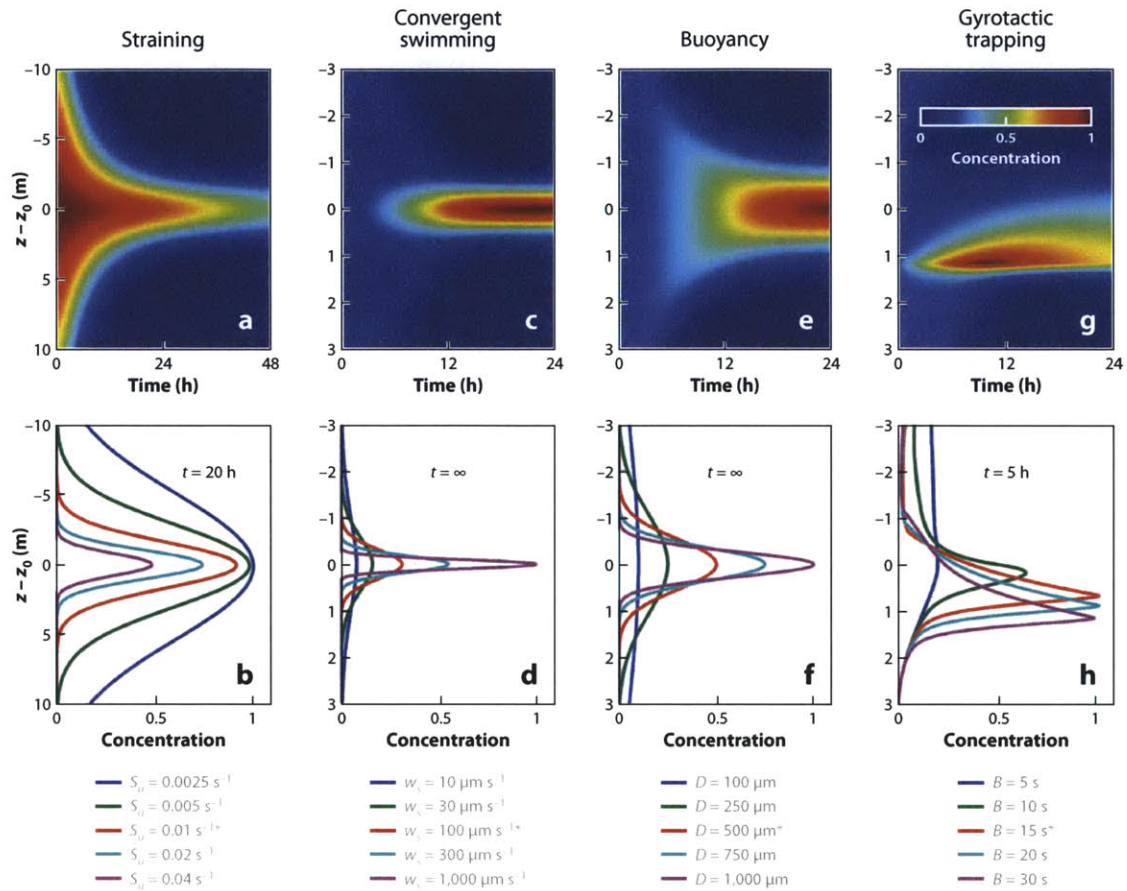
Figure 3 Thin layers generated via different convergence mechanisms exhibit distinctive characteristics. Using the mathematical models described in Section 3, we illustrate typical layer morphologies produced by four different convergence mechanisms. (*Lower panels*) Vertical profiles of phytoplankton concentration, $c(z)$, at a specific time t (or at steady state, denoted by $t = \infty$) for five different parameter values (indicated below each panel). (*Upper panels*) The spatiotemporal development of the layer for the value of the parameter marked with an asterisk. The color bar denotes cell concentration. All plots assume a vertical eddy diffusivity $\kappa_z = 10^{-5}\ \mathrm{m^2\ s^{-1}}$, and concentrations have been rescaled to a maximum of $c = 1$ in each case (taking advantage of the linearity of the advection-diffusion equation). (*a,b*) Layer formation via straining occurs when horizontal heterogeneity in a phytoplankton distribution is transformed into vertical heterogeneity. Straining cannot elevate phytoplankton concentrations above the maximum initial concentration. We assumed a Gaussian initial distribution centered at the origin, with standard deviations $L_o = 1$ km and $H_o = 10$ m; $u(z = 0) = 0$; a homogenous shear rate S_u; and $\kappa_x = 1\ \mathrm{m^2\ s^{-1}}$ (see Section 3.1). Shown are

88

concentrations at $x = 0$, where they are highest. (c,d) Convergent swimming $(\delta = 1$ m, $z_o = 0$, $P = 1$; see Section 3.2) assumes that cells above the layer swim downward and cells below the layer swim upward, yielding a steady balance between motility and turbulent dispersion. Faster swimming speeds w_s produce thinner layers. (e,f) Cell buoyancy $(N = 0.05$ s^{-1}, $v = 10^{-6}$ m^2 s^{-1}, $z_o = 0$, and $P = 1$; see Section 3.3) produces thin layers in a manner analogous to convergent swimming, albeit for nonmotile cells: Cells above their neutral buoyancy depth z_o sink, whereas those below it rise. A steady state is reached when buoyant convergence balances turbulent dispersion. Larger cells form thinner layers because the buoyancy velocity increases with size. (g,h) Gyrotactic trapping produces asymmetric layers (because swimming direction is asymmetric; here, upward) that do not attain a steady state because cells escape through one side (here, the top) of the layer by turbulent dispersion, which releases them from the trapped region. For the parameters used here $(\delta = 1$ m, $z_o = 0$, $u_o = 0.1$ m s^{-1}, and $w_{max} = 100$ µm s^{-1}; see Section 3.4) the maximum shear rate is $S = u_o/\delta = 0.1$ s^{-1}; therefore, layer formation occurs only for $B \sim> 10$ s. Results in panels c, e, g, h were produced via numerical integration, assuming an initially homogeneous concentration field $(c = 1$ for all z). Panels d and f show analytical expressions (Equations 2 and 3). Results in panels a and b were obtained via numerical integration of the two-dimensional advection-diffusion equation.

A phytoplankton patch in a vertically sheared flow will lengthen and, after a transient, become thinner (**Figures 2a** and **3a**). For simplicity, we consider that the shear rate du/dz – where $u(z)$ is the horizontal fluid velocity – is constant in time and uniform over depth and denote it by S_u. Then the horizontal extent of a patch with initial length L_o and

thickness H_o grows like $L(t) \sim \left[L_o^2 + \left(H_o S_u t \right)^2 \right]^{1/2}$. After a time $t_{shear} \sim L_o/(S_u\,H_o)$, the

upper portion of the patch has been transported horizontally past the lower portion. Up to this time, the layer thickness H_o remains unchanged, whereas for $t > t_{shear}$, the layer thickness measured across the mid-section of the strained patch decreases as $H(t) \sim L_o/(S_u\,t)$ (Birch et al. 2008, Stacey et al. 2007).

Typical values of vertical shear rates in the ocean are on the order of $S \sim 0.01$ s^{-1} (MacKinnon & Gregg, 2003), although values of $S \sim 0.1$ s^{-1} have been measured within thin layers (Cheriton et al. 2009, Dekshenieks et al. 2001), and larger shear rates might be revealed by sampling at higher vertical resolution (Cowles 2004). The size of phytoplankton patches before straining is highly variable, and we consider here a patch of initial size $H_o = 10$ m and $L_o = 1$ km as an example. When strained, a patch of these dimensions will begin decreasing in thickness after $t_{shear} \sim 3$ h for $S_u = 0.01$ s^{-1}. A distinctive characteristic of patches created by straining is their tilt across surfaces of constant density. Although small, this tilt has allowed the identification of patch straining as the mechanism responsible for the formation of some observed layers (Hodges & Fratantoni 2009, Prairie et al. 2010).

In the absence of turbulent dispersion, the thickness of a layer strained by fluid shear would monotonically approach zero, and the phytoplankton concentration in the layer

would remain unchanged (unlike the other mechanisms described in this section, straining cannot increase the local concentration of phytoplankton). However, turbulence acts to dissipate the layer, reducing peaks in phytoplankton concentration and increasing the layer thickness, thus placing a limitation on the lifetime and intensity of strained layers. Layers can form by way of this mechanism only if a patch is strained into a layer before turbulent dispersion mixes it away. In other words, dispersion must be weak compared to patch straining. In the ocean, turbulent dispersion is much larger in the horizontal (x) than in the vertical (z) direction, with typical eddy diffusivities on the order of $\kappa_x = 1$ m^2 s^{-1} and $\kappa_z = 10^{-5}$ m^2 s^{-1}. The relative importance of straining and turbulent dispersion is quantified by the horizontal and vertical Péclet numbers, $Pe_x = S_u H_o L_o / \kappa_x$ and $Pe_z = S_u H_o^3 / L_o \kappa_z$, defined as the ratio of the timescales for horizontal and vertical dispersion, L_o^2 / κ_x and H_o^2 / κ_z, respectively, to the straining timescale t_{shear}. For a thin layer to form before dissipating, it is necessary that $Pe_x \gg 1$ and $Pe_z \gg 1$ (Birch et al. 2008). For example, if $S_u = 0.01$ s^{-1}, $\kappa_x = 1$ m^2 s^{-1}, $\kappa_z = 10^{-5}$ m^2 s^{-1}, $H_o = 10$ m, and $L_o = 1$ km, then $Pe_x = 100$ and $Pe_z = 1,000$; hence conditions are conducive to layer formation by straining.

After a time $t = t_{shear}$, the layer begins thinning. The rate of thinning decreases with time (**Figure 3a**), until it equals the rate of layer thickening by vertical dispersion. The minimum thickness, $H_{min} \sim (\kappa_z L_o / S_u)^{1/3}$, is reached when vertical dispersion and straining balance, which occurs at time $t_{min} \sim \left(L_o^2 / \alpha^2 \kappa_z \right)^{1/3}$ (Birch et al. 2008, Stacey et al. 2007). At this time the layer's angle of tilt (**Figure 2a**) is $\theta \sim (\kappa_z / S_u L_o^2)^{1/3}$ (Stacey et al. 2007). For $t < t_{min}$, the layer thickness decreases as straining dominates over dispersion, whereas the opposite is true for $t > t_{min}$. For the values above, the patch reaches a minimum thickness of $H_{min} \sim 1$ m after $t_{min} \sim 1$ day.

Because straining does not actively concentrate cells, turbulent dispersion acts to monotonically reduce peak concentrations in the layer. For typical parameter ranges, the layer intensity---defined as the current maximum in cell concentration normalized by the maximum initial concentration---declines like $I(t) \sim [1 + 2(t/t_{min})^3]^{-1/2}$ (Birch et al. 2008). At $t = t_{min}$, the layer's maximum concentration is still ~60% of its initial concentration. After t_{min}, the concentration falls off rapidly: At $t = 4t_{min}$ (~4 days in the above example), it is only ~10% of the initial concentration. Eventually, vertical dispersion returns the layer thickness to its initial value, H_o, after a time H_o^2 / κ_z. By this time, however, the layer intensity is only marginally above background and of little ecological relevance (Birch et al. 2008).

3.2. Convergent Swimming

Many factors can contribute to the aggregation of cells at a particular depth by convergent swimming. There is evidence that gradients in nutrient concentration often act in concert with light cues. In laboratory experiments, MacIntyre et al. (1997) found that the HAB-forming dinoflagellate *Alexandrium tamarense* did not perform any vertical migration under uniformly nitrate-replete conditions. When nitrate was

exhausted in the upper portion of the water column, the population initiated a diel migration to the nutricline. The migration began just before dark, and phytoplankton swam back to the surface before sunrise, indicating that the migration was not driven purely by phototaxis. Field observations have confirmed this behavior: For example, *Akashiwo sanguinea* has been reported to initiate downward migration to the nutricline 5--6 h before sunset and to begin their upward journey 3--4 h before sunrise (Sullivan et al. 2010a). The onset of vertical migration before light becomes a cue is common to many species (e.g. Baek et al. 2009) and is likely driven by cell metabolism (Kamykowski & Yamazaki 1997). Furthermore, concentrated cells within thin layers might themselves affect light penetration, changing the light cues available to cells (Marcos et al. 2011, Sullivan et al. 2010a).

Some thin layers occur at depths corresponding to specific nutrient concentrations. Ryan et al. (2010) observed that *A. sanguinea* aggregated within a vertical gradient of nitrate in Monterey Bay. Chlorophyll peaks coincided with the depth of the 3-μM nitrate isocline, demonstrating that cells swam downward until they reached this concentration (**Figure 1b,c**). The half-saturation constant for nitrate uptake by this species is ≈ 1 μM (Kudela et al. 2010), suggesting that swimming deeper to higher nitrate concentrations might not have been justified by the small additional uptake. In the Gulf of Maine, Townsend et al. (2005) found that a thin layer of *Alexandrium fundyense* resided at a depth corresponding to a cumulative concentration of nitrate plus nitrite of 1 μM, while another fraction of the population was located near the surface. This bimodal distribution might have resulted from asynchronous vertical migrations within the population (Ralston et al. 2007). This explanation assumes that when all steps of the migration cycle (i.e. photosynthesizing near the surface, swimming to depth, absorbing nutrients, and swimming back to the surface) cannot be completed in 24 hours, the cells' migration pattern becomes desynchronized from the day/night cycle, leading to two peaks in cell abundance, one at the surface and one at depth, between which individuals shuttle (Ralston et al. 2007).

Gradients in salinity (haloclines) also attract motile phytoplankton. The toxic raphidophyte *Heterosigma akashiwo*, sometimes observed in thin layers (Grünbaum 2009), has been shown to aggregate at haloclines in laboratory water columns (Harvey & Menden-Deuer 2011). Natural phytoplankton assemblages also aggregate at haloclines in the laboratory, indicating that convergent swimming to salinity gradients might be widespread, although the fitness benefit of this behavior remains unknown (D. Grünbaum, personal communication).

Thin layer formation induced by an active swimming response (e.g., toward a preferred nutrient, salinity, or light level) is often modeled by assuming that cell motility is directed to a particular depth (**Figure 2b**). Stacey et al. (2007) proposed a simple model of convergent swimming, in which cells swim vertically toward a target depth z_o from both above and below that depth, at a constant speed w_s. If we denote by $W(z)$ the vertical swimming speed at depth z (with z and W positive downward), the behavior modeled by Stacey et al. (2007) corresponds to $W(z) = -w_s$ for $z > z_o$ and $W(z) = w_s$ for $z < z_o$. However, gradients in stimuli (e.g., nutrients, salinity, light) and the timescale over which cells respond to these stimuli are likely not as abrupt as this minimum-ingredient

model assumes (Sullivan et al. 2010a, Ryan et al. 2010). An additional degree of realism can be included in the model by assuming a reduction in the swimming speed as the target depth z_o is approached, to avoid a discontinuous change in swimming behavior at z_o. This was proposed by Birch et al. (2009), who considered the continuous velocity $W(z) = -w_s \tanh[(z - z_o)/\delta]$. In this formulation, cells swim toward the target depth z_o with a vertical velocity whose magnitude smoothly increases with distance from z_o, reaching a maximum speed of w_s at a vertical distance of order δ from the target depth. At the target depth, the swimming speed is zero; $W(z = z_o) = 0$. Although more realistic than the binary behavioral model of Stacey et al. (2007), this model requires the estimation of the length scale δ. The two models are equivalent in the limit $\delta \to 0$.

Unlike patch straining (see Section 3.1), thin layer formation via convergent swimming is inherently a one-dimensional process. The spatiotemporal evolution of the cell concentration, $c(z,t)$, can thus be predicted by the one-dimensional advection-diffusion equation

$$\frac{\partial c}{\partial t} + \frac{\partial (cW)}{\partial z} = \frac{\partial}{\partial z}\left(\kappa_z \frac{\partial c}{\partial z} \right), \quad (1)$$

where the second term on the left-hand side is the divergence of the cell flux that results from vertical swimming. Unlike straining, the vertical distribution of cells in a thin layer that forms by convergent swimming can reach a steady state, in which the flux of cells into the thin layer due to swimming balances the flux of cells out of the layer due to turbulent dispersion. Using Stacey et al.'s (2007) assumption of binary convergent swimming leads to the prediction that the steady-state layer thickness scales as $H_e \sim \kappa_z/w_s$. Convergent swimming can therefore produce layers that are very thin: Cells swimming at $w_s = 100$ μm s^{-1} in an environment with vertical eddy diffusivity $\kappa_z = 10^{-5}$ m^2 s^{-1} accumulate in a layer that is only $H_e \sim 10$ cm thick.

A reduction in swimming speed as cells approach the target depth z_o can increase layer thickness. Using their continuous swimming velocity profile, Birch et al. (2009) obtained the steady-state cell distribution

$$c_e(z) = \frac{P}{\delta} \frac{\cosh[(z - z_o)/\delta]^{-Pe_{swim}}}{\beta(\frac{1}{2}, \frac{1}{2} Pe_{swim})}, \quad (2)$$

where P is the depth-integrated phytoplankton concentration (cells per unit surface area of the ocean), and $Pe_{swim} = w_s \delta / \kappa_z$ is the motility Péclet number, based on the maximum vertical swimming speed w_s. The beta function $\beta(\frac{1}{2}, \frac{1}{2} Pe_{swim})$ decreases monotonically with increasing Pe_{swim}. If $Pe_{swim} \gg 1$ ($\ll 1$) the layer thickness is much smaller (greater) than δ. Thus, as predicted by the scaling above, $H_e \sim \kappa_z/w_s$, layer thickness decreases with faster swimming speeds (**Figure 3d**) and weaker vertical dispersion.

3.3. Buoyancy

Even nonmotile phytoplankton can actively control their vertical position in the water column by regulating their buoyancy (i.e., their density difference with the ambient water). A number of mechanisms are employed, including gas vacuoles (Walsby 1972), carbohydrate ballasting (Villareal & Carpenter 2003), and active replacement of ions in the internal sap (Gross & Zeuthen 1948). The density of marine phytoplankton typically lies in the range $\rho_p = 1.03$--1.20 g cm^{-3} for both motile and nonmotile species (Eppley et al. 1967, Van Ierland & Peperzak 1984, Kamykowski et al. 1992). While the settling velocity of motile cells can typically be neglected, as they swim much faster than they sink (Kamykowski et al. 1992), for nonmotile cells buoyancy represents an important means to move relative to the fluid. Similar to their motile counterparts, some nonmotile species also perform periodic vertical migrations by modulating their buoyancy. For example, the diatom *Rhizosolenia* completes a vertical migration cycle every 3--5 days (Richardson et al. 1998), and there is evidence that colonies of the nonmotile cyanobacterium *Trichodesmium* perform vertical migrations to great depths (potentially >100 m) on a daily basis (White et al. 2006).

Given phytoplankton's minute size ($\sim$1--1,000 μm) and small density contrast with seawater (typical seawater densities are $\rho_o = 1.02$--1.03 g cm^{-3}), their movement by buoyancy occurs at low Reynolds numbers. The Reynolds number, $Re = W_s D / v$, expresses the relative importance of inertial and viscous forces, where W_s is the vertical (settling or rising) speed relative to the fluid, D is a characteristic linear dimension of the cell, and v [$\approx 1 \times 10^{-6}$ m^2 s^{-1}] is the kinematic viscosity of seawater. W_s is determined by the balance of gravitational force, buoyancy, and drag. For a spherical cell at $Re \ll 1$, $W_s = \Delta\rho\, g\, D^2/(18\rho_o v)$, where $\Delta\rho = \rho_p - \rho_o$ and g is the gravitational acceleration (Clift et al. 1978). Phytoplankton cells thus sink or rise unless their density is the same as that of the ambient fluid.

Buoyancy can therefore drive layer formation in a stratified water column [i.e., $\rho_o = \rho_o(z)$, Alldredge et al. 2002], when phytoplankton sink or rise to their depth of neutral buoyancy, z_o (where $\Delta\rho = 0$) (**Figure 2c**). Assuming that the fluid density increases linearly with depth (i.e., dρ_o/dz is constant), the density difference between the cell and the fluid is $\Delta\rho = -\rho_o N^2(z - z_o)/g$, where $N^2 = (g/\rho_o)\,$dρ_o/dz. One can use this to rewrite the buoyancy velocity as a function of the distance $z - z_o$ of a cell from its neutral buoyancy depth; i.e., $W_s(z) = -N^2 D^2(z - z_o)/(18v)$ (Stacey et al. 2007).

The spatiotemporal distribution of cells is governed by the same advection-diffusion equation introduced for convergent swimming (Equation 1), with the velocity $W(z)$ replaced by the buoyancy velocity $W_s(z)$. We note that this formulation assumes that N is constant over the depth of the layer, which may not hold exactly in practice but can be often considered a good first approximation. A scaling analysis yields the characteristic steady-steady thickness, $H_e \sim [18v\kappa_z / (N^2 D^2)]^{1/2}$, of a phytoplankton layer formed under the influence of buoyancy and turbulent dispersion (Stacey et al. 2007). Birch et al. (2009) calculated the steady-state distribution of cells,

$$c_e(z) = P \sqrt{\frac{\gamma}{2\pi\kappa_z}} \exp\left(-\frac{\gamma(z-z_o)^2}{2\kappa_z}\right), \quad (3)$$

where P is the depth-integrated phytoplankton concentration and $\gamma = N^2 D^2 / 18\nu$. Thus steady-state profiles are Gaussian, with larger cells producing more compact layers (**Figure 3f**) owing to their higher vertical velocities. Solutions of the unsteady advection-diffusion equation reveal that for large cells, layer formation can occur within several hours (**Figure 3e**).

3.4. Gyrotactic Trapping

Thin layers are frequently found at depths at which the vertical shear is enhanced, in many cases corresponding to the location where the horizontal velocity changes direction (Dekshenieks et al. 2001, Cowles 2004, Ryan et al. 2008, Sullivan et al. 2010a). Vertical shear is often most pronounced at pycnoclines (Johnston & Rudnick 2009), where density stratification dampens turbulence and suppresses overturning instabilities. Durham et al. (2009) proposed that vertical gradients in shear trigger the formation of thin layers of motile phytoplankton by disrupting their vertical migration. To perform vertical migration, motile phytoplankton swim in a direction parallel to that of gravity, via a mechanism known as gravitaxis (or geotaxis). Multiple processes can result in gravitaxis (Kessler 1985, Lebert & Häder 1996, Roberts & Deacon 2002), but all generate a stabilizing torque on the cell that acts to keep its swimming direction oriented along the vertical. However, when there is ambient flow, shear exerts a viscous, destabilizing torque on the cell, which tends to make it rotate. The swimming direction is set by the balance of the gravitactic and the viscous torques, and the cell is said to be gyrotactic (Kessler 1985). The susceptibility of a cell to shear, i.e., how easily the cell is rotated away from its vertical equilibrium orientation, is measured by the gyrotactic reorientation parameter, B, the timescale required for a cell in a quiescent fluid to return to its equilibrium orientation after being perturbed. Cells with larger B are more susceptible to being reoriented by shear.

Durham et al. (2009) showed that thin layers form at depths where the shear rate, S, exceeds a critical value, $S_{CR} = B^{-1}$. There are two distinct regimes of gyrotaxis: an equilibrium regime and a tumbling regime. In the equilibrium regime, the local shear rate is lower than the critical shear rate $[|S(z)| < S_{CR}]$, and a cell can reach its equilibrium orientation, given by $\sin\theta = BS$, where θ is the angle between the swimming direction and the vertical direction. In the tumbling regime, the shear rate exceeds the threshold $[|S(z)| > S_{CR}]$: the maximum stabilizing torque due to gravity is not sufficient to balance the destabilizing torque due to shear, causing the cell to tumble end over end. A tumbling cell has no vertical movement, as it remains trapped at the depth at which $|S(z)| = S_{CR}$. B is known only for a handful of species (Drescher et al. 2009, Durham et al. 2009, Hill & Hader 1997, Kessler 1985) and we estimate that it generally falls in the range 1--100 s.

94

When vertically migrating phytoplankton encounter increasing levels of shear, the vertical projection of their swimming speed, W, progressively decreases (because $\sin\theta = BS$). When cells reach the depth at which $|S(z)| = S_{CR}$, their upward speed vanishes ($W = 0$), leading to a gradient in cell flux and thus an accumulation of cells (**Figure 2d**). Durham et al. (2009) demonstrated in a laboratory experiment that this mechanism, which they termed gyrotactic trapping, drives layer formation. Motile phytoplankton were injected into a flow whose shear rate increased linearly with height. Using video microscopy, they detected intense thin layers at mid-depth in the device, for both the green alga *Chlamydomonas nivalis* and the toxic raphidophyte *H. akashiwo*. These observations were supported by tracking individual cells, which revealed the transition from the equilibrium regime to the tumbling regime, at a depth corresponding to S_{CR}. An individual-based numerical model successfully reproduced the salient features of the observations.

Similar to convergent swimming and buoyancy, gyrotactic trapping can be modeled with a one-dimensional advection-diffusion equation (Durham et al. 2009). To model the peak in shear often associated with thin phytoplankton layers, a representative fluid velocity profile $u(z) = -u_o\tanh[(z - z_o)/\delta]$ was used, in which the horizontal flow velocity $u(z)$ varies smoothly from u_o to $-u_o$ over a vertical distance on the order of δ. The corresponding shear rate is $S(z) = du/dz = -(u_o/\delta)\mathrm{sech}^2[(z - z_o)/\delta]$, where z_o is the depth of zero fluid velocity and maximum shear. Combining this expression for $S(z)$ with the equilibrium orientation $\sin\theta = BS$ yields the vertical projection of the swimming speed, $W(z) = -w_{max}\{1 - \Psi^2\,\mathrm{sech}^4[(z - z_o)/\delta]\}^{1/2}$, where w_{max} is the vertical swimming speed when $S = 0$ and $\Psi = Bu_o/\delta$ is the plankton stability number. For depths z at which $|S(z)| > S_{CR}$ (tumbling regime), $W(z) = 0$ (Durham et al. 2009). The advection-diffusion equation for gyrotactic trapping is the same as that for convergent swimming and buoyancy (Equation 1), except that the vertical velocity is replaced by the expression for $W(z)$ derived here.

Turbulent dispersion acts to broaden the layer thickness as with the previous cases. The layer dynamics are governed by two dimensionless parameters: the plankton stability number, Ψ, and the gyrotactic Péclet number, $Pe_{gyro} = w_{max}\delta/\kappa_z$. A first criterion for layer formation is $\Psi \sim> 1$; i.e., the shear rate must be large enough to stifle vertical migration. A second criterion is $Pe_{gyro} > 1$: Motility must bring cells into the region of enhanced shear faster than turbulent dispersion transports them through it.

Cells trapped in a high-shear region will eventually escape from the layer via turbulent dispersion. Once clear of the region where $|S(z)| > S_{CR}$, previously trapped cells can resume upward migration. Thus, similar to patch straining, thin layers produced via gyrotactic trapping are inherently transient: No steady-state distribution is attained because the supply of phytoplankton swimming into the layer is finite, and turbulent dispersion makes the layer leaky. The diel cycle of phytoplankton motility, the magnitude of turbulent dispersion and the temporal coherence and vertical extent of the region of enhanced shear all likely affect the lifetime of a layer produced by this mechanism. Modeling suggests that layers produced via gyrotactic trapping could persist for more than 12 hours (**Figure 3g**).

Unlike patch straining, convergent swimming, and buoyancy---all of which generate layers that are symmetric about the depth of maximum concentration when the eddy diffusivity is constant over depth ---gyrotactic trapping produces layers that are inherently asymmetric. The side of the layer where cells swim into the region of enhanced shear (the lower side in **Figure 3g,h**) features a considerably steeper gradient in cell concentration (larger $|dc/dz|$) than the opposite side. Furthermore, this mechanism predicts that species with different B will aggregate into spatially distinct layers, each corresponding to the depth of that species' critical shear rate (**Figure 3h**).

3.5. In Situ Growth

Layer formation via *in situ* growth can occur when growth is most vigorous at mid-depth, for example when growth is either light- or nutrient-limited except over a small depth interval (**Fig. 2e**) or when nutrients are abundant only at mid-depth (see Section 3.6). Consisent with the latter scenario, Birch et al. (2008) gave a detailed analysis of phytoplankton growth within a nutrient patch strained by shear, finding that the resulting layer dynamics largely follow the scalings for a phytoplankton patch in shear (see Section 3.1).

Growth is typically modeled using the differential equation $dc/dt = \mu_{net}\, c$, where μ_{net} is the net growth rate (growth minus mortality), yielding an exponential increase in phytoplankton or chlorophyll concentration over time. For the purpose of comparing with observations, this differential growth model is often approximated as $\Delta c = \mu_{net}c_0\Delta t$, where c_0 is the initial concentration and Δt the elapsed time (Steinbuck et al. 2010). Typical growth rates of phytoplankton range from $\mu = 0.4\ \mathrm{d}^{-1}$ in polar habitats to $\mu = 0.7\ \mathrm{d}^{-1}$ in tropical habitats, whereas grazing-induced mortality rates ranges from $r = 0.2\ \mathrm{d}^{-1}$ to $r = 0.5\ \mathrm{d}^{-1}$ in the same regions, respectively (Calbet & Landry, 2004).

3.6. Intrusions

Intrusions can generate layers through the lateral transport of phytoplankton- or nutrient-rich waters into adjacent waters: The former produces thin layers directly (**Figure 2f**), whereas the latter produces layers by locally enhancing growth rates at mid-depth (see Section 3.5). Although several mechanisms can trigger intrusions, we focus on two general types of intrusion that have been implicated in layer formation: gravity-driven flows by salt wedge dynamics in estuaries (Kasai et al. 2010) and boundary mixing (Armi 1978, Phillips et al. 1986).

Estuaries often harbor phytoplankton blooms that result from the mixing of saltwater, containing nutrient-limited marine phytoplankton, with nutrient-replete freshwater (Nixon, 1995). In salt-wedge estuaries, the boundary between fresh riverine waters and the salty marine waters intruding beneath them is especially sharp, because stratification suppresses vertical mixing. This boundary, where marine species mix with nutrient-rich waters (*e.g.* containing high nitrogen concentrations), often harbor thin layers, such as those observed in the Yura Estuary in Japan (Kasai et al. 2010). Two mechanisms are believed to have contributed to the formation of these layers: the upstream transport of phytoplankton-rich waters by the salt wedge intrusion and the diffusion of nutrient-rich

96

freshwater through the interface between freshwater and saline water, which fuels growth (Kasai et al. 2010). The latter mechanism was supported by the observation that phytoplankton concentrations in the layer were higher than at the estuary's mouth, where the phytoplankton-rich water originated.

A second type of intrusion occurs when mixing along land boundaries interacts with stratification to drive offshore flows at the pycnocline (Armi 1978, Phillips et al. 1986). Several processes can induce boundary mixing, including breaking internal waves on sloping shores (McPhee-Shaw 2006), flow around islands (Simpson et al. 1982), and topographically influenced fronts (Pedersen 1994). The latter two have been observed to trigger layer formation by locally bolstering growth at mid-depth. In the first case, mixing induced by flow about the Scilly Isles in the Celtic Sea was observed to drive nitrate-rich waters from the deep sea into the well-lit pycnocline, producing layers composed of motile cells whose chlorophyll concentration was more than 15 times larger than ambient (Simpson et al. 1982). In the second case, a tidal front that occurred over Dogger's Bank in the North Sea interacted with the sloping bottom to drive a horizontal intrusion of water from the deeper depths into the thermocline. The resulting phytoplankton layers contained chlorophyll concentrations up to 20-fold larger than ambient (Pedersen 1994).

Boundary mixing has also been implicated in the direct formation of thin layers via offshore-directed intrusions of phytoplankton-rich waters. This mechanism was proposed by Steinbuck et al. (2010) to explain the formation of layers in the Gulf of Aqaba. Large intrusions are affected by hydrodynamic instabilities induced by Earth's rotation, which produce horizontal mixing with a dispersion coefficient $\kappa_{in} \approx 0.13 \ g'h/f$ (Ivey 1987), where h is the intrusion thickness, f is the Coriolis parameter, $g' = 0.07g(\rho_2 - \rho_1)/\rho_1$, and ρ_1 and ρ_2 are the water densities above and below the intrusion, respectively. With this formulation, Steinbuck et al. (2010) estimated the time,

$t_{in} \approx L_{in}^2 / (2\kappa_{in})$ (Fischer et al. 1979), required for an intrusion to propagate a distance L_{in}, finding good agreement with their observations. As the tongue of intruding water advances, vertical turbulent dispersion homogenizes it with the surrounding water, and the layer thickness increases as $H' \approx (2\kappa_z t_{in})^{1/2}$ (Fischer et al. 1979). These observations are discussed in more detail in Section 4.

3.7. Differential Grazing

Some zooplankton predators exhibit reduced grazing rates in regions that contain toxic or otherwise unpalatable species (Turner & Tester 1997), sometimes avoiding those species altogether (Bjornsen & Nielsen 1991, Nielsen et al. 1990). The prominence of a thin layer containing such phytoplankton species might be dramatically enhanced when zooplankton graze on other species above and below the layer. Although this mechanism does not per se create a thin layer, as species benefitting from reduced predation must first form a layer by another mechanism, differential grazing can increase a layer's chlorophyll signal relative to the surrounding waters, making layers of certain species detectable as surrounding species are consumed.

3.8. A Cautionary Note About Turbulent Dispersion

A note is in order regarding the role of turbulence, as it has been repeatedly suggested that vertical gradients in eddy diffusivity cause phytoplankton layers, by the accumulation of cells at depths where diffusivity is low (e.g., pycnoclines; see Visser 1997 for examples). This proposition is based on an incorrect implementation of individual-based models. Properly formulated models, as well as solutions of the diffusion equation, demonstrate that---in the absence of a process that transports cells relative to the fluid (e.g., motility, buoyancy)---randomly distributed cells cannot form aggregations, even if turbulent dispersion is spatially variable (Ross & Sharples 2004, Visser 1997).

## 4. DEDUCING MECHANISMS OF LAYER FORMATION FROM FIELD OBSERVATIONS

Quantitative understanding of the physical and biological processes that mediate layer formation holds great promise for guiding field observations and for developing mathematical models to predict the occurrence and ecologically relevant characteristics of thin layers. In this section, we draw on the results of Section 3 to review recent reports of thin phytoplankton layers that applied quantitative methods to probe the mechanisms responsible for layer formation. The melding of theory and field observations pursued in these studies constitutes an important step toward a deeper understanding of thin layer dynamics.

4.1 Balancing convergence and turbulence dispersion

One method to infer the mechanism driving the convergence of phytoplankton into a thin layer is to determine the properties of the cells or patches of cells required to counteract the vertical spreading of the layer caused by turbulent dispersion. Although this approach does not establish any direct causal relationships, it can help determine candidate mechanisms. Stacey et al. (2007) applied this method to 4 thin layers observed at pycnoclines in East Sound (Dekshenieks et al. 2001), for which they considered two convergence mechanisms: buoyancy and patch straining. Mechanisms invoking motility were not considered, because layers were mostly comprised of the diatom *Pseudo-nitzschia*, which is nonmotile. Using the measured layer thickness, eddy diffusivity, shear rate, and buoyancy frequency associated with each layer, Stacey et al. (2007) computed the cell diameter $D \sim \left(18 v \kappa_z / N^2 H_e^2\right)^{1/2}$ (see Section 3.3) required to generate the observed convergence by buoyancy and found it to agree remarkably well with independent measurements of the diameter. They also computed the layer tilt angle $\theta \sim (\kappa_z / S_u L_o^2)^{1/3}$ predicted if the layer had formed by straining (see Section 3.1 and **Figure 2a**), under the assumption that thinning by shear had reached a quasi-steady equilibrium with vertical dispersion, as expected at the time of minimum layer thickness (see Section 3.1). The predicted tilt angles also yielded plausible results, but a direct comparison was not possible because θ was not measured in the field. Thus both mechanisms were found

to be consistent with observations and neither could be ruled out as the culprit of layer formation.

A similar analysis was performed by Steinbuck et al. (2009) for thin layers of the dinoflagellate *A. sanguinea* (synonymous with *Gymnodinium sanguinea*) observed at the nutricline in Monterey Bay. *A. sanguinea* is highly motile (Park et al. 2002) and performs daily vertical migrations. Cells were found to begin swimming from the surface down to the nutricline 5--6 h before sunset and to aggregate there (Sullivan et al. 2010a, Ryan et al. 2010). Chlorophyll profiles acquired over 35 min during the afternoon showed that the population formed a thin layer at the thermocline, where turbulent dispersion had a local minimum (**Figure 4a,b**). The layer was highly asymmetric, with the magnitude of the concentration gradient $|\partial c/\partial z|$ below the peak being twice as large as above. This likely resulted from differences in turbulent dispersion, as the upper part of the layer extended into the energetic surface mixed layer ($\kappa_z \sim 10^{-5}$--10^{-4} m^2 s^{-1}), whereas the lower part experienced weaker turbulence ($\kappa_z \sim 10^{-6}$ m^2 s^{-1}).
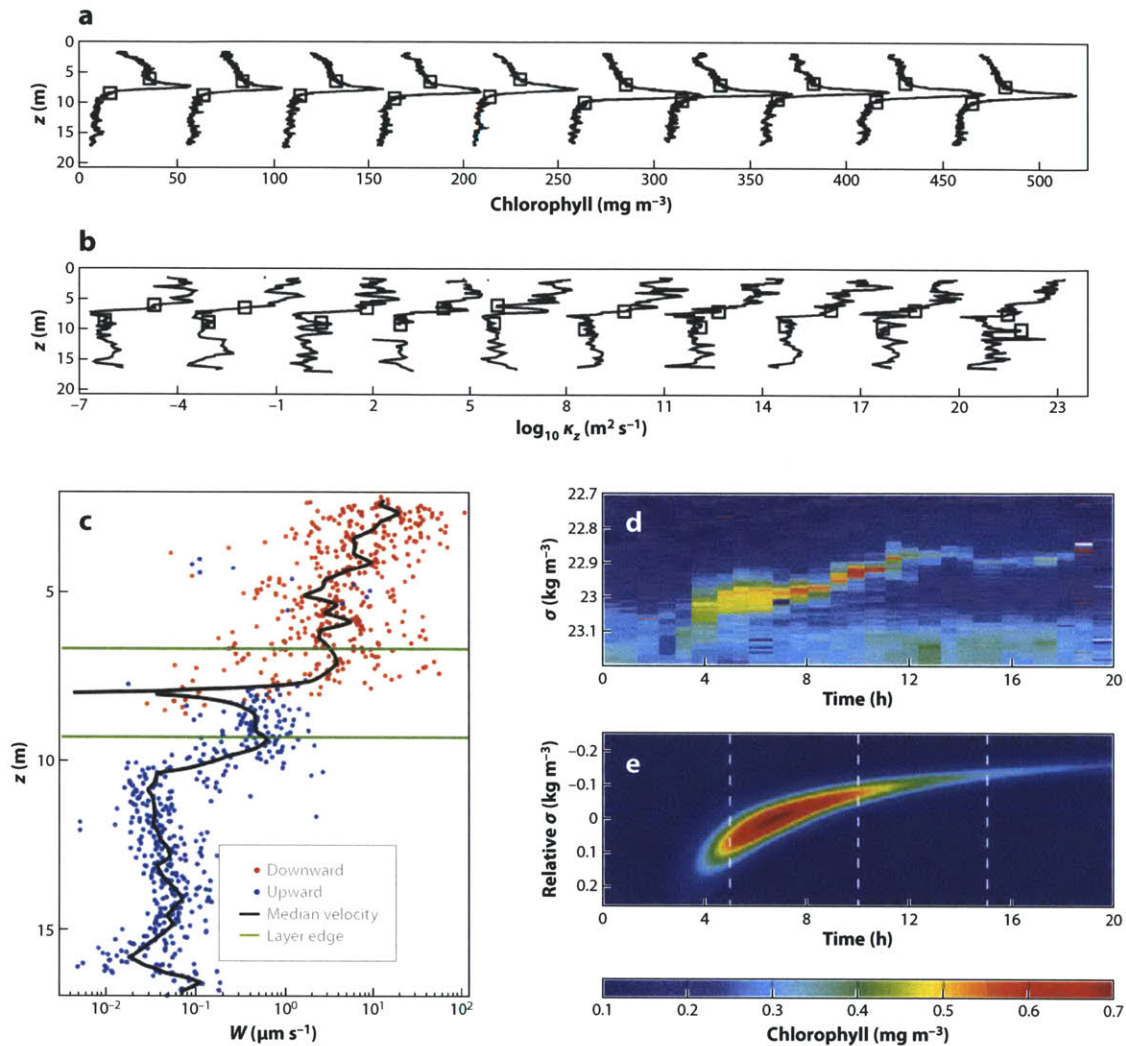
Figure 4 The use of mathematical models to interpret field observations provides insight into the processes that shape layer formation. (*a,b,c*) To maintain a steady phytoplankton distribution in the face of turbulent dispersion, a convergence mechanism must balance the spreading of the layer by turbulence. Using 10 high-resolution profiles of (*a*) the vertical distribution of chlorophyll and (*b*) the vertical eddy diffusivity acquired over a 35-min period in Monterey Bay, Steinbuck et al. (2009) estimated the local swimming velocity $W(z)$ required to balance turbulent dispersion. The median of $W(z)$ is shown by the black line in panel *c*. The edges of the layer are denoted by squares in panels *a* and *b* and by green lines in panel *c*. Vertical turbulent dispersion was larger above than below the layer, resulting in large inferred downward velocities above the layer ($W \sim 10 \ \mu m \ s^{-1}$) and small inferred upward velocities below the layer ($W \sim 0.1 \ \mu m \ s^{-1}$) (see Section 4). Sequential profiles are offset by 50 mg m^{-3} in panel *a* and by three decades in panel *b*. (*d,e*) Thin layers do not occur only in shallow coastal waters. (*d*) A thin layer observed by Hodges & Fratantoni (2009) in the Philippine Sea, where the total water depth exceeds 5,000 m. The layer exhibited a chlorophyll distribution that

was tilted across lines of constant density (measured here in terms of the sigma-theta density, σ), a feature of layers formed via straining. (e) A simple model of straining successfully reproduces the basic characteristics of the layer.

Panels (a,b,c) were reproduced with permission from Steinbuck JV, Stacey MT, McManus MA, Cheriton OM, Ryan JP, 2009, Observations of turbulent mixing in a phytoplankton thin layer: Implications for formation, maintenance, and breakdown. *Limnol. Oceanogr.* 54: 1353-68. Panels (a,b): copyright 2009 by the American Society of Limnology and Oceanography, Inc. Panel (c) was redrawn using data provided by the authors.

Panels (d,e) were modified with permission from Hodges BA, Fratantoni DM, 2009, A thin layer of phytoplankton observed in the Philippine Sea with a synthetic moored array of autonomous gliders. *J. Geophys. Res. Oceans* 114: C10020. Copyright 2009 American Geophysical Union.

Steinbuck et al. (2009) assumed that these layers were in steady state, with either cell motility or cell buoyancy balancing turbulent dispersion. This balance between convergence (by motility or buoyancy) and divergence (by turbulence) is expressed by the steady-state advection-diffusion equation (see Equation 1),

$$\frac{d(cW)}{dz} = \frac{d}{dz}\left(\kappa_z \frac{dc}{dz}\right). \quad (4)$$

From this, one can infer the vertical convergence velocity, $W(z)$, required at each depth z to balance turbulent dispersion. Equation 4 yields $\ln(c/c_o) = \int(W/\kappa_z)dz$ and, by differentiation, $W(z) = \kappa_z d\,[\ln(c/c_o)]/dz$, where c_o is the maximum cell concentration. This expression, combined with high-resolution measurements of κ_z, was used by Steinbuck et al. (2009) to determine the convergence velocity $W(z)$ required to produce the observed concentration profiles, c/c_o.

Because of its larger vertical eddy diffusivity κ_z, the region above the layer was found to require a much faster convergence velocity ($W \sim 10\ \mu m\ s^{-1}$) than the region below the layer ($W \sim 0.1\ \mu m\ s^{-1}$) (**Figure 4c**). Although sinking speeds of *A. sanguinea* can be of this order [$\approx$20 $\mu m\ s^{-1}$; Kamykowski et al. (1992)], layer formation by buoyancy was ruled out because gradients in fluid density were too weak: Measurements of the buoyancy frequency N showed that the settling velocity would have changed by only 1% over the depth of the layer, insufficient to explain observed accumulations. Instead, thin layers were consistent with an accumulation by convergent swimming, as this species' 300 $\mu m\ s^{-1}$ swimming speed (Park et al. 2002) was more than sufficient to account for the inferred velocities W.

To determine the time required for layer formation, Steinbuck et al. (2009) solved the unsteady advection-diffusion equation (Equation 1) using the inferred vertical swimming velocity profile for $W(z)$ (**Figure 4c**). Equation (1) was then integrated in

time until the predicted vertical profile converged to the measured profile [convergence was guaranteed because the steady version of the same equation had been used to find $W(z)$]. The computed layer-formation time of 6 days was much longer than the measured time of a few hours, suggesting that $W(z)$ had been considerably higher during layer formation. Imposing a uniform downward swimming velocity of 20 μm s^{-1} yielded the correct formation times (Sullivan et al. 2010a), but much thinner layers than was observed. Furthermore, independent estimates showed that vertical migration velocities were more than one order of magnitude larger (~240 μm s^{-1}) (Sullivan et al. 2010a).

Steinbuck et al. (2009) used the same method to rule out enhanced growth as the sole mechanism responsible for the formation of those layers. By solving the steady advection-diffusion equation balancing growth and turbulent dispersion, they computed the net growth rate, $\mu_{net}(z)$, necessary to counteract dispersion at each depth z, such that the predicted concentration profile matched the observed one. Net mortality ($\mu_{net} < 0$) was inferred on either side of the peak and net growth ($\mu_{net} > 0$) along the layer's centerline, the latter occurring at a rate that exceeded the maximum growth rate recorded for *A. sanguinea* (Doucette & Harrison 1990). In addition, the unsteady advection-diffusion equation predicted a layer-formation time 30-fold larger than measured, providing further support against layer formation via enhanced growth.

4.2 Fitting to an ideal distribution

Prairie et al. (2011) applied a similar technique to estimate the convergence strength, with one difference: they assumed that in the absence of turbulent dispersion, the phytoplankton distribution, $c(z)$, tends to an ideal distribution, $c^*(z)$, with finite thickness of H_T. H_T is a characteristic of the underlying convergence process and represents a lower bound for the layer thickness. In contrast, in some convergence models layers would be infinitely thin in the absence of turbulence (*e.g.* convergent swimming, buoyancy, and gyrotactic trapping; see Section 3). Prairie et al. (2011) developed a framework to determine H_T and q, the rate at which $c(z)$ tends to $c^*(z)$, by fitting measured vertical gradients of phytoplankton abundance. Using 30-cm segments from 7 high-resolution phytoplankton profiles collected in the Santa Barbara Channel, they found $H_T \sim 1$ m and $q = 0.5$–0.9 day^{-1}. The latter values are in line with maximal growth rates of *Pseudo-nitzchia*, the dominant genus during the observations (Prairie et al. 2010), suggesting that enhanced growth within 1 m thick regions of the water column could have formed the observed layers (though other mechanisms, such as buoyancy, could not be ruled out). By providing information on thickness and rate of convergence, this approach represents a useful addition to the tools that can be applied to identify mechanisms of layer formation.

4.3 Quantifying changes in layer thickness

Another approach to infer convergence mechanisms is based on the quantification of the rate of change of layer thickness, dH/dt. This was done by Cheriton et al. (2009) for 99 profiles of a thin layer of *A. sanguinea* collected over an 8.5-h nighttime period in Monterey Bay. They compared the mean observed rate of change, $(dH/dt)_{obs} \approx -2$ mm s^{-1}, with the rates of layer convergence predicted for buoyancy, straining, and motility.

Following the scaling analysis of Stacey et al. (2007), Cheriton and coworkers computed the convergence rates as $(dH/dt)_{sink} \approx w_2 - w_1 \approx -0.3$ μm s^{-1} for sinking (where w_1 and w_2 are the sinking speeds at the upper and lower boundaries of the layer, calculated using the local fluid density; see Section 3.3); $(dH/dt)_{strain} \approx -H/\Delta t \approx -60$ μm s^{-1} for straining (where Δt is the time since the onset of patch straining and the tilt angle is assumed to be small); and $(dH/dt)_{swim} \approx -2w_s \approx -600$ μm s^{-1} for convergent swimming. All three predicted rates were considerably smaller in magnitude than $(dH/dt)_{obs}$, suggesting that none of these mechanisms produced the layer.

Yet, further inspection revealed that internal waves produced oscillatory contractions and expansions of isopycnals (surfaces of constant density), greatly increasing the apparent, instantaneous dH/dt (Cheriton et al. 2009). This internal-wave-driven thinning and thickening is a transient and reversible process (Franks 1995, Stocker & Imberger 2003). After removing it, by calculating dH/dt relative to isopycnals, Cheriton et al. (2009) found that straining and sinking were still too weak and that only swimming could have produced the observed convergence rates. However, we note that this treatment omits the effect of turbulent dispersion: $(dH/dt)_{obs}$ did not result solely from the convergence mechanism, but from the competition between the convergence mechanism and turbulent dispersion, casting some doubt on the validity of this approach to infer convergence mechanisms. For example, including dispersion would further increase the required rate of layer convergence (Steinbuck et al. 2009), implying that even swimming might not have been sufficient to produce the layer.

4.3 Case studies: inferring convergence mechanisms from systematic analysis

A systematic and insightful analysis of possible mechanisms of layer formation, providing a template for future studies, was presented by Steinbuck et al. (2010). These authors investigated thin layers, likely dominated by the cyanobacteria *Prochlorococcus* and *Synechococcus*, observed 1.6 km offshore in the Gulf of Aqaba. Patch straining was excluded because the required initial patch length $L \sim (H_{min})^3 S_u / \kappa_z \sim 10^2$--$10^4$ km (see Section 3.1)---calculated using parameters measured in situ---was much larger than could be contained in the narrow bay (<10 km). The swimming speeds required to balance turbulent dispersion, $w_s \sim \kappa_z / H_e$ (see Section 3.2), were small (~0.1--1 μm s^{-1}) and easily achieved by the motile clade of *Synechococcus*. However, dividing the layer's excess concentration, Δc (relative to the surrounding concentration c_{ext}), by the flux of cells due to swimming, $w_s c_{ext}$, yielded a timescale of layer formation, $H_e \Delta c / (w_s c_{ext}) \sim$ 10--100 days, much larger than was observed (~1 day). Buoyancy was also excluded because the cell diameter required to compensate turbulent dispersion,

$$D > \left(18 v \kappa_z / N^2 H_e^2\right)^{1/2} = 50\text{--}400 \text{ μm (see Section 3.3), was much larger than the <5-μm}$$

size of the cyanobacteria.

Near the shore, chlorophyll concentrations were similar to those found in the layers, suggesting that layers were formed by intrusions. To test this hypothesis, Steinbuck and coworkers integrated the horizontal fluid velocity at the depth of the layers backward in time to estimate the path of the water before it arrived at the sampling location. Thin layers were observed when water originated from the shoreward direction, whereas no

layers formed when water originated from offshore. The thickness and intrusion time of the layers were successfully compared to theoretical predictions. The time required to propagate the distance from shore, L_{in} = 1.6 km, was computed to be $t_{in} \approx L_{in}^2 / (2\kappa_{in}) \approx$ 5--20 h (see Section 3.6), in good agreement with estimates obtained from the integration of horizontal velocities. The predicted increase in layer thickness with time, $H' \approx (2\kappa_z t_{in})^{1/2} \approx$ 6--10 m (see Section 3.6), was also consistent with observations, indicating that turbulent dispersion would not completely dissipate the intruding high cell concentrations before they reached the sampling location.

In one of the few thin phytoplankton layer recordings made in the open ocean, Hodges & Fratantoni (2009) used autonomous gliders to sample a layer located 800 km east of the Luzon Strait, in ≈5,000-m water depth. A patch of low-salinity, high-chlorophyll water was advected across the 100 × 100 km² sampling area, at a depth of 100 m, ≈40 m above the deep chlorophyll maximum. The layer was observed simultaneously by two gliders separated by 75 km, implying that it extended for at least this distance. Over a 16-h period, the layer thickness decreased from 20 to 2 m. This coincided with the thinning of the low-salinity lens, indicating that cells were not actively moving relative to the flow. As it thinned, the layer tilted across isopycnals, consistent with patch straining (see Section 3.1). The shear required to strain the patch was likely provided by the diurnal internal waves observed during the study. Hodges & Fratantoni (2009) developed a model of layer formation via patch straining, similar to that of Birch et al. (2008) but neglecting turbulent dispersion, which gave good agreement with their observations (**Figure 4d,e**).

The formation of some layers appears to be driven by the interaction of cell motility and flow. Sullivan et al. (2010a) observed thin layers of the highly motile, toxic dinoflagellate *Alexandrium catenella* in Monterey Bay. No clear diel pattern was found, possibly because of confounding effects due to the simultaneous presence of nonmotile species (e.g., *Chaetoceros*) (Rines et al. 2010). Layers formed 1--2 m beneath peaks in shear, during both the daytime and nighttime. The shear rate averaged $S \approx 0.01$ s^{-1} at the center of the layers and peaked at $S \approx 0.03$ s^{-1} above the layers. Turbulence was also enhanced above the layers. Sullivan et al. (2010a) suggested that these layers might have formed as a result of modifications of the cells' swimming behavior. This hypothesis is supported by laboratory experiments in which shear was found to markedly affect *A. catenella*'s swimming behavior (Karp-Boss et al. 2000). Flow-induced changes in swimming are predicted by gyrotactic trapping, in which shear inhibits vertical motility by inducing phytoplankton tumbling, either through the mean flow (Durham et al. 2009) or via turbulence (Durham et al. 2011). Confirmation of this hypothesis, however, will require in situ observations of cell motility and knowledge of the cells' critical shear rate (B^{-1}) (see Section 3.4).

An interesting case is provided by the thin layers associated with a region of upwelling that occurred in Monterey Bay in 2003, independently observed by Ryan et al. (2008) and Johnston et al. (2009). Ryan et al. (2008) found that all layers occurred at the thermocline and most (92%) coincided with depths where ambient currents sharply changed direction over depth. Vertical shear profiles exhibited a strong peak that

coincided with the center of the layers and thinner layers were associated with higher shear rates. The layers' species composition was not determined, but cells did not exhibit vertical migration: The layer depth closely followed a single isotherm, indicating that cells were not moving relative to the fluid. Synoptic mapping revealed the presence of strong horizontal patchiness at 1--3 km scales before layers were observed. This patchiness, together with the observed correlation of layers with shear, led both Ryan et al. (2008) and Johnston et al. (2009) to suggest that layers had formed via patch straining. However, Johnston et al. (2009) noted that chlorophyll concentrations within the layers were larger than in the upwelled subsurface chlorophyll maxima from which the layers originated. This fact implies that a mechanism other than straining (e.g., in situ growth) determined or codetermined the formation of these layers, because straining cannot account for an increase in concentration compared to the original patch (see Section 3.1).

4.4 Concluding remarks

We conclude this section by noting that, to date, identification of the mechanism driving the formation of a thin layer is rarely achieved by direct observation, but rather by using theoretical models to determine which mechanisms are capable of producing salient features of the layer and to rule out mechanisms with attributes that are incompatible with observations. It would be highly desirable to complement this deductive approach with novel observational techniques that directly characterize rates of layer convergence, permitting more definitive conclusions about the mechanisms of layer formation. For example, because thin layers can form as a result of phytoplankton motility, it will be important to develop techniques to quantify cell motility in situ. Such direct observations of biophysical marine processes are sorely needed to interpret field observations and inform predictive models. Furthermore, the overwhelming majority of thin layer observations has been made in coastal water bodies: comprehensive studies in other locales, including the open ocean, would enable a broader understanding of the processes relevant to layer formation and a greater ability to test hypotheses on the role of thin layers in the instigation of HABs (see Section 2.9).

5. TROPHIC INTERACTIONS

Thin layers are a remarkable example of a heterogeneous distribution of primary producers. By concentrating large amounts of prey over small depth intervals, thin layers have the potential to induce predator aggregation and thus substantially increase trophic transfer rates compared to more homogeneous phytoplankton distributions (Cowles et al. 1998, Tiselius et al. 1993). Indeed correlations between thin layers of phytoplankton and zooplankton are often observed (Benoit-Bird et al. 2009, 2010; Gallager et al. 2004; McManus et al. 2003, Menden-Deuer 2008, Menden-Deuer & Fredrickson 2010), although zooplankton avoidance of toxic and mucus-rich phytoplankton layers has also been reported (Alldredge et al. 2002, Bjornsen & Nielsen 1991, Nielsen et al. 1990).

An early, dramatic link between phytoplankton layers and higher trophic levels was demonstrated by Lasker (1975), who found that the feeding success of anchovy larvae in water collected from within a thin layer of *Gymnodinium sanguineum* (syn.

Gymnodinium splendens) was dramatically greater than in water collected from the surface. Furthermore, larval feeding was negligible after a storm had destroyed the thin layer, likely because prey concentrations became too dilute. This finding is emblematic of a fundamental principle of planktonic life in the sea: resource densities are often too low for survival (e.g. Mullin & Brooks 1976), as summarized in the adage "the mean fish is a dead fish" (Preston et al. 2010). In this respect, Lasker's observations exemplify the critical role that thin layers can play in the sustenance of higher trophic levels and highlight their potential impact on the recruitment of fish larvae.

One strategy that predators use to enhance foraging when prey distributions are heterogeneous is to engage in area-restricted search behavior. In phytoplankton layers, this behavior can result from a number of predator adaptations, including altered swimming speeds, increased turning rates, and a bias of swimming in the horizontal direction (Tiselius 1992, Woodson et al. 2005). The ability of predators to exploit phytoplankton layers was demonstrated in experiments in which copepods (*Acartia tonsa*) were exposed to two different distributions of prey (*Thalassiosira weissflogii*) within a 20-cm tall column (Tiselius 1992). In the first treatment, phytoplankton cells were distributed homogeneously over depth, whereas in the second treatment, they were confined to a 3-cm-thick layer, at the same concentration. Despite the total abundance of prey being more than six times larger in the homogeneous treatment, the grazing rates were very similar in the two cases owing to the copepods' ability to find and maintain their position within the layer (Tiselius 1992).

Herbivorous zooplankters likely use a variety of cues to locate thin phytoplankton layers. The use of chemical cues is demonstrated by the observation that grazers aggregate in patches of cell-free phytoplankton exudates (Menden-Deuer & Grünbaum 2006, Woodson et al. 2007). It has also been speculated that physical cues---including vertical gradients in fluid density and fluid velocity---might be used by predators as proxies to find thin layers. For example, grazers actively aggregate at pycnoclines (Harder 1968, Harvey & Menden-Deuer 2011) and engage in area-restricted search behaviors where shear is enhanced (Woodson et al. 2005, 2007): both density gradients and velocity gradients are often associated with thin phytoplankton layers (see Section 2.7). Woodson et al. (2007) posited that such strategies allow predators to focus on regions of the water column more likely to contain prey. Harder (1968) observed that the copepod *Temora longicornis* aggregated at density gradients when there was no corresponding gradient in salinity but failed to aggregate in salinity gradients when there was no associated gradient in density, suggesting that copepods may actively seek pycnoclines using mechanical cues, as opposed to passively aggregating there in response to salt-induced stress.

Behavioral adaptations that allow grazers to aggregate within a thin phytoplankton layer are not without risk: Although this strategy confers increased foraging rates, it also exposes grazers to potentially higher mortality rates due to predation by higher trophic levels (e.g., larger zooplankton or fish). This trade-off has been analyzed using individual-based models of organisms foraging within patchy, layered prey landscapes (Tiselius et al. 1993). Two classes of grazers were simulated---ciliates and copepods--- using functional responses, swimming speeds, and predation risks typical of each class.

In the absence of predation by higher trophic levels, both classes of grazers benefitted from an area-restricted search behavior in terms of enhanced growth rates. However, when predation of grazers was included, ciliates achieved a higher net growth rate by adopting an area-restricted search behavior, whereas this strategy conferred only marginal advantages to copepods. These results indicate that, for copepods, accumulating to forage on thin phytoplankton layers is beneficial only under certain conditions. Consistent with these predictions, observations in East Sound revealed that thin phytoplankton layers were correlated with increased ciliate (and heterotrophic dinoflagellate) abundance, though it could not be ascertained whether these correlations occurred due to altered motility or enhanced predator growth rates (Menden-Deuer 2008).

5.1 Three case studies

With these general considerations as a background, we now focus on three field studies that provide a unique perspective on the relationship of thin phytoplankton layers with higher trophic levels. The first study is a detailed analysis of the correlations between vertical phytoplankton and zooplankton distributions during nighttime hours in Monterey Bay, recorded in 2006 and 2008 (Benoit-Bird et al. 2010). Both phytoplankton and zooplankton were observed to intermittently aggregate into layers. While the acoustic technique used to sample zooplankton layers does not readily permit organism identification, net tows found that 90% of the zooplankton biomass was composed of three copepod genera (*Calanus*, *Ctenocalanus*, and *Acartia*). While the depth of the zooplankton layer and that of the phytoplankton layer were sometimes highly correlated, at other times they were up to 16 m apart. Whether phytoplankton and zooplankton layers were colocalized was independent of the phytoplankton layer's peak chlorophyll concentration and instead correlated with the fraction of chlorophyll contained within the layer (**Figure 5a**): For phytoplankton layers comprising >20% of the total chlorophyll in the water column, there was typically zooplankton layers in close proximity. Although the mechanism that led to this correlation remains unknown, this analysis suggests that zooplankton can assess prey availability over the entire depth of the water column, likely through vertical migration. Conversely, it is interesting to note that the likelihood of a zooplankton layer occurring at any depth was independent of whether a thin phytoplankton layer was present. More broadly, this result shows that the trophic consequences of thin phytoplankton layers cannot be assessed without considering the distribution of phytoplankton over the rest of the water column. Finally, it is tempting to draw a connection between these results and the aforementioned model of Tiselius et al. (1993): Might copepods expose themselves to higher predation risks only when their phytoplankton prey are highly aggregated, such that the payoff shifts the gamble in their favor?

The second study we focus on provides perhaps the only field measurement of grazing rates within thin layers, a crucial step towards quantifiying the ecological interactions between phytoplankton and zooplankton in layers. Using samples collected from within and outside thin layers in East Sound, Washington over three years, Menden-Deuer & Fredrickson (2010) performed laboratory dilution experiments to estimate in situ rates of phytoplankton growth and grazing, the latter limited to small (<200 μm) protistan

grazers. Although the mechanisms responsible for layer formation were not identified, two conclusions could be reached. First, in situ growth was ruled out as the layer formation mechanism, because phytoplankton growth rates were the same inside and outside layers ($\mu = 0.34$ d^{-1}). Second, most layers were short-lived (less than a few days) and average grazing rates were considerably higher inside layers ($r = 0.25$ d^{-1}) than outside ($r = 0.09$ d^{-1}). This is consistent with the hypothesis that layer persistence is curtailed by enhanced predation pressure: If grazing removes phytoplankton from a layer faster than convergent processes transport them into it, a reduction in the layer's intensity will occur.
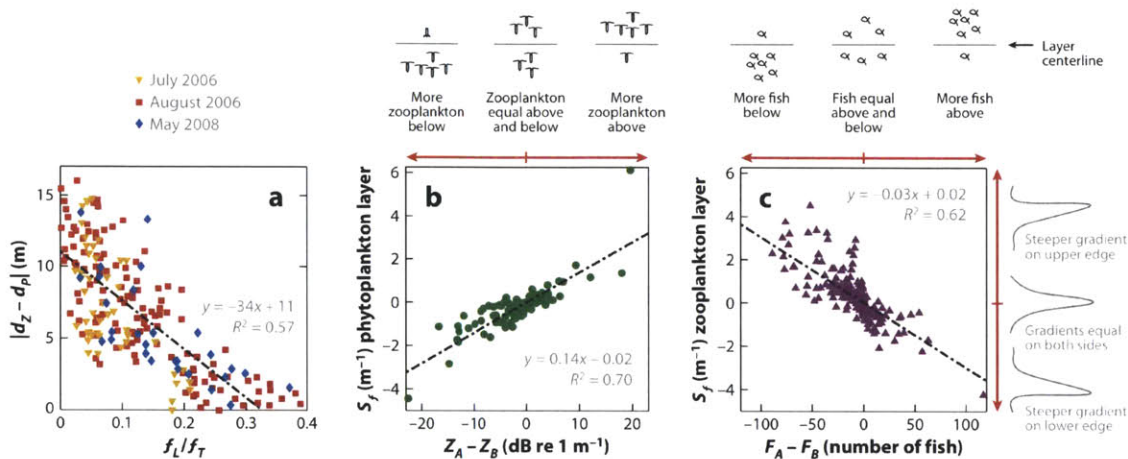
Figure 5 Thin phytoplankton layers are often correlated with the distribution of organisms from higher tropic levels, although the mechanisms behind these correlations remain largely unknown. (*a*) Benoit-Bird et al. (2010) measured the vertical distance $|d_Z - d_P|$ between the depth of the zooplankton layer d_Z and the depth of the phytoplankton layer d_P, over 11 nights in Monterey Bay. The distance was smaller when the fraction of chlorophyll in the phytoplankton layer, relative to the entire water column, f_L/f_T, was larger. This suggests that zooplankters scan the entire water column, aggregating near phytoplankton layers only when these are sufficiently concentrated. (*b,c*) Higher trophic levels can affect the vertical structure of thin layers of phytoplankton and zooplankton. Benoit-Bird et al. (2009) quantified the vertical asymmetry of thin layers by means of a shape factor, S_f, for thin layers observed in Monterey Bay. S_f measures the difference in the magnitude of the concentration gradient above and below the layer (e.g., $S_f > 0$ indicates that the gradient is sharper at the upper edge; see Section 5). The difference in the amount of predators above and below the layer is $Z_A - Z_B$ for zooplankton (on a logarithmic scale, in panel *b*) and $F_A - F_B$ for fish. The asymmetry in the shape of the phytoplankton layer is well predicted by the relative distribution of zooplankton (*b*). Similarly, the asymmetry in the shape of the zooplankton layer is well predicted by the relative distribution of fish (*c*). However, the two trends are opposite: The phytoplankton layer is steeper on the side with more zooplankton, whereas the zooplankton layer is steeper on the side with less fish. In all panels, the black lines are least-squares regressions to the data.

Panel (a) was redrawn with permission from Benoit-Bird KJ, Moline MA, Waluk CM, Robbins IC, 2010, Integrated measurements of acoustical and optical thin layers I: Vertical scales of association. *Cont. Shelf Res.* **30: 17-28, using data provided by the authors.**

Panels (*b,c*) were redrawn with permission from Benoit-Bird KJ, Cowles TJ, Wingard CE, 2009, Edge gradients provide evidence of ecological interactions in planktonic thin layers. *Limnol. Oceanogr.* **54: 1382-92, using data provided by the authors.**

The third study analyzes the effect of predation on the vertical structure of a thin layer. As we saw, gyrotactic trapping (see Section 3.4) and gradients in vertical eddy diffusivity lead to asymmetric layers (see Section 4), in which the concentration gradients $|\partial c/\partial z|$ above and below the layer differ. From data collected in Monterey Bay, Benoit-Bird et al. (2009) showed that such asymmetries can also result from the interaction with higher trophic levels, for both phytoplankton and zooplankton layers. Layer asymmetry was quantified with a shape factor, $S_f = (|\partial s/\partial z|_{above} - |\partial s/\partial z|_{below})/\max(s)$, where s is the local abundance of the organism composing the layer. Normalization by the peak abundance, $\max(s)$, removed the influence of layer intensity. No correlation was found between S_f and differences in vertical shear above and below the layer, indicating that layer asymmetry was likely not associated with gyrotactic trapping or gradients in turbulent dispersion. Instead, S_f was well correlated with predator abundance, but, intriguingly, asymmetries in predator abundance showed the opposite trend in the two types of layers: Phytoplankton layers had a steeper gradient on the side where more zooplankters resided (**Figure 5b**), whereas zooplankton layers had shallower gradients on the side containing more fish (**Figure 5c**). Furthermore, in the absence of predators, thin layers of both types were more symmetric with 10-fold smaller S_f. While the mechanisms mediating these interactions remain unknown, the shape factor of both types of prey layers appear to be actively modulated by predators (Benoit-Bird et al. 2009, Benoit-Bird 2009), suggesting that layers did not result from predators' preference for a particular prey gradient. In summary, this study demonstrates how trophic interactions can be a driver of layer morphology and suggests that predators should be considered when assessing layer dynamics.

SUMMARY POINTS

1.   Thin phytoplankton layers are recurrent features of the marine environment, observed mostly in the coastal ocean but recently also in open waters, that can harbor a considerable fraction of the water column's primary producers within small depth intervals.

2.   Advanced sampling technologies and meticulous field campaigns have greatly increased our ability to quantify thin layer characteristics, dynamics, and accompanying environmental conditions.

3.   Thin phytoplankton layers can form owing to diverse biophysical mechanisms, including cell behavior (e.g., motility, sensing), morphology (e.g., cell diameter, density,

asymmetry), fluid flow (e.g., shear, intrusions), and population dynamics (e.g., cell growth, grazing rates). Each convergence mechanism produces distinctive layer characteristics and correlations with the biophysical environment that can help diagnose the processes at play in field observations.

4. Scaling analyses and mathematical models of layer formation have been applied to field observations to identify candidate mechanisms and rule out those that are incompatible. However, rarely have putative mechanisms been directly demonstrated.

5. Thin layers of toxic phytoplankton species may play an important role in instigating HABs.

6. As trophic hotspots, thin phytoplankton layers can play an outsized role in mediating the survival and reproduction rates of organisms belonging to higher trophic levels.

7. The predators of phytoplankton may have evolved behavioral adaptations to locate and exploit thin layers, yet the specific tradeoffs that underlie observed correlations between the positions of thin phytoplankton layers and predator assemblages remain unknown.

FUTURE ISSUES

1. Broadening the scope of future field campaigns to new, diverse environments, including the open ocean and lakes, will test the universality of currently proposed mechanisms for layer formation.

2. Developing the next generation of mathematical models and scaling arguments that incorporate salient features of field observations will allow for a tighter coupling between models and observations.

3. The development of novel techniques that enable cell behavior to be observed in situ will allow direct testing and informed discrimination of layer-formation mechanisms.

4. New laboratory experiments can enable controlled tests of specific layer-formation processes, quantification of phytoplankton responses to imposed stimuli, and measurements of phytoplankton physiological and morphological parameters, especially as they pertain to motility.

5. The incorporation of the biophysical interactions that drive thin layer dynamics into models of HABs could enhance these models' predictive abilities and contribute to the development of bloom forecasting.

6. Understanding the trade-offs of residing in concentrated thin layers will provide a clearer ecological picture of the causes and consequences of thin layers.

110

7.   Determining the processes that mediate the co-occurrence of thin phytoplankton layers, zooplankton layers, and fish will help assess impacts of thin layers on the marine food web.

DISCLOSURE STATEMENT

ACKNOWLEDGMENTS

LITERATURE CITED

Alldredge AL, Cowles TJ, MacIntyre S, Rines JEB, Donaghay PL, et al. 2002. Occurrence and mechanisms of formation of a dramatic thin layer of marine snow in a shallow Pacific fjord. *Mar. Ecol. Prog. Ser.* 233:1—12

Armi L. 1978. Some evidence for boundary mixing in the deep ocean. *J. Geophys. Res.* 83: 1971-1979

Baek SH, Shimode S, Shin K, Han MS, Kikuchi T. 2009. Growth of dinoflagellates, *Ceratium furca* and *Ceratium fusus* in Sagami Bay, Japan: the role of vertical migration and cell division. *Harmful Algae* 8:843--56

Benoit-Bird KJ, Cowles TJ, Wingard CE. 2009. Edge gradients provide evidence of ecological interactions in planktonic thin layers. *Limnol. Oceanogr.* 54:1382--92

Shows that the vertical structure of a thin layer can be affected by the relative distribution of predators, above and below the layer.

Benoit-Bird KJ. 2009. Dynamic 3-dimensional structure of thin zooplankton layers is impacted by foraging fish. *Mar. Ecol. Prog. Ser.* 396: 61-76

Benoit-Bird KJ, Moline MA, Waluk CM, Robbins IC. 2010. Integrated measurements of acoustical and optical thin layers I: vertical scales of association. *Cont. Shelf Res.* 30:17--28

Shows that zooplankton layers reside closer to phytoplankton layers when the latter contain a larger fraction of the water column's chlorophyll.

Birch DA, Young WR, Franks PJS. 2008. Thin layers of plankton: formation by shear and death by diffusion. *Deep-Sea Res. Part 1* 55:277--95

Provides a detailed theoretical analysis of layer formation via straining.

Birch DA, Young WR, Franks PJS. 2009. Plankton layer profiles as determined by shearing, sinking, and swimming. *Limnol. Oceanogr.* 54:397--99

Bjornsen PK, Nielsen TG. 1991. Decimeter scale heterogeneity in the plankton during a pycnocline bloom of *Gyrodinium aureolum. Mar. Ecol. Prog. Ser.* 73:263--67

Bollens SM, Rollwagen-Bollens G, Quenette JA, Bochdansky AB. 2011. Cascading migrations and implications for vertical fluxes in pelagic ecosystems. *J. Plankton Res.* 33:349—55

Bracco A, Provenzale A, Scheuring I. 2000. Mesoscale Vortices and the Paradox of the Plankton. *Proc. Roy. Soc. B.* 267: 1795-1800

Brahamsha B. 1999. Non-flagellar swimming in marine *Synechococcus. J. Mol. Microbiol. Biotechnol.* 1:59--62

Calbet A, Landry MR. 2004. Phytoplankton growth, microzooplankton grazing, and carbon cycling in marine systems. *Limnol. Oceanogr.* 49:51--57

Cheriton OM, McManus MA, Stacey MT, Steinbuck JV. 2009. Physical and biological controls on the maintenance and dissipation of a thin phytoplankton layer. *Mar. Ecol. Prog. Ser.* 378:55--69

Cheriton OM, McManus MA, Steinbuck JV, Stacey MT, Sullivan JM. 2010. Towed vehicle observations of thin layer structure and a low-salinity intrusion in Northern Monterey Bay, CA. *Cont. Shelf Res.* 30:39--49

Churnside JH, Donaghay PL. 2009. Thin scattering layers observed by airborne lidar. *ICES J. Mar. Sci.* 66:778--89

Clift R, Grace JR, Weber ME. 1978. *Bubbles, Drops, and Particles.* New York: Academic Press

Cowles TJ. 2004. Planktonic layers: physical and biological interactions on the small-scale. In *Handbook of Scaling Methods in Aquatic Ecology: Measurement, Analysis, Simulation,* ed. L Seuront, PG Strutton, pp. 31--49. Boca Raton, FL: CRC

Cowles TJ, Desiderio RA, Carr ME. 1998. Small-scale planktonic structure: persistence and trophic consequences. *Oceanography* 11:4--9

Cullen JJ. 1982. The deep chlorophyll maximum: comparing vertical profiles of chlorophyll *a. Can. J. Fish. Aquat. Sci.* 39:791--803

Dekshenieks MM, Donaghay PL, Sullivan JM, Rines JEB, Osborn TR, Twardowski MS. 2001. Temporal and spatial occurrence of thin phytoplankton layers in relation to physical processes. *Mar. Ecol. Prog. Ser.* 223:61--71

Provides one of the first quantitative reports of thin layers and their associated physical environment, highlighting the intimate connection between the two.

Donaghay PL, Rines HM, Sieburth JM. 1992. Simultaneous sampling of fine scale biological, chemical, and physical structure in stratified waters. *Archiv. Hydrobiol. Beih.* 36: 97--108.

Donaghay PL, Osborn TR. 1997. Toward a theory of biological-physical control of harmful algal bloom dynamics and impacts. *Limnol. Oceanogr.* 42:1283--96

Doucette GJ, Harrison PJ. 1990. Some effects of iron and nitrogen stress on the red tide dinoflagellate *Gymnodinium sanguineum*. *Mar. Ecol. Prog. Ser.* 62:293--306

Drescher K, Leptos KC, Tuval I, Ishikawa T, Pedley TJ, Goldstein RE. 2009. Dancing *Volvox*: hydrodynamic bound states of swimming algae. *Phys. Rev. Lett.* 102:168101

Durham WM, Climent E, Stocker R. 2011. Gyrotaxis in a steady vortical flow. *Phys. Rev. Lett.* 106:238102.

Durham WM, Kessler JO, Stocker R. 2009. Disruption of vertical motility by shear triggers formation of thin phytoplankton layers. *Science* 323:1067--70

Shows that thin layers can form when vertical migration is disrupted by fluid shear, a process called gyrotactic trapping.

Eckart C. 1948. An analysis of the stirring and mixing processes in incompressible fluids. *J. Mar. Res.* 7:265--75

Eppley RW, Holmes RW, Strickland JDH. 1967. Sinking rates of marine phytoplankton measured with a fluorometer. *J. Exp. Mar. Biol. Ecol.* 1:191—208

Fauchot J, Levasseur M, Roy S. 2005. Daytime and nighttime vertical migrations of *Alexandrium tamarense* in the St. Lawrence estuary (Canada). *Mar. Ecol. Prog. Ser.* 296:241--50

Fenchel T. 2001. How dinoflagellates swim. *Protist* 152:329--38

Fischer HB, List EJ, Koh RCY, Imberger J, Brooks NH. 1979. *Mixing in Inland and Coastal Waters.* New York: Academic

Franks PJS. 1995. Thin-layers of phytoplankton: a model of formation by near-inertial wave shear. *Deep-Sea Res. Part 1* 42:75--91

Franks PJS. 1997. Models of harmful algal blooms. *Limnol. Oceanogr.* 42:1273--82

Gallager SM, Yamazaki H, Davis CS. 2004. Contribution of fine-scale vertical structure and swimming behavior to formation of plankton layers on Georges Bank. *Mar. Ecol. Prog. Ser.* 267:27--43

Gentien P, Donaghay PL, Yamazaki H, Raine R, Reguera B, Osborn T. 2005. Harmful algal blooms in stratified environments. *Oceanography* 18:172--83

Gjosaeter J, Lekve K, Stenseth NC, Leinaas HP, Christie H, et al. 2000. A long-term perspective on the *Chrysochromulina* bloom on the Norwegian Skagerrak coast 1988: a catastrophe or an innocent incident? *Mar. Ecol. Prog. Ser.* 207:201--18

Gross F, Zeuthen E. 1948. The buoyancy of plankton diatoms: a problem of cell physiology. *Proc. R. Soc. Lond. Ser. B* 135:382--89

Grünbaum D. 2009. Peter principle packs a peck of phytoplankton. *Science* 323:1022--23

Guasto JS, Rusconi R, Stocker R. 2012. Fluid mechanics of planktonic microorganisms. *Annu. Rev. Fluid Mech.* 44:In press

Harder W. 1968. Reactions of plankton organisms to water stratification. *Limnol. Oceanogr.* 13:156--68

Harvey EL, Menden-Deuer S. 2011. Avoidance, movement, and mortality: the interactions between a protistan grazer and *Heterosigma akashiwo*, a harmful algal bloom species. *Limnol. Oceanogr.* 56:371--78

Heil CA, Glibert PM, Fan CL. 2005. *Prorocentrum minimum* (Pavillard) Schiller: a review of a harmful algal bloom species of growing worldwide importance. *Harmful Algae* 4:449--70

Hill NA, Häder DP. 1997. A biased random walk model for the trajectories of swimming micro-organisms. *J. Theor. Biol.* 186:503--26

Hodges BA, Fratantoni DM. 2009. A thin layer of phytoplankton observed in the Philippine Sea with a synthetic moored array of autonomous gliders. *J. Geophys. Res.* 114:C10020

Using sophisticated glider technology, shows that thin layers are not limited to the coastal ocean but can also occur in the open ocean.

Holliday DV, Pieper RE, Greenlaw CF, Dawson JK. 1998. Acoustical sensing of small-scale vertical structures in zooplankton assemblages. *Oceanography* 11: 18-23

Hutchinson GE. 1961. The paradox of the plankton. *Am. Nat.* 95:137—45

Ivey GN. 1987. Boundary mixing in a rotating stratified fluid. *J. Fluid Mech.* 183:25-44

Jester R, Lefebvre K, Langlois G, Vigilant V, Baugh K, Silver MW. 2009. A shift in the dominant toxin-producing algal species in central California alter phycotoxins in food webs. *Harmful Algae* 8: 291-298

Johnston TMS, Cheriton OM, Pennington JT, Chavez FP. 2009. Thin phytoplankton layer formation at eddies, filaments, and fronts in a coastal upwelling zone. *Deep-Sea Res. Part 2* 56:246--59

Johnston TMS, Rudnick DL. 2009. Observations of the transition layer. *J. Phys. Oceanogr.* 39:780--97

Kamykowski D, Reed RE, Kirkpatrick GJ. 1992. Comparison of sinking velocity, swimming velocity, rotation, and path characteristics among six marine dinoflagellate species. *Mar. Biol.* 113:319--28

Kamykowski D, Yamazaki H. 1997. A study of metabolism-influenced orientation in the diel vertical migration of marine dinoflagellates. *Limnol. Oceanogr.* 42:1189--202

Karp-Boss L, Boss E, Jumars PA. 2000. Motion of dinoflagellates in a simple shear flow. *Limnol. Oceanogr.* 45:1594--602

Kasai A, Kurikawa Y, Ueno M, Robert D, Yamashita Y. 2010. Salt-wedge intrusion of seawater and its implication for phytoplankton dynamics in the Yura Estuary, Japan. *Estuar. Coast. Shelf Sci.* 86:408--14

Kessler JO. 1985. Hydrodynamic focusing of motile algal cells. *Nature* 313:218--20

Koukaras K, Nikolaidis G. 2004. Dinophysis blooms in Greek coastal waters (Thermaikos Gulf, NW Aegean Sea). *J. Plankton Res.* 26:445--57

Kudela RM, Seeyave S, Cochlan WP. 2010. The role of nutrients in regulation and promotion of harmful algal blooms in upwelling systems. *Prog. Oceanogr.* 85:122—35

Kundu PK, Cohen IM. 2004. Fluid mechanics, 3rd ed. Elsevier, San Diego.

Lasker R. 1975. Field criteria for survival of anchovy larvae: relation between inshore chlorophyll maximum layers and successful first feeding. *Fish. Bull.* 73:453--62

Lebert M, Häder DP. 1996. How Euglena tells up from down. *Nature* 379:590

Lévy M. 2008. The modulation of biological production by oceanic mesoscale turbulence. *Lecture notes in physics.* Vol. 744, e.d. AR Robinson, JJ McCarthy and BJ Rothschild, pp. 219-261. Springer-Verlag, Berlin.

MacIntyre JG, Cullen JJ, Cembella AD. 1997. Vertical migration, nutrition and toxicity in the dinoflagellate *Alexandrium tamarense*. *Mar. Ecol. Prog. Ser.* 148:201—16

MacKinnon JA, Gregg MC. 2003. Mixing on the late-summer New England shelf – solibores, shear, and stratification. *J. Phys. Oceano.* 33:1476--92.

Marcos, Seymour J, Luhar M, Durham WM, Mitchell JG, et al. 2011. Microbial alignment in flow changes ocean light climate. *Proc. Natl. Acad. Sci. USA* 108:3860--64

McCarren J, Brahamsha B. 2009. Swimming motility mutants of marine *Synechococcus* affected in production and locations of the s-layer protein swmA. *J. Bacteriol.* 191: 1111-1114.

McManus MA, Alldredge AL, Barnard AH, Boss E, Case JF, et al. 2003. Characteristics, distribution and persistence of thin layers over a 48 hour period. *Mar. Ecol. Prog. Ser.* 261:1--19

McManus MA, Kudela RM, Silver MW, Steward GF, Donaghay PL, Sullivan JM. 2008. Cryptic blooms: Are thin layers the missing connection? *Estuar. Coasts* 31:396--401

McPhee-Shaw E. 2006. Boundary-interior exchange: reviewing the idea that internal-wave mixing enhances lateral dispersal near continental margins. *Deep-Dea Res. Part 2* 53:42--59

Menden-Deuer S, Grünbaum D. 2006. Individual foraging behaviors and population distributions of a planktonic predator aggregating to plankton thin layers. *Limnol. Oceanogr.* 51: 109--116.

Menden-Deuer S. 2008. Spatial and temporal characteristics of plankton-rich layers in a shallow, temperate fjord. *Mar. Ecol. Prog. Ser.* 355: 21--30.

Menden-Deuer S, Fredrickson K. 2010. Structure-dependent, protistan grazing and its implication for the formation, maintenance and decline of plankton patches. *Mar. Ecol. Prog. Ser.* 420: 57--71.

Mitchell JG, Yamazaki H, Seuront L, Wolk F, Li H. 2008. Phytoplankton patch patterns: seascape anatomy in a turbulent ocean. *J. Mar. Syst.* 69:247--53

Moline MA, Benoit-Bird KJ, Robbins IC, Schroth-Miller M, Waluk CM, Zelenke B. 2010. Integrated measurements of acoustical and optical thin layers II: horizontal length scales. *Cont. Shelf Res.* 30:29--38

Mullin MM, Brooks ER. 1976. Some consequences of distributional heterogeneity of phytoplankton and zooplankton. *Limnol. Oceanogr.* 21:784--96

Nielsen TG, Kiorboe T, Bjornsen PK. 1990. Effects of a *Chrysochromulina polylepis* subsurface bloom on the planktonic community. *Mar. Ecol. Prog. Ser.* 62:21—35

Nixon SW. 1995. Coastal marine eutrophication: a definition, social causes, and future concerns. *Ophelia.* 41: 199--219

Osborn TR. 1998. Fine structure, microstructure, and thin layers. *Oceanography* 11:36--43

Paine RT. 1966. Food web complexity and species diversity. *Am. Nat.* 100: 65-75.

Park MG, Cooney SK, Kim JS, Coats DW. 2002. Effects of parasitism on diel vertical migration, phototaxis/geotaxis, and swimming speed of the bloom-forming dinoflagellate *Akashiwo sanguinea*. *Aquat. Microb. Ecol.* 29:11--18

Pedersen F. 1994. The oceanographic and biological tidal cycle succession in shallow sea fronts in the North Sea and the English Channel. *Estuar. Coast. Shelf Sci.* 38:249—69

Phillips OM, Shyu J, Salmun H. 1986. An experiment on boundary mixing: mean circulation and transport rates. *J. Fluid Mech.* 173: 473--499.

Polin M, Tuval I, Drescher K, Gollub JP, Goldstein RE. 2009. *Chlamydomonas* swims with two "gears" in a eukaryotic version of run-and-tumble locomotion. *Science* 325:487--90

Prairie JC, Franks PJS, Jaffe JS. 2010. Cryptic peaks: invisible vertical structure in fluorescent particles revealed using a planar laser imaging fluorometer. *Limnol. Oceanogr.* 55:1943—58

Prairie JC, Franks PJS, Jaffe JS, Doubell MJ, Yamazaki H. 2011. Physical and biological controls of vertical gradients in phytoplankton. *Limnology and Oceanography: Fluids and Environments*. 1: 75-90.

Preston MD, Pitchford JW, Wood AJ. 2010. Evolutionary optimality in stochastic search problems. *J. R. Soc. Interface* 7:1301--10

Ralston DK, McGillicuddy DJ, Townsend DW. 2007. Asynchronous vertical migration and bimodal distribution of motile phytoplankton. *J. Plankton Res.* 29:803--21

Richardson TL, Cullen JJ, Kelley DE, Lewis MR. 1998. Potential contributions of vertically migrating *Rhizosolenia* to nutrient cycling and new production in the open ocean. *J. Plankton Res.* 20:219--41

Rines JEB, Donaghay PL, Dekshenieks MM, Sullivan JM, Twardowski MS. 2002. Thin layers and camouflage: hidden *Pseudo-nitzschia* spp. (Bacillariophyceae) populations in a fjord in the San Juan Islands, Washington, USA. *Mar. Ecol. Prog. Ser.* 225:123--37

Rines JEB, McFarland MN, Donaghay PL, Sullivan JM. 2010. Thin layers and species-specific characterization of the phytoplankton community in Monterey Bay, California, USA. *Cont. Shelf Res.* 30:66--80

Roberts AM, Deacon FM. 2002. Gravitaxis in motile micro-organisms: the role of fore-aft body asymmetry. *J. Fluid Mech.* 452:405--23

Ross ON, Sharples J. 2004. Recipe for 1-D Lagrangian particle tracking models in space-varying diffusivity. *Limnol. Oceanogr. Methods* 2:289--302

Ryan JP, McManus MA, Paduan JD, Chavez FP. 2008. Phytoplankton thin layers caused by shear in frontal zones of a coastal upwelling system. *Mar. Ecol. Prog. Ser.* 354:21--34

Ryan JP, McManus MA, Sullivan JM. 2010. Interacting physical, chemical and biological forcing of phytoplankton thin-layer variability in Monterey Bay, California. *Cont. Shelf Res.* 30:7--16

Sellner KG, Doucette GJ, Kirkpatrick GJ. 2003. Harmful algal blooms: causes, impacts and detection. *J. Ind. Microbiol. Biotechnol.* 30:383—406

Seymour JR, Marcos, Stocker R. 2009. Resource patch formation and exploitation throughout the marine microbial food web. *Am. Nat.* 173: 15-29

Simpson JH, Tett PB, Argoteespinoza ML, Edwards A, Jones KJ, Savidge G. 1982. Mixing and phytoplankton growth around an island in a stratified sea. *Cont. Shelf Res.* 1:15--31

Smayda TJ. 1997. Harmful algal blooms: their ecophysiology and general relevance to phytoplankton blooms in the sea. *Limnol. Oceanogr.* 42:1137--53

Stacey MT, McManus MA, Steinbuck JV. 2007. Convergences and divergences and thin layer formation and maintenance. *Limnol. Oceanogr.* 52:1523--32

Develops scaling relations for the expected layer thickness based on the competition between various convergence mechanisms and turbulent dispersion.

Steele JH. 1974. Spatial heterogeneity and population stability. *Nature* 248:83

Steinbuck JV, Genin A, Monismith SG, Koseff JR, Holzman R, Labiosa RG. 2010. Turbulent mixing in fine-scale phytoplankton layers: observations and inferences of layer dynamics. *Cont. Shelf Res.* 30:442--55

Applies a systematic, deductive approach to determine the mechanism responsible for layer formation, providing a template for the analysis of future field observations.

Steinbuck JV, Stacey MT, McManus MA, Cheriton OM, Ryan JP. 2009. Observations of turbulent mixing in a phytoplankton thin layer: implications for formation, maintenance, and breakdown. *Limnol. Oceanogr.* 54:1353--68

Tests the hypothesis that thin layers can form by convergent swimming, by inferring swimming speeds from field measurements.

Stocker R, Imberger J. 2003. Horizontal transport and dispersion in the surface layer of a medium-sized lake. *Limnol. Oceanogr.* 48:971--82

Strickland JDH. 1968. A comparison of profiles of nutrient and chlorophyll concentrations taken from discrete depths and by continuous recording. *Limnol. Oceanogr.* 13:388--91

Provides the first published report of thin phytoplankton layers, presciently noting that thin layers limit our ability to measure phytoplankton abundance with traditional techniques.

Sullivan JM, Donaghay PL, Rines JEB. 2010a. Coastal thin layer dynamics: consequences to biology and optics. *Cont. Shelf Res.* 30:50--65

Sullivan JM, Van Holliday D, McFarland M, McManus MA, Cheriton OM, et al. 2010b. Layered organization in the coastal ocean: an introduction to planktonic thin layers and the LOCO project. *Cont. Shelf Res.* 30:1--6

Tiselius P. 1992. Behavior of *Acartia tonsa* in patchy food environments. *Limnol. Oceanogr.* 37:1640--51

Tiselius P, Jonsson PR, Verity PG. 1993. A model evaluation of the impact of food patchiness on foraging strategy and predation risk in zooplankton. *Bull. Mar. Sci.* 53:247--64

Townsend DW, Bennett SL, Thomas MA. 2005. Diel vertical distributions of the red tide dinoflagellate *Alexandrium fundyense* in the Gulf of Maine. *Deep-Sea Res. Part 2* 52:2593--602

Turner JT, Tester PA. 1997. Toxic marine phytoplankton, zooplankton grazers, and pelagic food webs. *Limnol. Oceanogr.* 42:1203—14

Twardowski MS, Sullivan JM, Donaghay PL, Zaneveld JRV. 1999. Microscale quantification of the absorption by dissolved and particulate material in coastal waters with an ac-9. *J. Atmos. Ocean. Techol.* 16: 691-707.

Tyler MA, Seliger HH. 1978. Annual subsurface transport of a red tide dinoflagellate to its bloom area: water circulation patterns and organism distributions in Chesapeake Bay. *Limnol. Oceanogr.* 23:227--46

Vanierland ET, Peperzak L. 1984. Separation of marine seston and density determination of marine diatoms by density gradient centrifugation. *J. Plankton Res.* 6:29--44

Villareal TA, Carpenter EJ. 2003. Buoyancy regulation and the potential for vertical migration in the oceanic cyanobacterium *Trichodesmium*. *Microb. Ecol.* 45:1--10

Visser AW. 1997. Using random walk models to simulate the vertical distribution of particles in a turbulent water column. *Mar. Ecol. Prog. Ser.* 158:275--81

Walsby AE. 1972. Structure and function of gas vacuoles. *Bacteriol. Rev.* 36:1—32

Waterbury JB, Willey JM, Franks DG, Valois FW, Watson, SW. 1985. A cyanobacterium capable of swimming motility. *Science* 230: 74-76.

Waters RL, Mitchell JG, Seymour J. 2003. Geostatistical characterisation of centimetre-scale spatial structure of in vivo fluorescence. *Mar. Ecol. Prog. Ser.* 251:49--58

White AE, Spitz YH, Letelier RM. 2006. Modeling carbohydrate ballasting by *Trichodesmium* spp. *Mar. Ecol. Prog. Ser.* 323:35--45

Woodson CB, Webster DR, Weissburg MJ, Yen J. 2005. Response of copepods to physical gradients associated with structure in the ocean. *Limnol. Oceanogr.* 50:1552--64

Woodson CB, Webster DR, Weissburg MJ, Yen J. 2007. Cue hierarchy and foraging in calanoid copepods: ecological implications of oceanographic structure. *Mar. Ecol. Prog. Ser.* 330:163--77